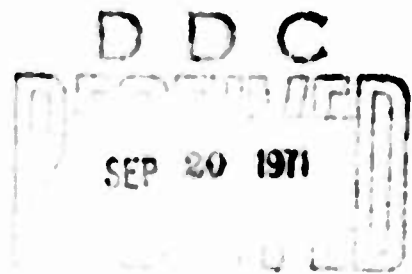$ax.l - 2$

AD

USAAVLABS TECHNICAL REPORT 70-74A

STABILITY AND CONTROL OF HELICOPTERS IN STEEP APPROACHES

VOLUME I
SUMMARY REPORT

By
Julian Wolkovitch
John A. Hoffman

May 1971

D D C

SEP 20 1971

EUSTIS DIRECTORATE
U. S. ARMY AIR MOBILITY RESEARCH AND DEVELOPMENT LABORATORY
FORT EUSTIS, VIRGINIA

DISCLAIMERS

The findings in this report are not to be construed as an official Department of the Army position unless so designated by other authorized documents.

When Government drawings, specifications, or other data are used for any purpose other than in connection with a definitely related Government procurement operation, the United States Government thereby incurs no responsibility nor any obligation whatsoever; and the fact that the Government may have formulated, furnished, or in any way supplied the said drawings, specifications, or other data is not to be regarded by implication or otherwise as in any manner licensing the holder or any other person or corporation, or conveying any rights or permission, to manufacture, use, or sell any patented invention that may in any way be related thereto.

DISPOSITION INSTRUCTIONS

Destroy this report when no longer needed. Do not return it to the originator.

DOCUMENT CONTROL DATA - R & D

(Security classification of title, body of abstract and indexing annotation must be entered when the overall report is classified)

1. ORIGINATING ACTIVITY (Corporate author)	2a. REPORT SECURITY CLASSIFICATION
Mechanics Research, Inc. 9841 Airport Blvd. Los Angeles, California	Unclassified
	2b. GROUP NA

3. REPORT TITLE

STABILITY AND CONTROL OF HELICOPTERS IN STEEP APPROACHES
VOLUME I. SUMMARY REPORT

4. DESCRIPTIVE NOTES (Type of report and inclusive dates)

Final Report

5. AUTHOR(S) (First name, middle initial, last name)

Julian Wolkovitch
John A. Hoffman

6. REPORT DATE	7a. TOTAL NO. OF PAGES	7b. NO. OF REFS
May 1971	198	39

8a. CONTRACT OR GRANT NO. DAAJ02-69-C-0004	9a. ORIGINATOR'S REPORT NUMBER(S)
b. PROJECT NO. 1F162204A142	USAAVLABS Technical Report 70-74A
c.	9b. OTHER REPORT NO(S) (Any other numbers that may be assigned this report)
d.	MRI Report No. 2284-1

10. DISTRIBUTION STATEMENT

Approved for public release; distribution unlimited.

11. SUPPLEMENTARY NOTES	12. SPONSORING MILITARY ACTIVITY
Volume I of a 4-volume report	Eustis Directorate U.S. Army Air Mobility R&D Laboratory Fort Eustis, Virginia

13. ABSTRACT

Aerodynamics and control characteristics of helicopters in level flight and steep descents at low speeds are analyzed. Single-rotor, tandem-rotor, and compound helicopters are considered and are specifically represented by the S-58, AH-56A, and YHC-1A, for each of which derivatives and transfer functions are presented. New analytic methods are used to describe the flow about descending rotors. Using these methods, predictions are made of the boundaries of the vortex-ring state and of tip loss factors. Good agreement with experiment is obtained. A new modular stability derivative program, MOSTAB, is described and is used to calculate derivatives for the S-58 and AH-56A, including lateral-longitudinal cross-coupling derivatives. It is shown that, for these helicopters, control of flight path by collective pitch becomes difficult for low-speed steep descents even with stability augmentation, due to a nonminimum phase transfer function and the associated wrong-way step response characteristic. The effect is identified as an important factor in the observed degradation of flying qualities in steep approaches.

DD FORM 1473, 1 NOV 65 REPLACES DD FORM 1473, 1 JAN 64, WHICH IS OBSOLETE FOR ARMY USE.

14. KEY WORDS	LINK A		LINK B		LINK C	
	ROLE	WT	ROLE	WT	ROLE	WT
HELICOPTER STABILITY AND CONTROL						
HELICOPTER AERODYNAMICS						
HELICOPTER STABILITY DERIVATIVES						
HELICOPTER TRANSFER FUNCTIONS						
V/STOL STEEP APPROACH						
VORTEX-RING STATE						
SIKORSKY S-58 STABILITY AND CONTROL						
LOCKHEED AH-56A STABILITY AND CONTROL						
BOEING-VERTOL YHC-1A STABILITY AND CONTROL						
MOSTAB DIGITAL COMPUTER PROGRAM						

The report has been reviewed by the Eustis Directorate,
U. S. Army Air Mobility Research and Development Labora-
tory, and is judged to be technically sound.

The primary effort is to examine the behavior of rotary-
wing aircraft in steep approaches, from the standpoint
of aerodynamics and dynamics, and the resultant effects
on human and automatic control.

The report is presented in four volumes. Volume I sum-
marizes the main results of the study. Volume II des-
cribes the MOSTAB program. Volume III presents derivatives
and transfer functions for the YHC-1A tandem-rotor heli-
copter and the S-58 single-rotor helicopter. Volume IV
presents derivatives and transfer functions for the AH-56A
compound helicopter and data on low-altitude turbulence
representation.

The program was conducted under the technical management
of Mr William D. Vann, Aeromechanics Division.

STABILITY AND CONTROL OF HELICOPTERS
IN STEEP APPROACHES

VOLUME I

SUMMARY REPORT

MRI REPORT NO. 2284-1

By

Julian Wolkovitch
John A. Hoffman

Prepared by

Mechanics Research, Inc.
Los Angeles, California

for

EUSTIS DIRECTORATE
U.S. ARMY AIR MOBILITY RESEARCH AND DEVELOPMENT LABORATORY
FORT EUSTIS, VIRGINIA

ABSTRACT

Aerodynamics and control characteristics of helicopters in level flight and steep descents at low speeds are analyzed. Single-rotor, tandem-rotor, and compound helicopters are considered and are specifically represented by the S-58, AH-56A, and YHC-1A, for each of which derivatives and transfer functions are presented. New analytic methods are used to describe the flow about descending rotors. Using these methods, predictions are made of the boundaries of the vortex-ring state and of tip loss factors. Good agreement with experiment is obtained. A new modular stability derivative program, MOSTAB, is described and is used to calculate derivatives for the S-58 and AH-56A, including lateral-longitudinal cross-coupling derivatives. It is shown that, for these helicopters, control of flight path by collective pitch becomes difficult for low-speed steep descents even with stability augmentation, due to a nonminimum phase transfer function and the associated wrong-way step response characteristic. The effect is identified as an important factor in the observed degradation of flying qualities in steep approaches.

iii

FOREWORD

This research was performed by Mechanics Research, Inc. under United States Army Aviation Materiel Laboratories*Contract DAAJO2-69-C-0004, Project 1F162204A142. The AVLABS Project Monitor was Mr. W. D. Vann.

The authors express their gratitude to Mr. Vann and Mr. Robert P. Smith of AVLABS for constant encouragement and assistance. Thanks are also due to Dr. M. J. Abzug for granting permission to use TRW technical memoranda, and to Mr. J. M. Drees of the Bell Helicopter Company who supplied several valuable references relating to his pioneering work on the vortex-ring state.

Finally, the authors thank their colleagues at Mechanics Research, Inc. who contributed to this report: in particular, Mr. H. B. Amey and Mr. D. W. Lochtie who gave significant technical support.

---

*Redesignated Eustis Directorate, U.S. Army Air Mobility Research and Development Laboratory.

TABLE OF CONTENTS

LIST OF ILLUSTRATIONS

LIST OF TABLES

LIST OF SYMBOLS

A	Aspect ratio, also characteristic area for interference velocity
A_f	Profile drag area, $D/\frac{1}{2}(\rho V^2)$
A_{1c}	Lateral stick deflection commanding A_{1s}
A_{1s}	Lateral cyclic pitch
a	Blade section lift-curve slope
a_z	Acceleration along the aircraft z-axis
B	Tip loss factor, R_e/R
B_{1c}	Longitudinal stick deflection commanding B_{1s}
B_{1s}	Longitudinal cyclic pitch
b	Number of blades
C_D	Drag coefficient $= D/\frac{1}{2}(\rho V^2 S)$
C_L	Lift coefficient $= L/\frac{1}{2}(\rho V^2 S)$
C_T	$T/\rho(\Omega R)^2 \pi R^2$, or alternatively, $T/\rho(\Omega R_e)^2 \pi R_e^2$, as appropriate
C_T	$T/\rho\pi\Omega^2 R^4$ helicopter rotor thrust coefficient
C_{T_p}	$T/\rho n^2 D^4$, propeller thrust coefficient
D	Rotor diameter, or total aircraft drag, as appropriate

D_p	Parasite drag, i.e., drag not induced by lift
D/L	Drag/lift ratio
e	Span-efficiency factor
F	$T/2\rho A(\nu-V)^2$
F_o	Momentum flux into the rotor system from the distant atmosphere
F_w	Momentum flux in the distant wake
f	$T/2\rho AV^2$
g	Acceleration due to gravity
h	Height
$\hat{h}$	Height error, i.e., perpendicular distance from unperturbed flight path to the c.g. of the aircraft $(= h$ for $\gamma_o = 0)$
h	Rate of climb
I	Moment or product of inertia
J	V/nD
K_β	Sideslip feedback gain
k	Ratio of the mean induced velocity under consideration to that at the rotor
L	Rolling moment
M	Pitching moment
M_f	Nondimensional mass flow: $M_f = \dot{m}/\pi R^2 \rho \Omega R$, $M_f > 0$ for a net downward flow through the rotor

m	Aircraft mass
$\dot{m}$	Mass flow through rotor
N	Yawing moment
n	Rotor rotational speed, revs/sec
P_o	Energy influx to the rotor flow system from the distant atmosphere per second
P_R	Power added to the flow by the rotor
P_w	Energy efflux through the distant wake per second
p	Aircraft perturbation rate of roll
q	Aircraft perturbation rate of pitch
R	Rotor radius
R_e	Effective rotor radius
R_w	Radius of distant wake (from rotor spin axis to outer edge of vortex core)
r	Aircraft perturbation rate of yaw, or vortex core radius, as appropriate
S	Wing area, or other stated reference area
S_e	Momentum theory "area of capture" for tandem rotors
s	Laplace transform complex variable
T	Thrust, or time constant, as appropriate
$\bar{T}$	Mean thrust

U_o	Unperturbed velocity along the aircraft x-axis
u	Aircraft perturbation velocity along x-axis
V	Descent velocity
V_A	Wind speed
V_r	Resultant velocity at actuator disc
V_T	Resultant velocity at module
v	Sideslip velocity, or $v - V$, as appropriate
W	Weight
w	Aircraft perturbation velocity along z-axis
X	Force along aircraft x-axis
x	Horizontal distance
x	s/R or s_w/R_w
y	Force along aircraft y-axis
Z	Force along aircraft z-axis
Z_w	Plunge damping stability derivative
α	Inclination of plane of actuator disc to flight path, positive for descent
α	$v/\Omega R$
β	Sideslip angle
γ	Angle of flight path to horizontal, negative for descent

γ_o	Unperturbed flight path angle, positive for climb
ΔT	$T - \overline{T}$
δ, δ_w	Diameter of vortex core divided by R or R_w respectively
δ_A	Lateral stick deflection
δ_e	Pitch control deflection
δ_R	Rudder pedal deflection
ϵ	R_w/R, wake contraction ratio
θ	Pitch angle
θ_{op}	Pusher propeller collective pitch
θ_o	Collective pitch of main rotor
θ_{oTR}	Tail rotor collective pitch
θ_r	Blade pitch angle at the root
θ_t	Blade pitch angle at the tip
$\theta_{.75}$	Blade pitch angle at 0.75R
Λ	$V/\Omega R$
λ	$\nu/\Omega R$
ν	Induced velocity at rotor or actuator disc (positive in the opposite direction to rotor thrust)
ν_w	Induced velocity in the wake

ν_h	(Thrust of one rotor/$2\rho\pi R^2)^{1/2}$, theoretical induced velocity at actuator disc in hover
ρ	Air density
σ	Solidity
ϕ	Bank angle
Ω	Rotor rotational speed, rad/sec
Ω_h	Rotor rotational speed in hover, rad/sec
ω	Frequency, rad/sec

Special Mathematical Symbols

$\approx$	Approximately equals
$\triangleq$	Defined equal to
$\|x\|$	Absolute magnitude of x
x_o	Unperturbed value of x
$\overset{o}{x}, \dot{x}$	Derivative of x with respect to time

.

CHAPTER I. INTRODUCTION

I.1   THE SCOPE OF THIS REPORT

This introduction is divided into two parts. In the first, we describe the scope of the report and indicate how it advances the state of the art. The second part of the introduction is a summary of the specific contents of the report, chapter by chapter. The reader who does not wish to read the entire report should use Section 2 of the introduction as a guide to areas of specific interest.

Approach and landing are generally the most demanding portions of a flight, for both fixed-wing aircraft and helicopters. Proximity to the ground demands increased precision in controlling the flight path, and the pilot's task may be extremely difficult, particularly in IFR conditions. Pilot comments on helicopters have indicated that the difficulties become more pronounced as the desired approach angle increases (see, e.g., Ref. 1). This suggests that at least part of the difficulty stems from changes in the dynamics and aerodynamic characteristics of the helicopter associated with change in the trim condition from level flight to descent. This is the area of most interest to the present report. The main purpose of this report is to identify the effects of descent angle on the aerodynamics and dynamics of typical helicopters, and to interpret the significance of these effects for human and automatic control.

To achieve this goal it was necessary to go back to fundamentals. As will be described, it was difficult to obtain reliable stability derivatives for small perturbations from steep descents, and these had to be calculated. Such calculations required a better understanding of the effect of descent angle on the flow about the rotor in the unperturbed condition. This required some advances in aerodynamic theory. These included delineation of the boundaries of the vortex-ring state, plus improved analytic models for the aerodynamic tip losses of rotors in level flight and descent.

Having obtained improved flow models for the aerodynamics of rotors in steep descents, it was necessary to calculate stability derivatives incorporating these models. Stability derivatives are presented here for three specific helicopters: the Sikorsky S-58, the Boeing-Vertol YHC-1A, and the Lockheed AH-56A Cheyenne. These are employed to represent the general classes of single-rotor, tandem-rotor, and compound helicopters. Inferences are drawn about the behavior of each class from the dynamics of these individual configurations.

1

The variety of configurations and the novel flow representations made it impossible to use handbook methods of computing derivatives, or even existing computer programs. The available programs were tied to particular classes of helicopter and/or certain flow representations. We therefore developed a new computer program for calculating derivatives. This program, called MOSTAB (modular stability derivative program), calculates trim and stability derivatives for any flying vehicle, described as an assemblage of rigid and flexible rotors, bodies, and fixed lifting surfaces (wings, tails). The MOSTAB program is an important product of this study. It was used to calculate trim conditions and stability derivatives for speeds of 0, 20, 40, 60, and 100 knots for the S-58 and AH-56A in level flight and descent. For the YHC-1A published derivatives were used.

Having obtained the derivatives, it was noticed that strong cross-coupling between lateral and longitudinal perturbations occurred, as evidenced by large magnitudes of derivatives such as L_q, M_p as compared with L_p, M_q. In many previous analytic studies, these cross-coupling derivatives were not available. Such an incomplete treatment, with arbitrary decoupling of longitudinal and lateral perturbations, did not seem appropriate for a fundamental study, and so all the cross-coupling derivatives were retained; the transfer functions thus indicated the responses in six degrees of freedom to each control input.

To validate the above transfer functions, several sets of responses to step control inputs calculated using MOSTAB derivatives were compared with flight test time histories, showing good agreement.

Finally, the implications of the transfer functions for control of each helicopter were considered. The philosophy was a sort of "reverse optimization"; instead of attempting to produce the best system, by modifying the characteristics of the aircraft, we searched for these characteristics which would cause difficulties for human and automatic control. Special interest centered on adverse characteristics which appeared in descent but were absent from level flight. It was found that some transfer functions did exhibit significant differences between level flight and descent. In particular, at low speeds, control of the normal deviation from the desired flight path by collective pitch becomes more difficult as the desired descent angle increases. This is demonstrated by the appearance of a right-half plane zero in the appropriate transfer functions.

2

The major advances in the state of the art that are presented in the report are:

(i) a method of predicting the boundaries of the vortex-ring state.

(ii) improved models for the tip losses of helicopter rotors and methods of calculating their effect on derivatives, including cyclic variations of tip losses.

(iii) the MOSTAB program, which calculates trim and stability derivatives of any helicopter configuration.

(iv) presentation of derivatives and transfer functions for representative single-rotor, tandem-rotor, and compound helicopters, including lateral-longitudinal cross-coupling effects.

(v) identification of some significant changes in closed-loop control characteristics between level flight and descents.

I.2. SUMMARY OF SPECIFIC CONTENTS OF THIS REPORT

Chapter II presents a brief summary of the kinematics of steep approaches, demonstrating the equivalence between descent and deceleration capability. The importance of descent/deceleration capability to Army missions is explained. A description is also given of some of the problems that have been observed in steep-approach flight tests. This chapter contains nothing new; it merely sets the stage for the detailed technical analyses that follow, by explaining their relevance to practical problems.

Chapter III presents a theory for predicting the boundaries of the vortex-ring state. This is believed to be the first published theory which predicts the major features of these unsteady flow boundaries. The analysis is very simple, and employs momentum theory and actuator disc concepts. Despite this simplicity, the agreement with experiment is good.

Chapter IV uses flow models developed in Chapter III to calculate the derivatives of an isolated rotor in vertical descent. For purposes of calculating derivatives, it is customary to represent the tip losses by reducing the rotor radius from R to an effective radius BR. Standard formulas exist for B in hover, but in descent these disagree with experiment, yielding inaccurate derivatives. It was therefore necessary to produce modified formulas for B; these

3

are derived in Chapter IV, and are shown to give good agreement with test data on model rotors in vertical descent. Data were not available for inclined descent, for which the theory predicts that the tip losses should vary cyclically. This cyclic tip loss factor was included in subsequent calculations of derivatives. In addition, some cases were re-run without tip losses, to illustrate their importance by comparing transfer functions (given in Chapter VI) with and without tip losses.

Chapter V presents a general description of the MOSTAB modular stability derivative program. This briefly summarizes MOSTAB, avoiding technical detail (which is given in **Volume II**). Chapter V also presents a discussion of the accuracy of the MOSTAB derivatives. Flight test data on the S-58 are compared with predictions from MOSTAB. The results are generally in good agreement.

The derivatives and transfer functions for the YHC-1A, AH-56A and S-58 at each flight condition are presented in **Volumes II - IV.** Eigenvectors and residues of partial fraction expansions of selected transfer functions are given in the main text of the report, where appropriate. These data characterize the transient response characteristics of each helicopter for several forward speeds and descent angles.

The main section of the report continues in Chapter VI with the discussion of the open-loop and closed-loop dynamics of each class of helicopter, as revealed by the above data. Chapter VI discusses the tandem-rotor configuration, exemplified by the YHC-1A. Chapter VII discusses the dynamics of the S-58, representing single-rotor configurations. Chapter VIII discusses some control problems of the compound configuration, typified by the AH-56A. The principal con- clusions of the report are given in Chapter IX.

Volume II provides an extensive account of the MOSTAB program. It should be noted that the version of MOSTAB used in this report (MOSTAB-B) does not include rotor stall or compressibility characteristics, as these were not significant for the approach flight conditions of interest here. Volume II describes the coordinate systems and the rationale for finding trim and derivatives, presents the equations used in MOSTAB and explains the underlying assumptions, describes the rotor analysis method used to represent the first flapping mode, includes a listing of the MOSTAB program, and explains computational aspects of MOSTAB.

Volume III presents derivatives and transfer functions for the YHC-1A tandem-rotor helicopter at forward speeds of 0, 60, and 80 knots, and several descent rates. It also presents derivatives for the S-58 at 0, 20, 40, 60, and 100 knots, and four descent rates (0, 7.5, 15.0, 22.5 fps) at each speed. Transfer functions are also tabulated for all the level flight and maximum descent rate conditions.

Volume IV presents similar data to Volume III for the AH-56A and reviews the literature on turbulence representation for low altitudes.

Reader's Guide

For a quick overview of the main points of this report, read all of Chapter II; the first half of Chapter V, which describes the MOSTAB program; the summaries at the ends of Chapters III, IV, VI, VII, and VIII: and all of Chapter X.

CHAPTER II. OPERATIONAL ASPECTS OF STEEP APPROACHES

II.1   THE IMPORTANCE OF STEEP APPROACH CAPABILITY

In this chapter we review some analytic and experimental work on helicopter steep approaches in order to pinpoint the vehicle parameters of prime importance. As will be shown, one of the most important parameters is maximum obtainable drag/lift ratio expressed as a function of airspeed. This determines the helicopter's descent and deceleration capability.

Figure 1 illustrates the balance of forces in a straight-line descent in still air with acceleration $\overset{o}{V}$. (Note that $\overset{o}{V}$ is negative for deceleration and that the flight path angle γ is also negative for descent.) The relationship between γ, $\overset{o}{V}$, and the drag/lift ratio D/L is

$$\tan(-\gamma) = \frac{D}{L} + \frac{\overset{o}{V}}{g\cos(-\gamma)} \tag{1}$$

The second term is merely the ratio of the acceleration along the flight path to the component of gravitational acceleration along the flight path. Since $\overset{o}{V}$ is negative for deceleration, increased deceleration at a given V and γ requires more D/L, which implies increased D with constant L. In most instances the value of D/L that can be obtained at a given V is limited; thus descent angle may be traded off against deceleration, but the sum of descent angle and deceleration is limited. This limit is fundamental for helicopter steep approaches. For simplicity, the limit is defined by considering a constant-speed descent for which the maximum descent angle is

$$(-\gamma)_{max} = \tan^{-1}(D/L)_{max} \tag{2}$$

Assuming that the landing is made at essentially zero forward speed, the terminal phase of flight must involve descent and deceleration. The way in which these are combined can greatly affect the effectiveness of the mission. This is illustrated by Figure 2, taken from Reference 2, which compares two alternative approach profiles. One is a 10-degree straight-line descent with constant deceleration of 0.088 g. The other approach involves two straight segments: the first at 14.8 degrees with no deceleration, followed by a level segment with 0.264 g deceleration. In both approaches the aircraft is flying at $(D/L)_{max} = 0.264$ throughout.

6
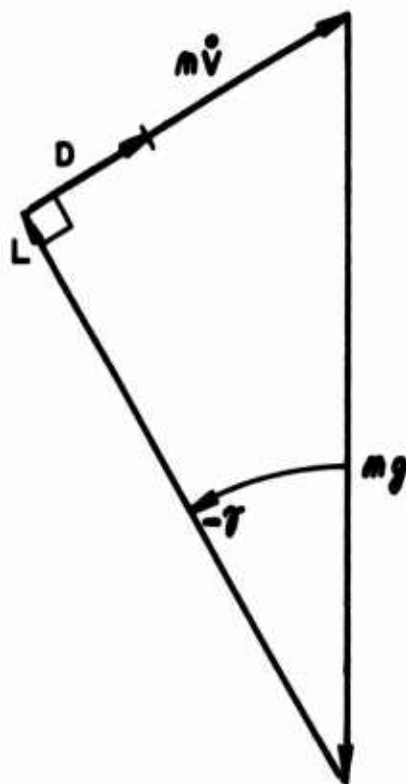
Figure 1. Forces Acting on an Aircraft Flying a Straight-Line Accelerating Descent.

APPROACH	DESCENT			LEVEL FLIGHT			TOTAL TIME
	TAN γ	$\dot{V}$	Δt	TAN γ	$\dot{V}$	Δt	
———	.176	.088	91	—	—	—	91 sec
— —	.264	0	30	0	.264	31	61 sec
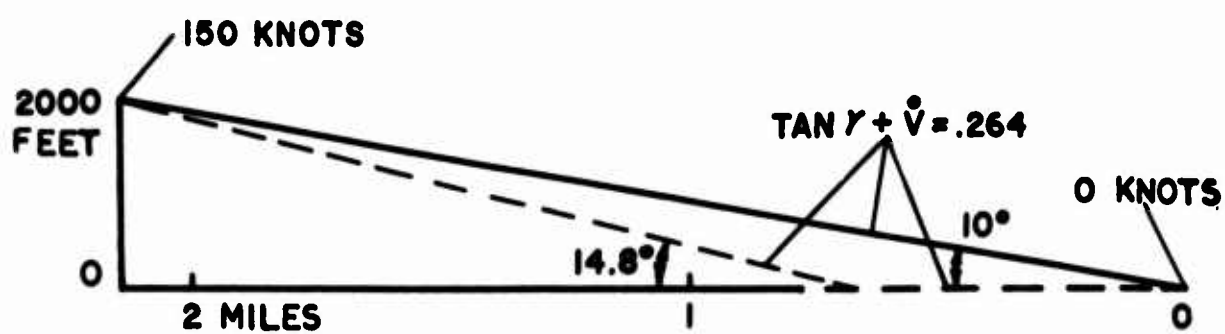
Figure 2. Alternative Approach Flight Profiles.

7

From Figure 2, it will be seen that the total approach time is reduced from 91 seconds to 61 seconds by the two-segment approach. Undoubtedly, further savings are possible by means of more complicated approach profiles. Much work has been done on the optimization of flight paths within given constraints on maximum D/L. Interesting though this is, it is somewhat outside the scope of this report. Our objective is to determine the constraints limiting $(D/L)_{max}$ for given helicopters. This forms the main topic of this and the next chapter.

To show the operational benefits of increased $(D/L)_{max}$ for a given approach profile, consider Figure 3, also taken from Reference 2. $(D/L)_{max}$ must be at least 0.17 in order to achieve the 10-degree descent. However, raising $(D/L)_{max}$ from 0.21 to 0.35 reduces the descent time from 3 to 1.5 minutes, measured from the 3-mile point to touchdown.

Further benefits of increased $(D/L)_{max}$ include enhanced capability to land in confined areas such as valleys and forest clearings. In addition, a high $(D/L)_{max}$ permits steep <u>downwind</u> approaches. This may be important for forward operations or where a normal into-the-wind approach may bring the helicopter uncomfortably close to the enemy. The effects of head- and tailwinds are illustrated in Figure 4.

Using Figure 4 to construct a simple example: for $(D/L) = 0.2$, with 60 knots airspeed and a 20-knot headwind, a descent angle of 17 degrees can be achieved. This reduces to 11.5 degrees in still air and to 8.5 degrees for a 20-knot tailwind. The implications for wind shears are profound.

The net conclusion that emerges from this brief review is that a high $(D/L)_{max}$ is desirable

(i) to minimize unproductive approach time.

(ii) to permit approaches with adverse wind directions and to cope with wind shears.

(iii) to permit approaches to confined areas.

II.2   FACTORS LIMITING $(D/L)_{MAX}$

For most helicopters, $(D/L)_{max}$ is limited by the flow conditions about the main rotor(s). This is illustrated in Figure 5, which shows the permissible regions of horizontal versus vertical

8

FLIGHT PROFILE

ALTITUDE, ft

150 KNOTS

2000

10°

0

DISTANCE FROM AIRPORT, miles

3   2   1   0

TIME FROM 3-MILE POINT TO GROUND CONTACT, min

3

2

1

0

$\dot{V} = 0$ FOR $\gamma = 10°$

VTOL

0   .1   .2   .3   .4   .5

TOTAL DECELERATION$(\dot{V} + \gamma)$, g $\doteq$ D/L
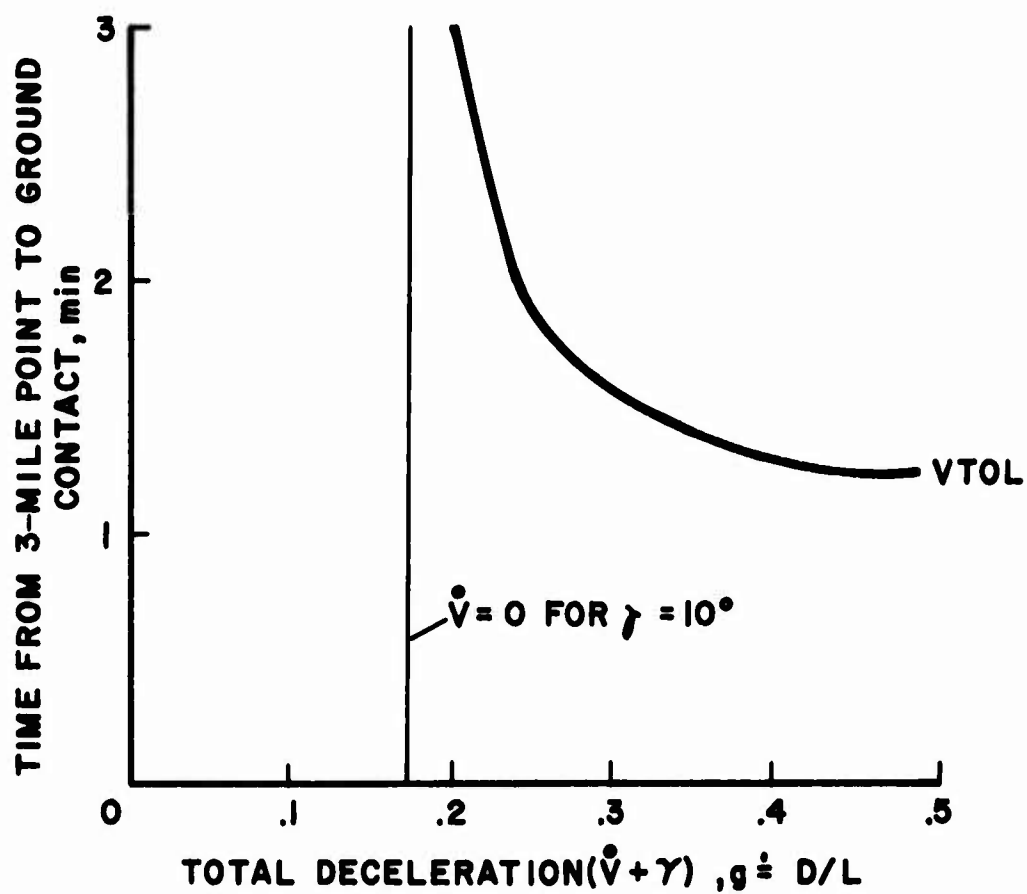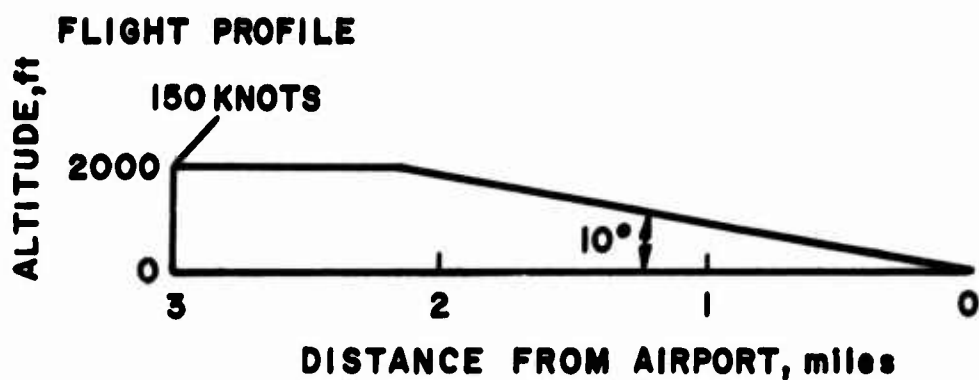
Figure 3. Effect of Descent/Deceleration Capability on Unproductive Mission Time.

9
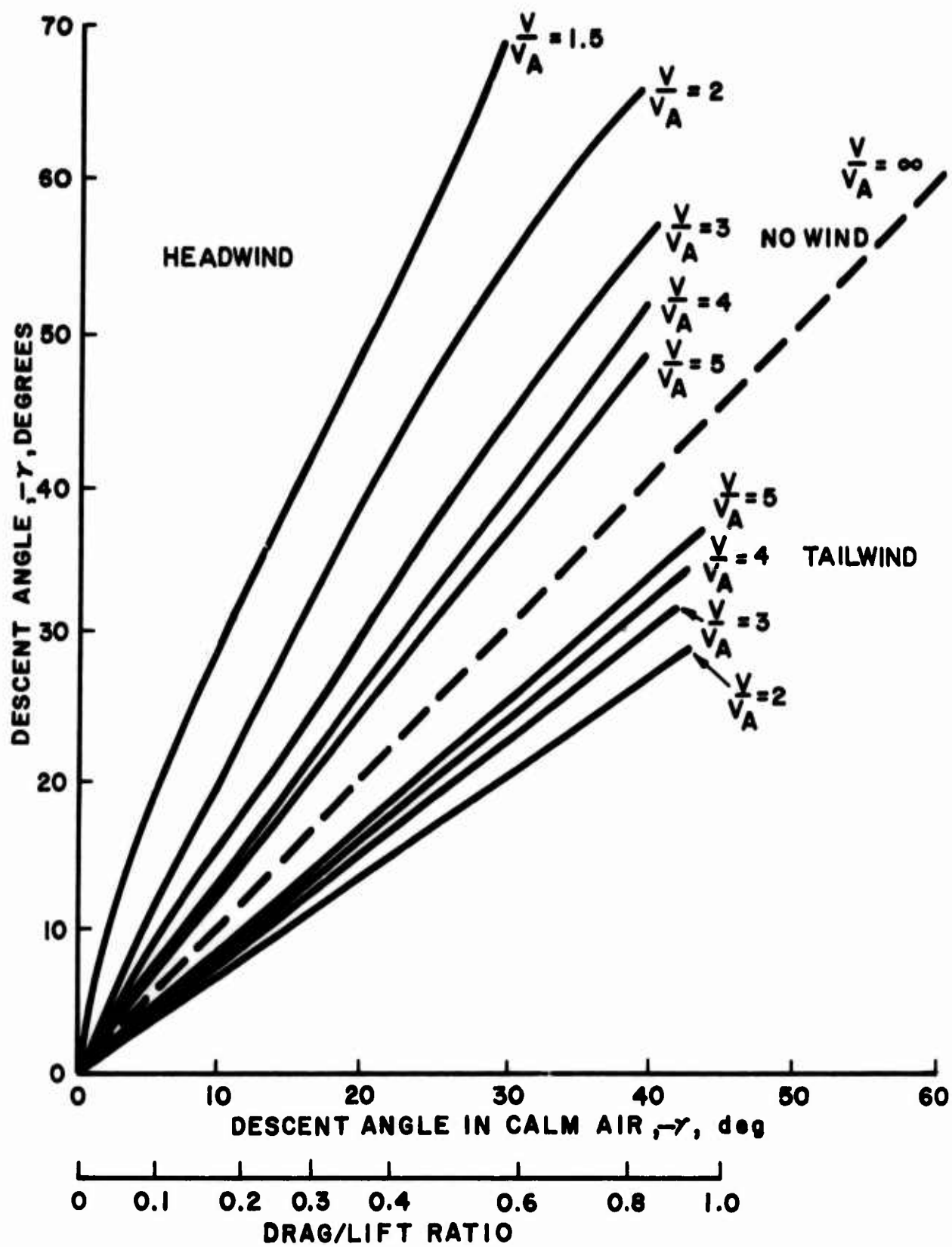
Figure 4. Effect of Head- and Tailwinds on Descent Angle.
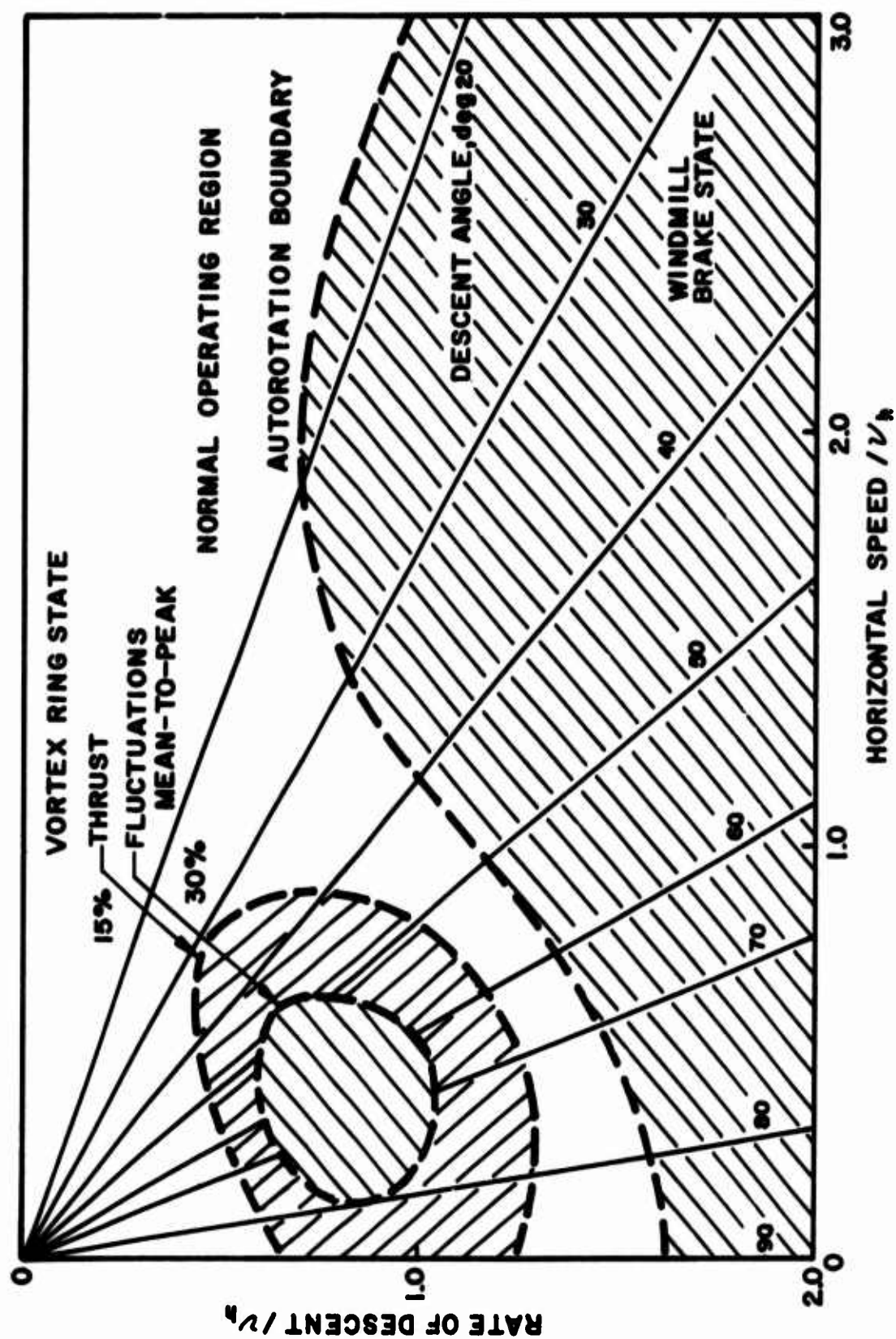
Figure 5. Helicopter Approximate Descent Boundaries in Nondimensional Form.

velocity for a single-rotor helicopter.* The boundaries shown stem
from two causes:

(i) the vortex-ring state
(ii) autorotation

The vortex-ring state is a region of unsteady flow which occurs
on rotors operating at high (D/L) at low speeds. It limits the
maximum achievable steady (D/L). By contrast, the autorotation
boundary is not associated with unsteady flow; it occurs because
the torque on the rotor is zero. Steeper descents would be possible
if a braking torque could be applied to the rotor. Current practice
precludes engine braking, as it is usual to include a freewheel
or override device to prevent stoppage of the rotor following
engine failure.

Autorotation is not widely used in IFR situations because
the rates of descent are usually excessive, particularly for the
higher disc loading helicopters. The principal operational limitation
on $(D/L)_{max}$ therefore is due to the vortex-ring state. This is
discussed at length in Chapter III.

II.3   OTHER FACTORS LIMITING STEEPNESS OF HELICOPTER APPROACHES

The foregoing discussion has emphasized the importance of
$(D/L)_{max}$. However, this is by no means the only factor limiting
the achievable steepness of helicopter approaches. Let us define
the term "nominal flight profile" as a combination of airspeeds,
descent angles, and decelerations which is within the limits
permitted by $(D/L)_{max}$. In practice, a nominal flight profile
may be unflyable. The reasons for this include gust response,
displays, handling qualities, loss of ground reference, etc.
In particular, indications exist that handling qualities deteriorate
with increased steepness of the nominal flight path. For example,
Reference 1, describing tests on a CH-54C helicopter, notes that,
when following a 3-degree nominal flight path, the rate of descent
varied from 100 to 700 ft/min. At $\gamma = -35$ degrees it varied
from 400 to 3000 ft/min, which was regarded as unacceptable. In
addition to the records of longitudinal and lateral deviations
presented in Reference 1, pilot comments also confirmed the deteri-
oration in handling qualities with increased $-\gamma$. A similar trend
is noted in flight tests on a HUP-1 tandem-rotor helicopter described
in References 3 and 4.

---

* In Figure 5 the horizontal and vertical velocities have been
normalized through division by $v_h = (1/2\rho)^{1/2} \times (\text{Disc Loading})^{1/2}$.

Figure 5 is illustrative only and should not be scaled. More
precise boundaries are given in Chapter III.

12

To form a complete assessment of the problems involved in flying steep approaches, it is necessary to consider both the limitations on nominal flight profiles and also the limitations associated with small perturbations from nominal flight profiles. Hence, in Chapter III we analyze the limits on $(D/L)_{max}$. The results are used to determine nominal flight profiles for the YHC-1A, S-58, and AH-56A, and subsequent chapters study the behavior of these helicopters in small perturbations from these nominal flight profiles.

Summary

In this chapter we have tried to "set the stage" for the detailed analyses that follow by demonstrating that:

(i)   High $(D/L)_{max}$ is required to minimize unproductive mission time, to permit steep descents into confined areas, and to allow approaches from any direction, irrespective of the wind vector.

(ii)   At approach speeds, $(D/L)_{max}$ is limited by autorotation and by the vortex-ring state. The latter limit is more serious since it occurs at smaller rates of descent.

(iii)   Within the bounds set by $(D/L)_{max}$, the helicopter's steep descent capability may be limited by some handling qualities factors, which appear to deteriorate with increased steepness of the approach.

CHAPTER III. THE VORTEX-RING STATE

III.1   INTRODUCTION

In performing steep descents at low speeds, helicopters encounter an unsteady flow condition known as the "vortex-ring state". This state is characterized by severe thrust fluctuations and difficulty of control. This chapter presents a simple method of predicting the combination of rate of descent and angle of descent at which the vortex-ring state occurs. Momentum theory and actuator disc concepts are employed; despite the simplicity of this approach, the results are in good agreement with experiment.

The chapter is organized as follows: Section 2 presents an analytical method of calculating the vortex-ring state boundary for vertical descent using simple momentum theory modified to include certain viscous effects. Section 3 extends the method to the case of nonvertical descent. In Section 4 the experimental data and published analyses are reviewed and compared with the theory of this report. Section 5 gives conclusions and recommendations for further work.

III.2   FLOW MODEL AND EQUATIONS FOR VERTICAL DESCENT

The analysis considers both vertical and inclined descent, but the theory is most easily understood by considering the vertical descent case first.

Consider an actuator disc in a uniform stream of air rising with velocity V. This, of course, corresponds to a vertical descent at velocity V on an actual helicopter. The flow model used is illustrated in Figure 6. It consists of a slipstream with uniform flow at any cross-section, surrounded by a tube of vorticity. This tube is modeled by a series of vortex cores. Thus, near the rotor outside the tube the stream velocity is V upward, and inside the tube the velocity is $(v - V)$ downward, where v is the induced velocity at the actuator disc. The rate of descent of the centers of the vortex cores is the mean of these velocities, i.e., $\left(\frac{v}{2} - V\right)$ downward.

The key assumption of the analysis is that the vortex-ring state will occur when the relative velocity of the vortex cores normal to the disc falls to zero. That is, when the rate of descent is increased to the point where vortex cores no longer move away from the actuator disc, unsteady flow occurs. The critical rate of descent V_{crit} at which this occurs is given by

$$V_{crit} = \frac{v}{2} \qquad\qquad (3)$$

14
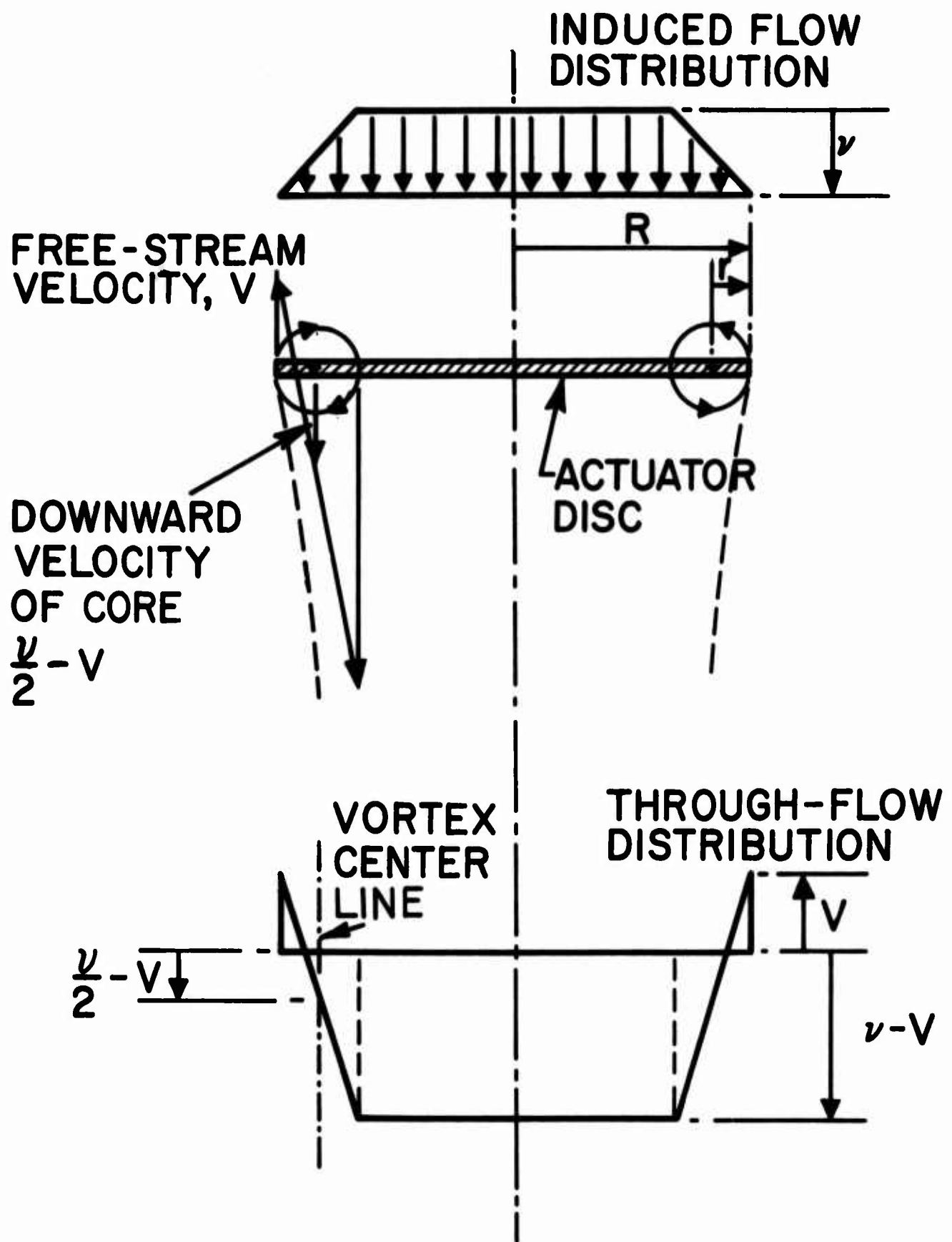
Figure 6. Flow Model for Vertical Descent.

From simple momentum theory (e.g., Reference 5),

$$v = \frac{V}{2} + \sqrt{\left(\frac{V}{2}\right) + v_h^2} \tag{4}$$

where

$$v_h \triangleq \sqrt{\text{Thrust}/2\rho\pi R^2}$$

$$\rho \triangleq \text{Air Density}$$

$$R \triangleq \text{Rotor Radius}$$

Combining (3) and (4) yields the following formula for the rate of vertical descent at which the vortex-ring state commences.

$$V_{crit} = \frac{v_h}{\sqrt{2}} = 0.707 \ v_h \tag{5}$$

This formula, although derived by the simplest possible methods, agrees well with experiments, as will be shown.

An alternative formulation of Eq. (5) can be obtained by putting $J \triangleq V/nD$, $C_{TD} \triangleq T/\rho n^2 D^4$, which gives

$$J_{crit} = \sqrt{\frac{C_{Tp}}{\pi}} \tag{6}$$

16

A further alternative is obtained by using $C_T \triangleq T/\rho\pi\Omega^2 R^4$ and $\lambda \triangleq V/\Omega R$, giving the critical rate of vertical descent as

$$\lambda_{crit} = \frac{1}{2}\sqrt{C_T}$$ (7)

Tip Loss Effects

It is necessary to refine the theory slightly to allow for nonuniform flow when considering high disc loading rotors and/or inclined descents. This is done by introducing a tip loss factor B. Blade elements outside of radius BR are assumed to produce no thrust. Thus, near the rotor, instead of a uniform induced velocity v over an area πR^2, we assume a uniform induced velocity v over an area $\pi R^2 B^2$. This leads to a slight increase in V_{crit} for vertical descents, but the effect is small for typical helicopter disc loadings. The tip loss effect for vertical descents is easily obtained as a special case of the more general formulation of the theory for inclined descents, derived below.

III.3   GENERAL THEORY FOR INCLINED DESCENT

Figure 7 shows the assumed flow model for inclined descent along a flight path inclined at an angle α to the horizontal (for vertical descent $\alpha = 90$ degrees). The velocity of the vortex cores normal to the actuator disc is assumed to be the mean of the normal velocities inside and outside the slipstream, i.e., $(v/2) - V \sin\alpha$. Marked unsteadiness is predicted to occur when the rate of descent becomes sufficiently high to cause the velocity to fall to zero. This condition gives the following general formula:

$$V_{crit} = \frac{v}{2 \sin\alpha}$$ (8)

To express Eq. (8) in a more convenient form, it is necessary to rewrite it in terms of horizontal velocity ($V \cos\alpha$), rate of descent ($V\sin\alpha$), and the tip loss factor B. This is done below by manipulating some equations of momentum theory.

17
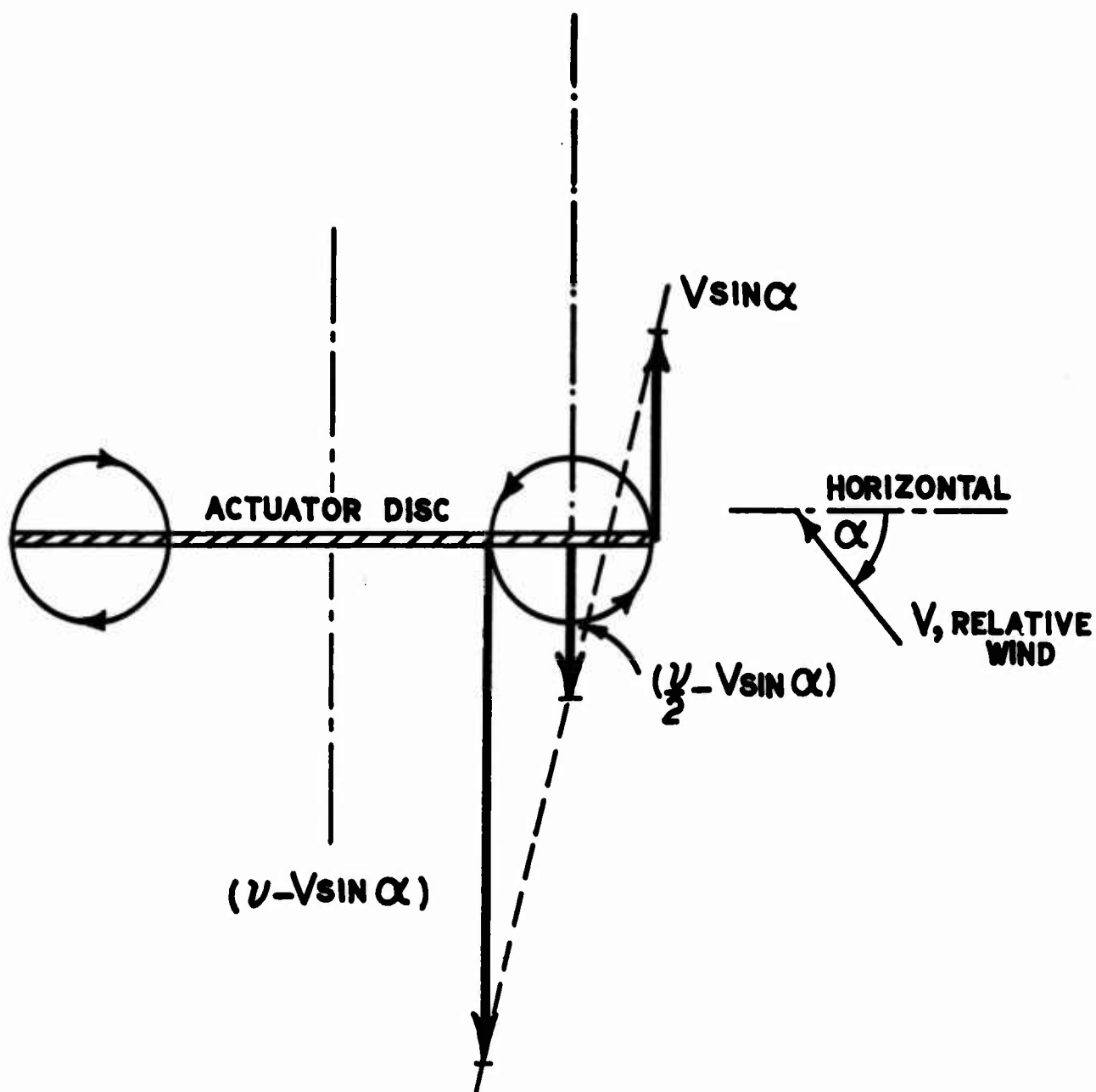
Figure 7. Flow Model for Inclined Descent With No Parasite
Drag, Showing Velocity Components Normal to the
Disc.

From momentum theory (e.g., Reference 5) the thrust of an actuator disc descending at an angle α to the horizontal can be expressed as

$$T = 2\rho\pi R^2 B^2 v |V_r| \qquad (9)$$

where $V_r^2 = v^2 - 2Vv \sin\alpha + V^2 \qquad (10)$

Eqs. (9) and (10) differ from familiar equations of momentum theory only in that the rotor radius R has been replaced by an effective radius BR. Substituting Eq. (10) in Eq. (9), squaring, and using the definition of v_h from Eq. (4) gives

$$(2\pi\rho R^2 v_h^2)^2 = (2\pi\rho R^2 v)^2 B^4 (v^2 - 2V v \sin\alpha + V^2) \qquad (11)$$

Expanding,

$$v_h^4 = B^4 v^4 - 2BV (\sin\alpha) B^3 v^3 + B^2 V^2 B^2 v^2 \qquad (12)$$

$$\left(\frac{v_h}{Bv}\right)^4 = 1 - \frac{2B\ V\sin\alpha}{Bv} + \frac{B^2\ V^2}{B^2\ v^2} \qquad (13)$$

$$\left(\frac{Bv}{v_h}\right)^4 = \frac{1}{1 - \dfrac{2\ B\ V\sin\alpha}{Bv} + \left(\dfrac{BV}{Bv}\right)^2} \qquad (14)$$

This is similar in form to the standard quartic equation of momentum theory usually derived for $B = 1$; i.e., quoting from Reference 5,

$$\left(\frac{v}{v_h}\right)^4 = \frac{1}{1 - \dfrac{2\ V\sin\alpha}{v} + \left(\dfrac{V}{v}\right)^2} \qquad (15)$$

Eq. (15) is conveniently graphed with v/v_h as ordinate and $V\sin\alpha/v_h$ as abscissa, for a fixed α forming a nondimensional graph of induced

19

velocity versus rate of descent for given angle of descent. (Similar graphs are given in References 6 and 7 for B=1.) The graphs can be formed from Eq.(14) for a fixed B using Bv/v_h as ordinate and B Vsinα/v as abscissa. Figure 8 illustrates these graphs for several values of α, from 5 to 90 degrees.

To establish the boundary of the vortex-ring state, for a given B and α, simply include in Figure 8 the critical condition of Eq. (8). Expressed in terms of the variables of Figure 8, Eq. (8) becomes

$$\frac{Bv}{v_h} = \frac{2 \text{ B Vsin}\alpha}{v_h} \tag{16}$$

This describes a straight line of slope 2, as shown on Figure 8. The intersection of this line with the remaining graphs denotes the critical value of rate of descent for a given B and α. It is convenient to plot the results in terms of nondimensional horizontal velocity, Vcosα/v_h, and nondimensional rate of descent, Vsinα/v_h, for a given B as shown on Figures 9, 10, and 11. In these figures, Eq. (16) corresponds to the line marked " zero parasite drag " for which case $\alpha = -\gamma$, as explained below.

Effect of Parasite Drag

The parasite drag of the rotor and of other components has not been included up to this point. This drag causes the boundary of the vortex-ring state to occur at a steeper angle of descent for a given airspeed. The effects of parasite drag can be included in the analysis as indicated below.

Figure 12 shows the forces acting on a helicopter in a steady descent; the aerodynamic forces are assumed to consist only of drag acting parallel to the flight path and rotor thrust normal to the actuator disc.

From Figure 12, resolving parallel and normal to the flight path, noting that γ is negative for descent,

$$T \sin\alpha + D + W \sin \gamma = 0 \tag{17}$$

$$T \cos\alpha - W \cos \gamma = 0 \tag{18}$$
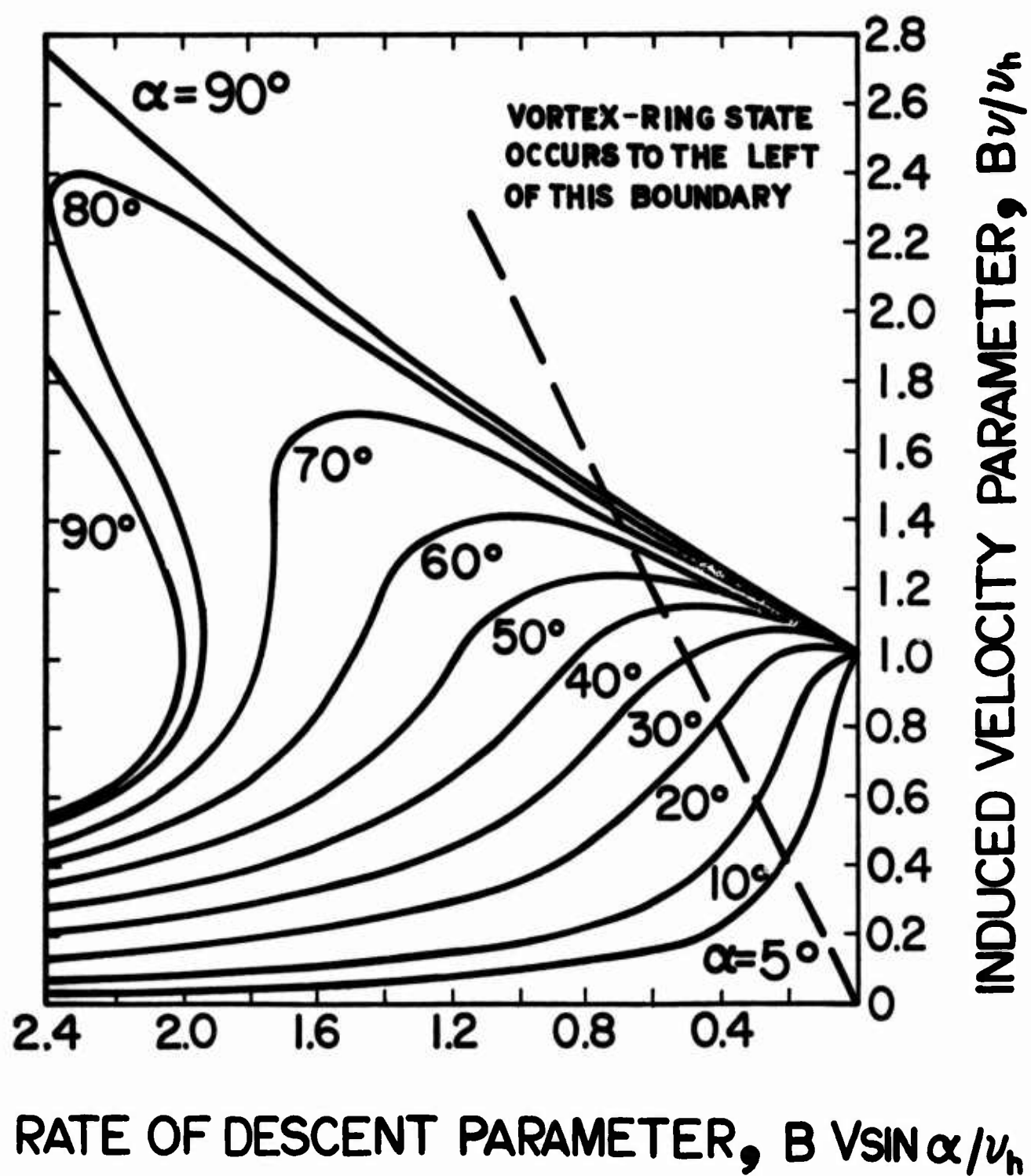
Figure 8. Induced Velocity Versus Rate of Descent From Momentum Theory.

HORIZONTAL VELOCITY PARAMETER, $V\cos(-\gamma)/\nu_h$

RATE OF DESCENT PARAMETER, $V\sin(-\gamma)/\nu_h$

ZERO PARASITE DRAG

WITH PARASITE DRAG
$A_f/4\pi R^2 = 0.05$

30 deg descent

B = 1.0
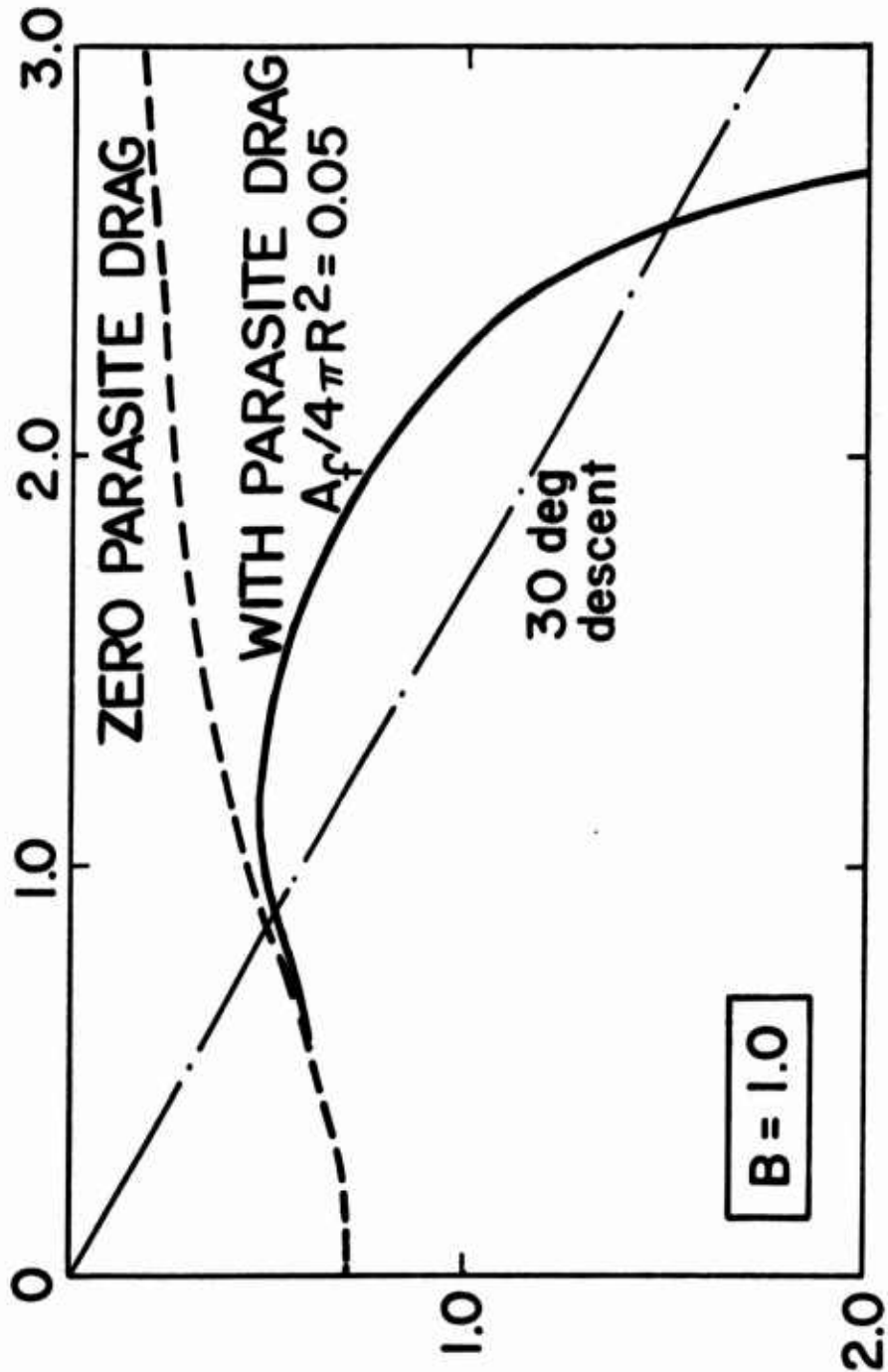
Figure 9. Predicted Upper Boundary of Vortex-Ring State With Zero Tip Loss Factor, B = 1.0 .

22
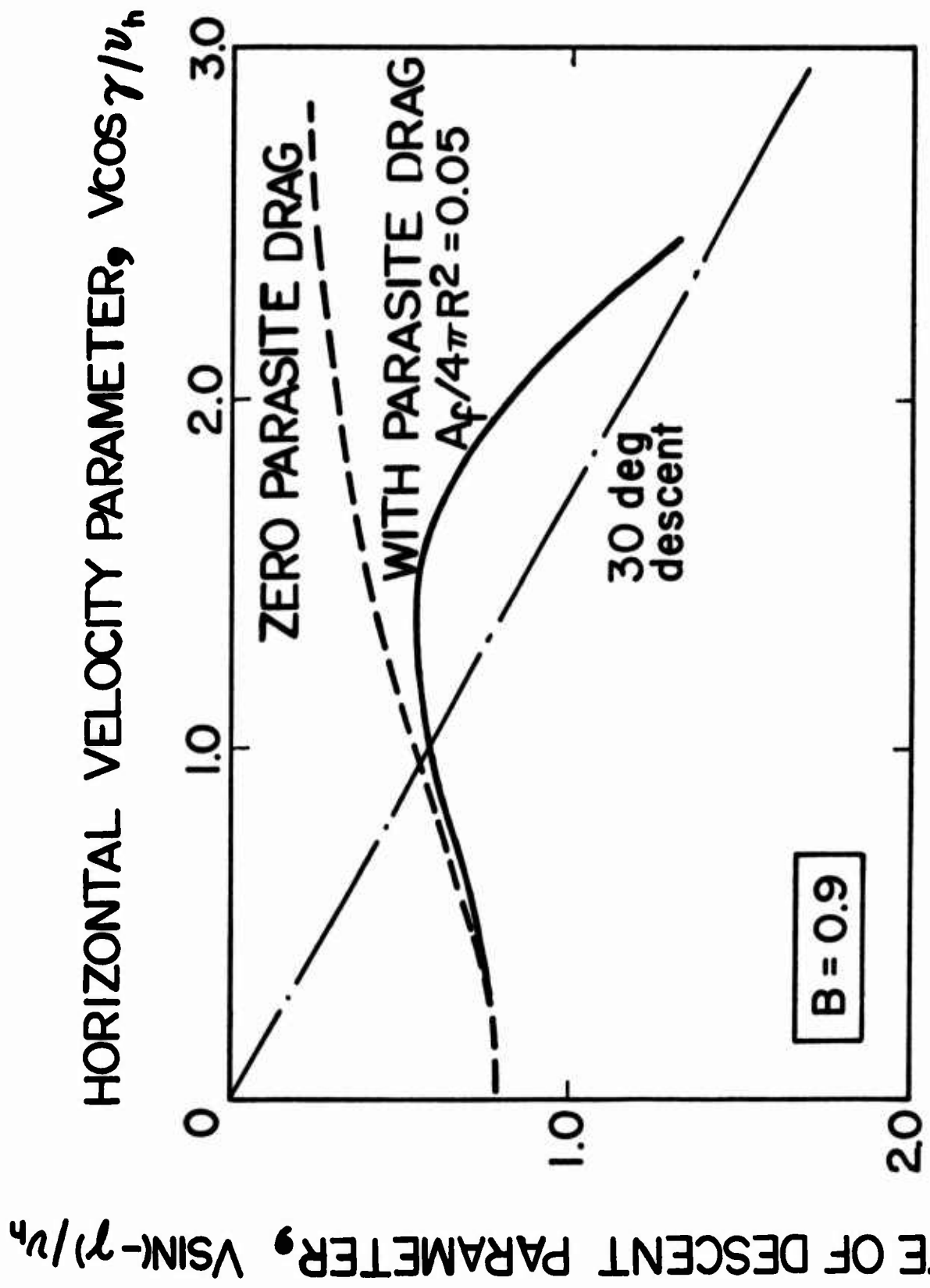
Figure 10. Predicted Upper Boundary of Vortex–Ring State With Tip Loss Factor B = 0.9.
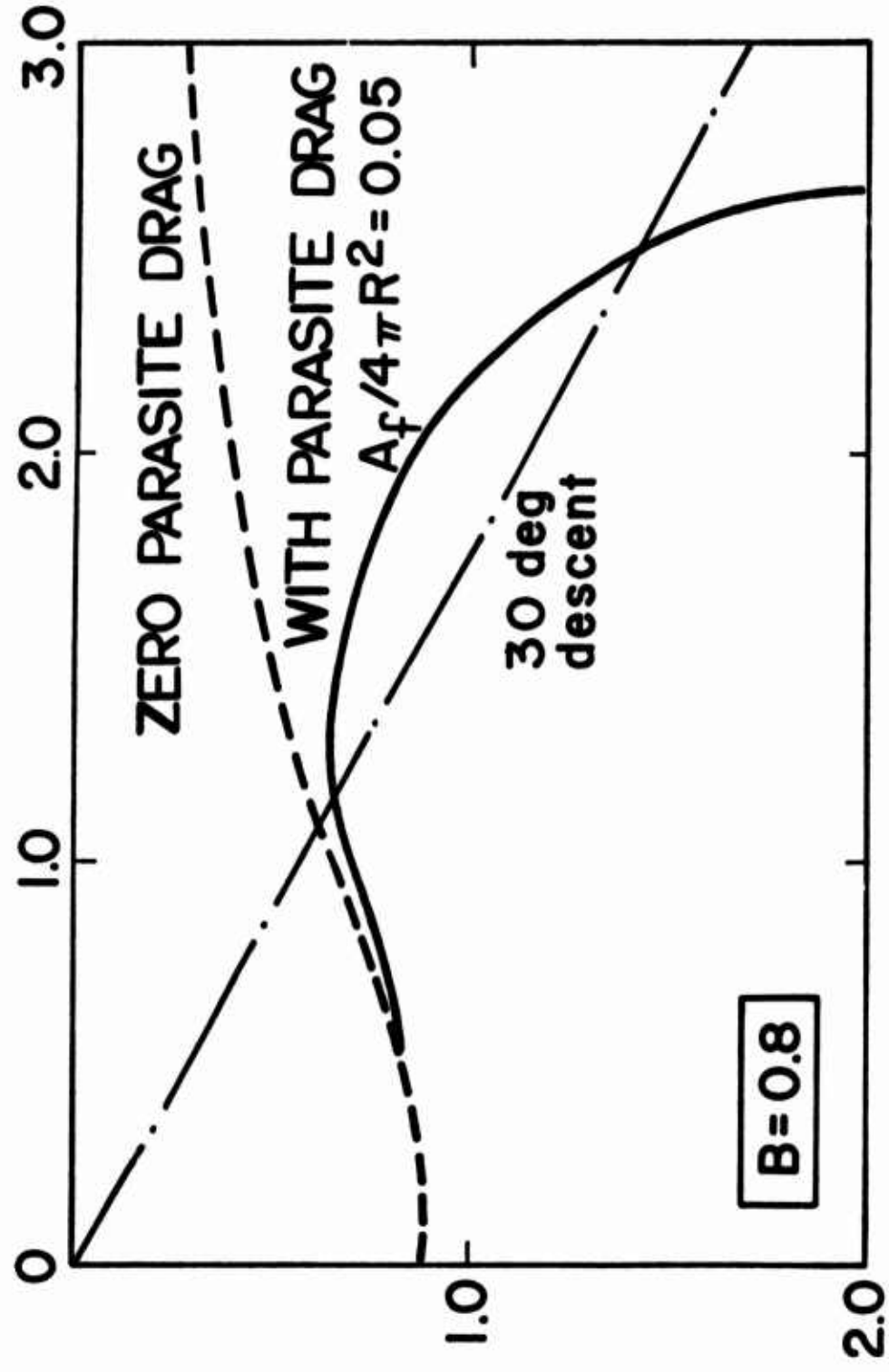
Figure 11. Predicted Upper Boundary of Vortex-Ring State With Tip Loss Factor B = 0.8.
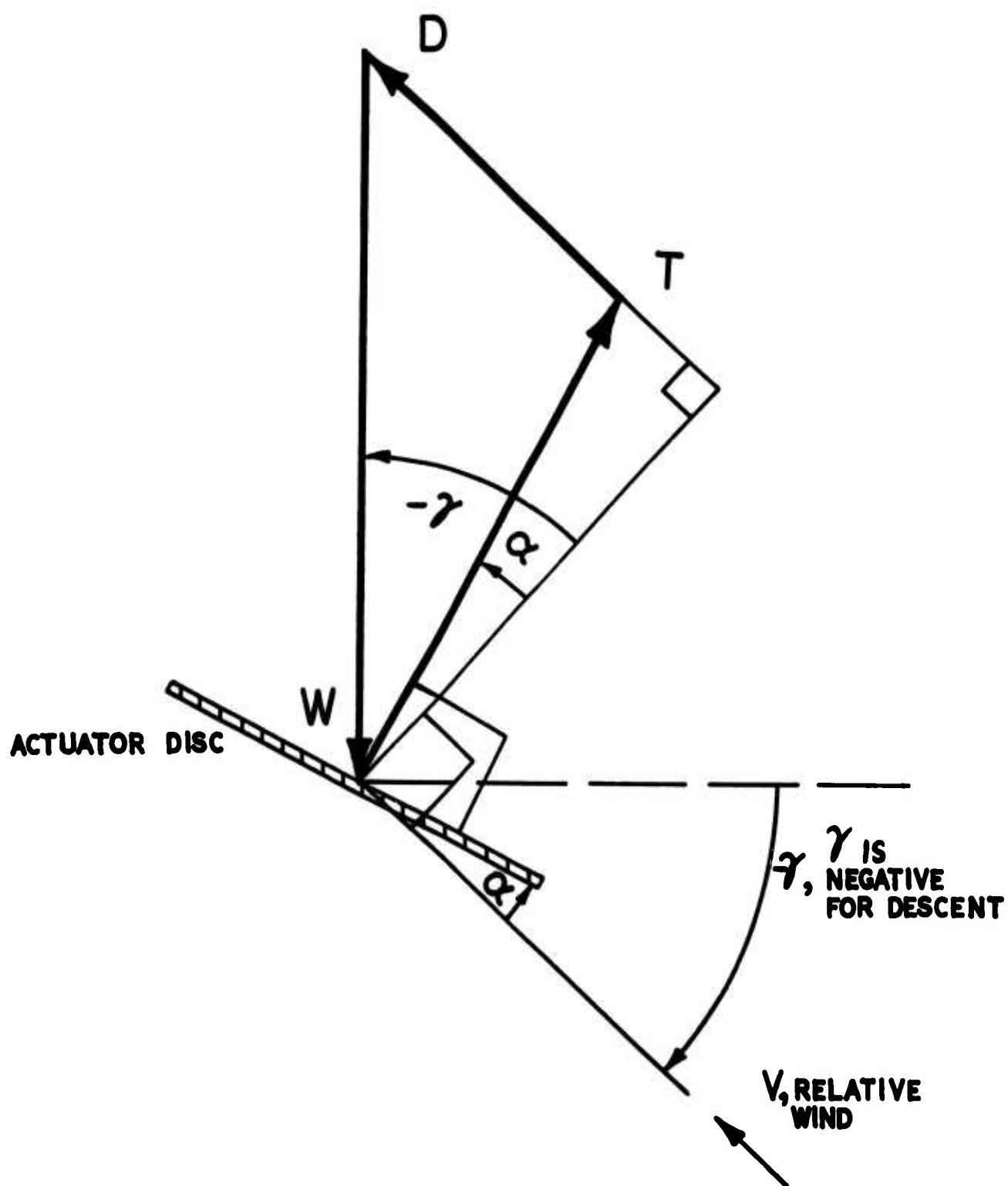
Figure 12. Balance of Forces in Descending Flight.

These equations yield the required relation between γ and α as:

$$\tan \alpha = \frac{-(D/W)}{\cos \gamma} - \tan \gamma \qquad (19)$$

The drag/weight ratio is conveniently expressed in terms of a "drag area" A_f defined as

$$A_f = D/\frac{1}{2}\rho V^2 \qquad (20)$$

Thus, using the definition of v_h, $(v_h^2 = T/2\rho_\pi R^2)$, and assuming thrust at hover equal to weight, Eq. (19) becomes

$$\tan \alpha = - \frac{A_f}{4\pi R^2} \left(\frac{V}{v_h}\right)^2 \frac{1}{\cos \gamma} - \tan \gamma \qquad (21)$$

To modify Figures 9, 10, and 11 to show the effect of profile drag, we require the relationship between γ and $A_f/4\pi R^2$ for a given V and α. This is obtained by manipulating Eq. (21) to give γ in terms of α, V, and $A_f/4\pi R^2$, as follows. Multiply (21) by $\cos\gamma$ and $\cos\alpha$:

$$\sin \alpha \cos \gamma = - \frac{A_f}{4\pi R^2} \left(\frac{V}{v_h}\right)^2 \cos \alpha - \sin \gamma \cos \alpha \qquad (22)$$

$$\sin (\alpha + \gamma) = - \frac{A_f}{4\pi R^2} \left(\frac{V}{v_h}\right)^2 \cos \alpha \qquad (23)$$

$$\gamma = - \alpha - \sin^{-1}\left[\frac{A_f}{4\pi R^2} \left(\frac{V}{v_h}\right)^2 \cos \alpha\right] \qquad (24)$$

Eq. (24) has been used to show the effect of parasite drag in
Figures 9, 10, and 11. For a fixed value of the drag parameter
$A_f/4\pi R^2 = 0.05$, the flight path angle at any V changes from α to γ
as determined from Eq. (22). For zero parasite drag, $\alpha = -\gamma$.
Note that the inclusion of parasite drag yields the characteristic
shape of the vortex-ring boundary, first rising and then falling,
as horizontal speed is increased.

The drag parameter $A_f/4\pi R^2$ was deliberately chosen to be
rather high, so that most helicopters display vortex-ring boundaries
falling between the "zero drag" and "with drag" curves of Figures
9, 10, and 11. To appreciate the physical significance of the parameter
$A_f/4\pi R^2$, note that a value of 0.05 corresponds to a parasite drag area
of 20 percent of the disc area. This is much larger than would be
expected in level flight for most helicopters. However, in descent,
the fuselage may be operating at a large angle of attack, causing a
corresponding increase in drag area. When comparing Figures 9, 10
and 11 with experimental results on wind tunnel models, note that the
parasite drag of the fuselage, tail, and other components will be
disproportionately large at low Reynolds numbers.

To predict vortex-ring boundaries of specific configurations
using Figures 9, 10 and 11 requires the value of the tip loss factor, B.
Well-known formulas exist for B in hover; e.g., Payne (Reference 8)
quotes a formula due to Sissingh,

$$B = 1 - \frac{1}{b} \sqrt{2C_T} \qquad (25)$$

Payne notes that Sissingh's formula is in reasonable agreement with
tests on untwisted, untapered blades but yields values of B which are
too small for uniformly loaded blades. For the latter, Payne suggests
an alternative formula, which at hover reduces to

$$B = 1 - \frac{1}{b} \sqrt{C_T} \qquad (26)$$

27

For high-disc-loading VTOL rotors, both the above formulas appear to give values of B which are too small. An alternative semi-empirical expression is derived in Chapter IV for rotors of ideal twist and is given below. This is more complicated than Eqs. (25) or (26) but gives good accuracy for vertical descent as well as hover.

$$B = 1 - \frac{1}{b} \sqrt{\frac{\sigma a}{2} \left(\theta_t + V/B\Omega R \right)} \qquad (27)$$

This gives a cubic equation for B, for a given rotor geometry, pitch setting, and rate of descent. Empirically it is suggested that Eq. (27) can be used for inclined as well as vertical descent, replacing V by Vsinα.

III.4   COMPARISON WITH EXPERIMENT

Although investigations of the behavior of rotors in the vortex-ring state have been made since the 1920's, only the more recent references contain data useful for comparison with the theory of this report. Most of the earlier references (e.g., Reference 9) are confined to measurement and empirical prediction of the mean thrust and through-flow velocity. Reference 10 summarizes various presentations of parameters such as 1/f and 1/F. These parameters are derived from measurements of **averaged** quantities, so these data are unsuitable for determining the velocity and angle of descent at which noticeable unsteadiness occurs. References 11, 12, 13, 14, and 15 do not include any unsteady force measurements, but they do present some flow visualizations, which quali-tatively indicate a "region of roughness." These data are discussed later. For purposes of comparison with theory, it is unfortunate that the available test data are for blades with non-ideal twist; e.g., References 11, 12, 13, 14, and 15 employ an untwisted rotor. The resulting induced velocity distribution is at variance with the uniform distribution assumed in the present theory. However, even full-scale helicopters do not have ideal twist, so this compromise must be accepted in order to compare theory and experiment.

Vertical Descent

Azuma (Reference 16) presents data on thrust and inflow fluctuations for a 3-bladed rotor, with a diameter of 1100 mm, a solidity of 0.0573, an NACA 0012 section and -8° twist from root to tip, free to flap and lag. The rate-of-descent parameter was expressed as $V\Omega_h/v_h\Omega$, because the nominal rotational speed of 1,000 rpm was not maintained precisely.

Lacking data on $V/\Omega R$, we cannot make allowance for the tip loss factor. However, Eq. (5), $V_{crit} = 0.707 \, v_h$, gives good agreement with the observed onset of significant unsteady thrust and inflow. This is demonstrated in Figure 13. Eq. (5) corresponds to r.m.s. thrust fluctuations $\Delta T/\bar{T}$ ranging from 4% to 14% depending on the blade pitch setting. (The thrust fluctuation, ΔT, is defined as $T - \bar{T}$, where $\bar{T}$ is the mean thrust; thus the r.m.s. peak to peak fluctuation is 8% to 28% of the mean thrust.) Note that the graph marked $\theta_r = 8$ degrees corresponds to zero blade angle at the tip. As predicted by Eq. (3) and Figures 9, 10, and 11, the critical rate of descent normalized with respect to v_h and Ω_h increases as the tip blade angle is increased (by increasing θ_r). The experimental data of Reference 16 indicate that the mean thrust in descent varies; for $\theta_r = 10$ degrees at $V = 0.7 \, v_h \Omega/\Omega_h$, the mean thrust falls to 80% of the hovering thrust. To convert the data to the constant mean thrust assumed by the theory (and appropriate to steady descents), the value of V_{crit} must be increased above that observed experimentally. Without data on C_m, this cannot be done precisely, but the trend will certainly be to move the peaks of the thrust fluctuation curves to the right, thus increasing agreement with the predicted boundary for the onset of unsteady flow.

Washizu (Reference 7) describes tests on a similar rotor in vertical and inclined descent. Figure 14 shows envelopes of C_m versus the rate of descent parameter λ, for vertical descent. For two of the tests, the blade pitch setting is very low and the tips are actually lifting downward in hover. This invalidates comparisons with our theory, which assumes uniform inflow except at the tips, corresponding to the rather high pitch setting appropriate to maximum static thrust/power. For this reason, the data taken at $\theta_{.75} = 4.5$ degrees are also unsuitable for comparison. However, using Eq. (7) and B = 0.95, the case with $\theta_{tip} = 8.0$ degrees gives $\lambda_{crit} = 0.033$. This corresponds to a mean-to-peak thrust fluctuation of 12% of the mean thrust.

Inclined Descent

Washizu **et al** presents experimental data on thrust and induced velocity fluctuations in the vortex-ring state for single-rotor configurations (Reference 7) and tandem configurations (Reference 17). Contours of percentage thrust fluctuation are shown on the horizontal velocity/rate-of-descent plane; however, the data points are not indicated. Hence results for low pitch angles cannot be removed to enable the remaining data to be compared with the theory. Washizu **et al** gives more complete data on induced velocity fluctuations, averaged over the disc based on measurements of thrust and torque fluctuations, and these can be compared with theory. Figures 15 and 16

29
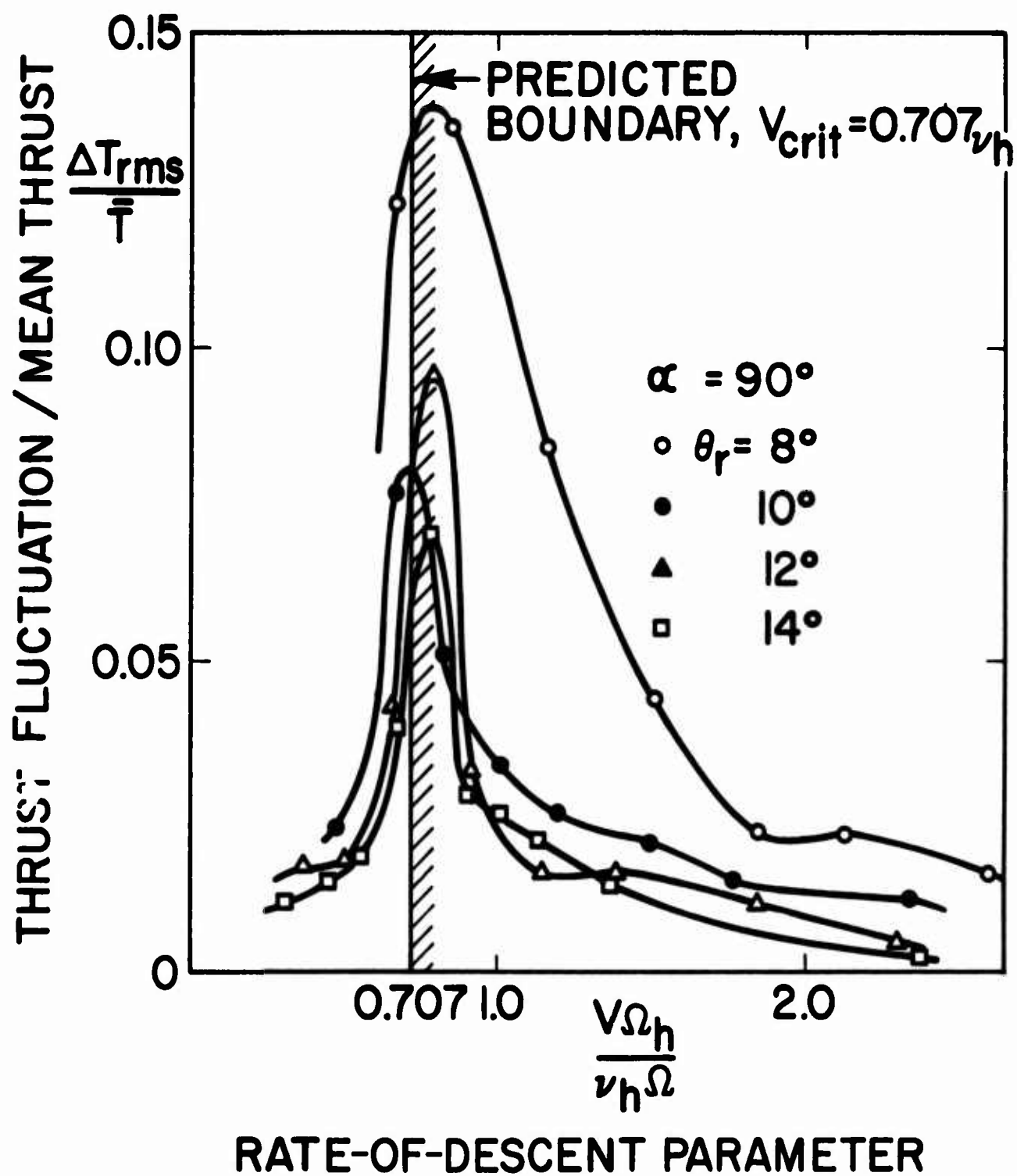
Figure 13. Measured Thrust Fluctuation for a Model
Helicopter Rotor in Vertical Descent.
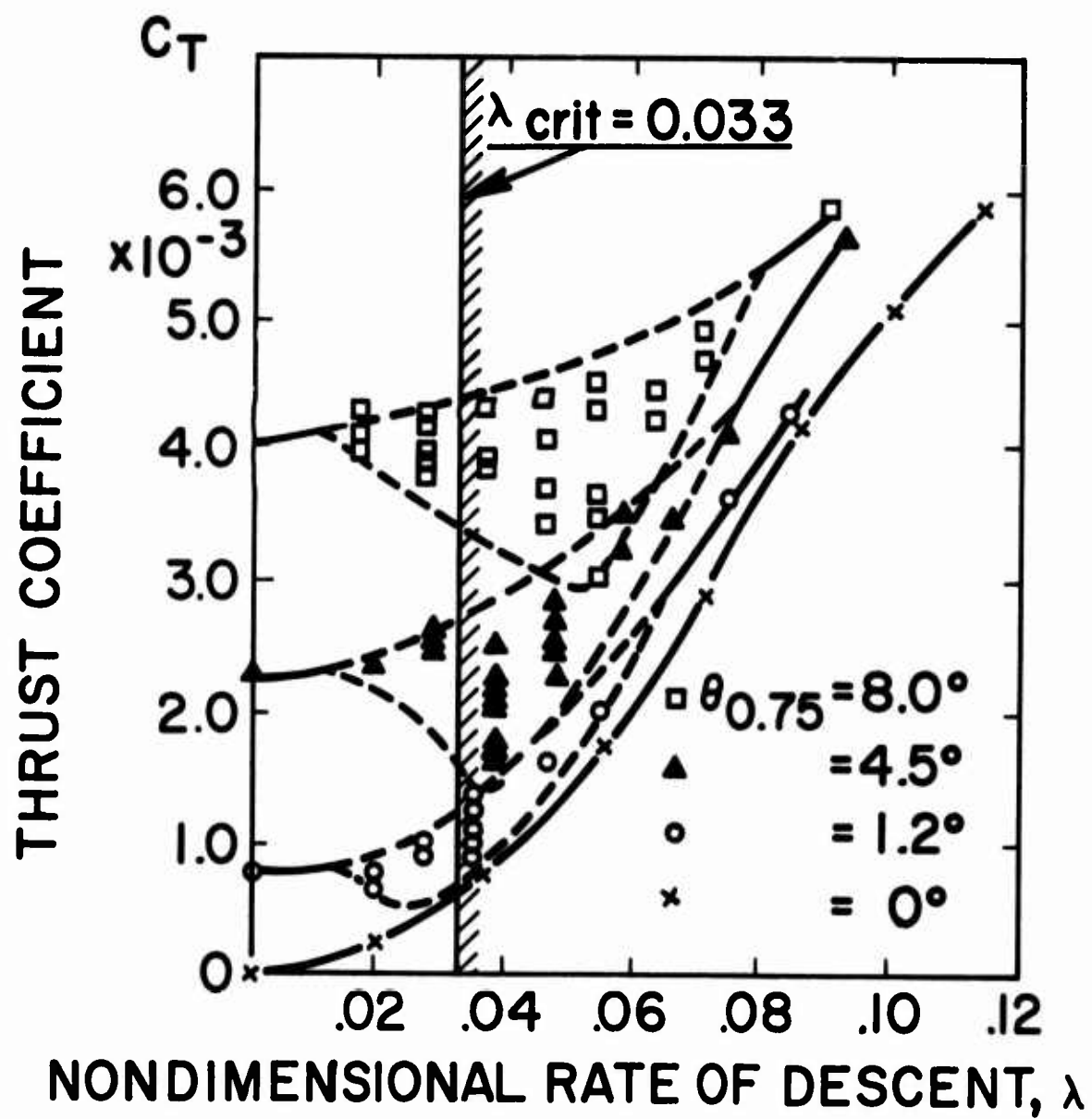
Figure 14. Measured Thrust Coefficient for a Model Helicopter Rotor in Vertical Descent.

31

illustrate the data of Reference 7 for rotor with $\theta_{.75} = 7.5$ degrees and $\alpha = 50$ and 70 degrees. Note that the lower boundary of the induced velocity is close to the momentum theory solutions and that the onset of marked unsteadiness corresponds to the critical condition predicted by Figure 8. This critical condition corresponds to the shaded lines on Figures 15 and 16.

Yaggy and Mort (Reference 18) describe tests on a flapping propeller with the shaft axis inclined at 180, 165, 150, 135, and 120 degrees to the freestream. This corresponds to descent angles of 90, 75, 60, 45, and 30 degrees.* Contours of the thrust fluctuation ΔT (measured from the mean thrust to the peak) divided by the mean thrust $\bar{T}$ are shown for various mean disc loadings $\bar{T}/\pi R^2$, in Figure 7 of Reference 18. Figure 17 illustrates the results for $\bar{T}/\pi R^2 = 16$ lb/ft^2. The vortex-ring boundary has also been calculated assuming $B = 0.86$ and a mean v_h, $\bar{v}_h \triangleq (\bar{T}/2\rho\pi R^2)^{1/2}$. The boundary corresponds to a $\Delta T/\bar{T}$ of between 15% and 25%. A more accurate boundary can be calculated if v is based on the lower value of thrust $\bar{T} - \Delta T$. This is in accord with Figures 15 and 16, which indicate that the minimum induced velocity during the vortex-ring state is approximately equal to the velocity predicted by momentum theory. To follow this suggestion, substitute the critical condition $v = 2V\sin\alpha$ in Eqs. (9) and (10). This gives

$$T - \Delta T = 4\pi R^2 B^2 (V \sin \alpha)^2 / \sin \alpha \qquad (28)$$

The critical rate of descent can be calculated iteratively by first putting $\Delta T = 0$. This gives the solid-line boundary on Figure 17. Since in this case we have knowledge of $\Delta T/\bar{T}$, we can refine the solution by reducing the critical rate of descent in the ratio $(1 - \Delta T/\bar{T})^{1/2}$. The resulting boundary is also shown on Figure 17 as a broken line. Without prior knowledge of $\Delta T/\bar{T}$ (or an estimate), it would be possible to calculate only the solid-line boundary.

Flight Tests

Published data on flight characteristics of helicopters in steep descents are insufficiently complete to permit mapping the boundaries of the vortex-ring region. However, some related data points can be obtained as listed below.

---

* The descent angles of 75, 60, 45, and 30 degrees are necessarily approximate, because Ref. 18 does not give the inclination of the thrust from the shaft axis.
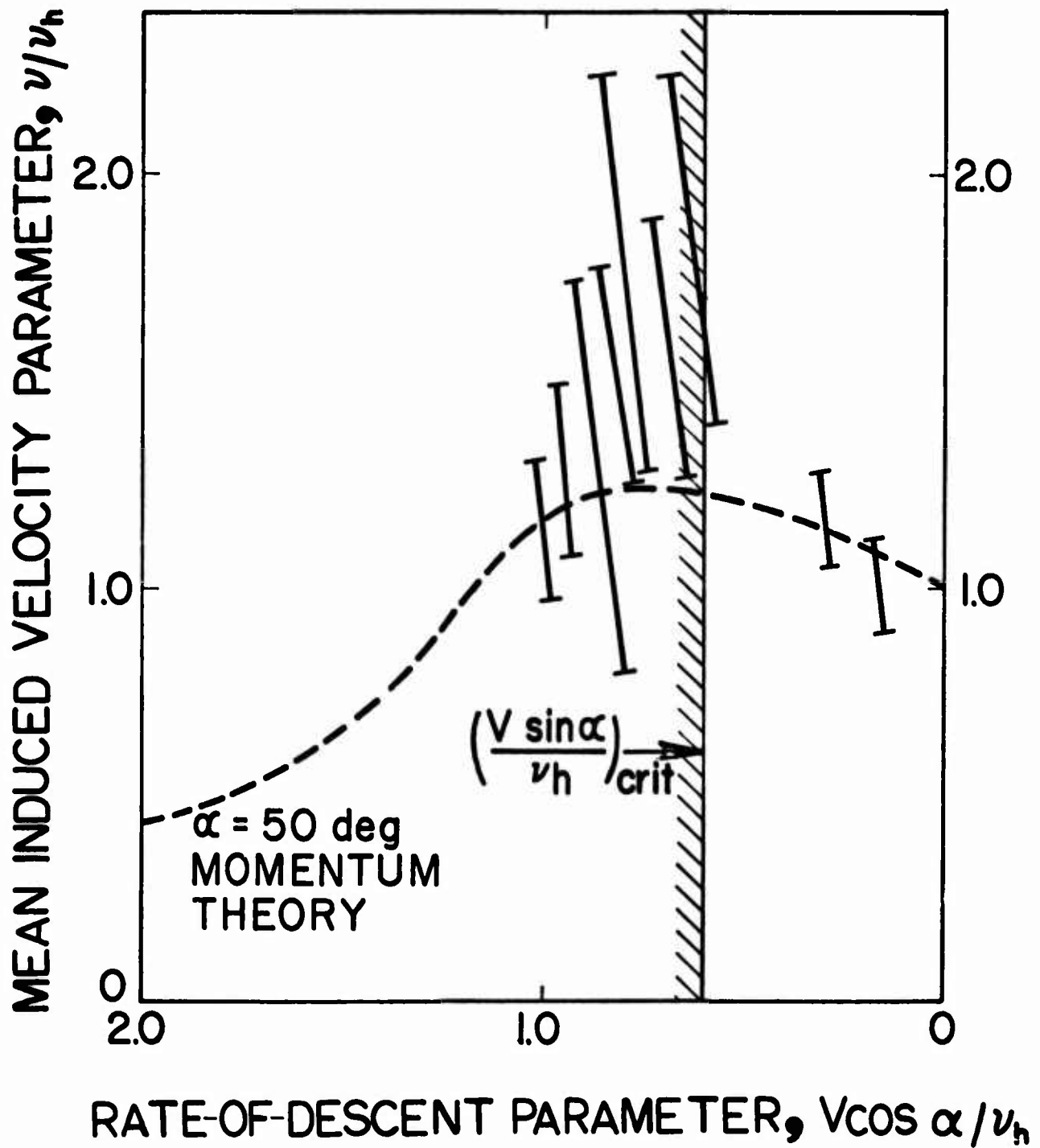
Figure 15. Fluctuations of Mean Induced Velocity, Deduced From Thrust and Torque Measurements, $\alpha = 50$ Degrees.
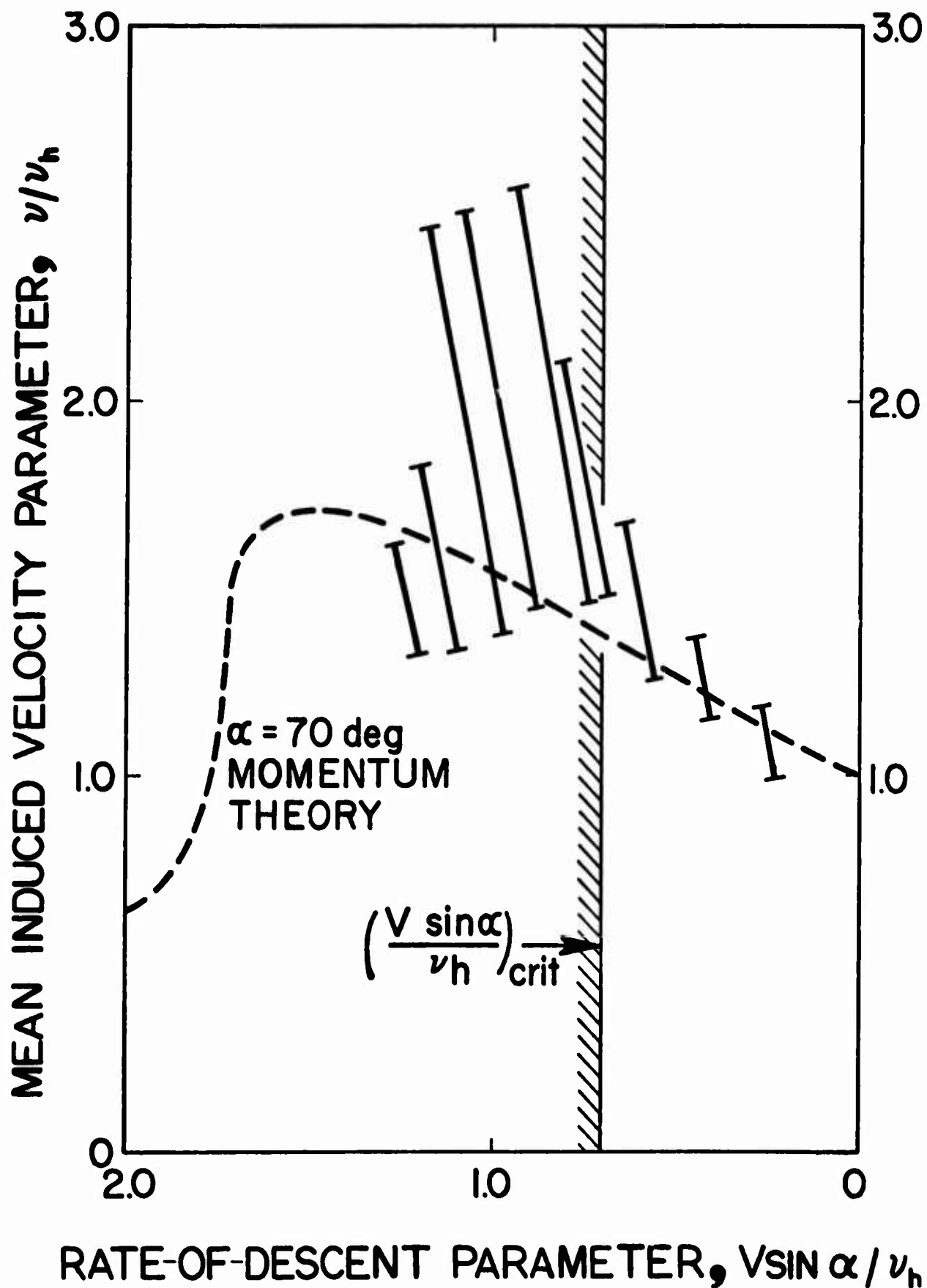
Figure 16. Fluctuations of Mean Induced Velocity, Deduced From
Thrust and Torque Measurements, α = 70 Degrees.
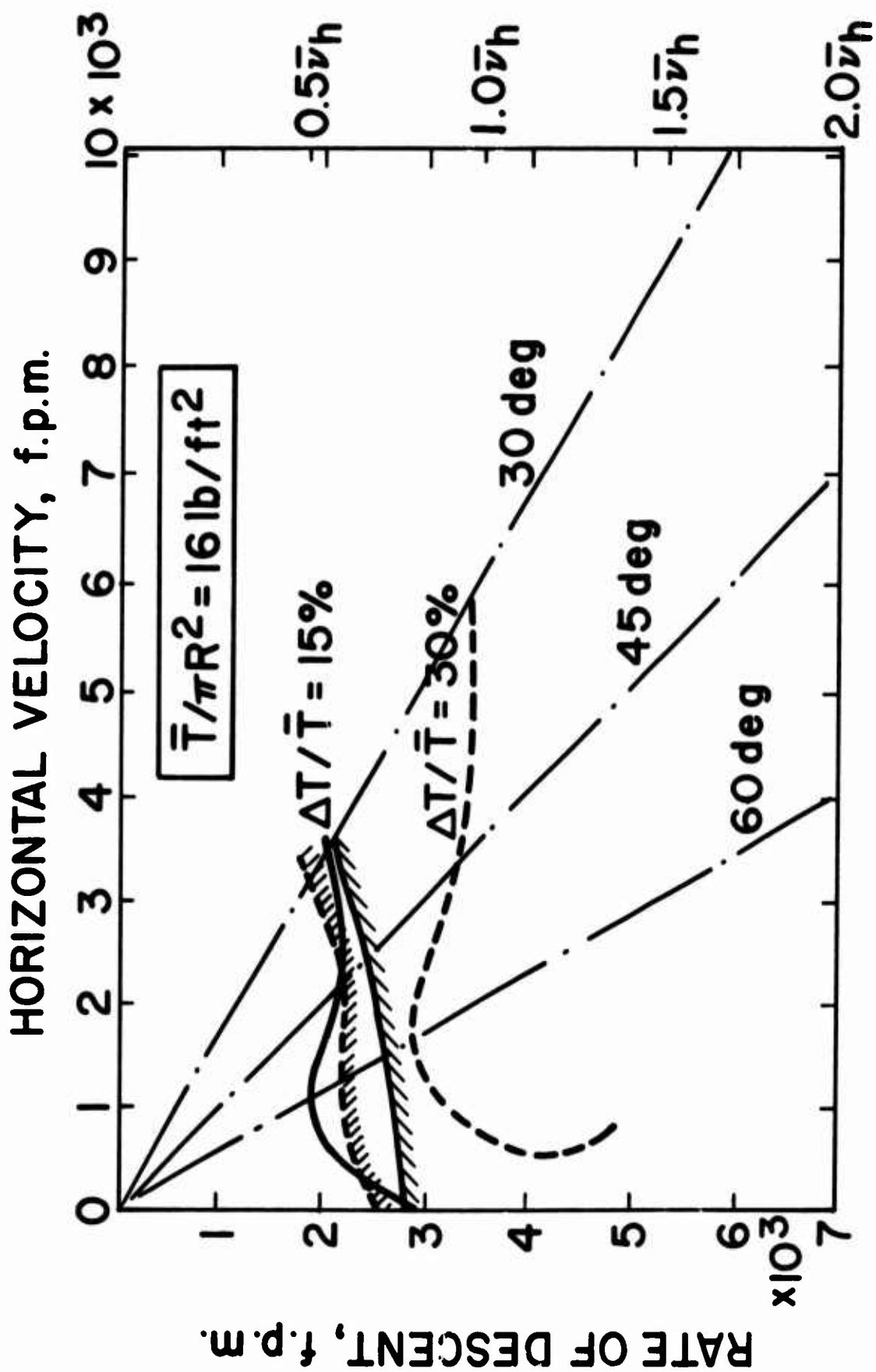
Figure 17. Measured Thrust Fluctuations of a Propeller in Inclined Descent.

Reference 19 notes that for a Westland Whirlwind helicopter, the vortex-ring state was well established at 1500 ft/min vertical descent, corresponding to $V/v_h = 0.84$. Tests on an early helicopter, the Sikorsky R-4B, described in Reference 20, showed onset of roughness in vertical descent at 500 f.p.m. and "shuddering" commencing at 900 f.p.m, corresponding to $0.707v_h$. In the discussion of Reference 21, Bennett states that for the R-4B, the critical rate of descent decreases as forward speed is increased, almost reaching level flight at 60 m.p.h.

The above results are in accord with the theory, but it must be remembered that factors other than the behavior of the rotor itself in the vortex-ring state may influence helicopter flying qualities in descents. The unsteady flow may induce large pitching moments on the fuselage. Reference 22 discusses this phenomenon, noting that the size and cross-section of the fuselage tail cone have an important effect. For example, the R-4B had particularly bad characteristics in the vortex-ring state because of its thick slab-sided rear fuselage. Quite apart from considerations of unsteady flow, changes in derivatives may affect flying qualities. Reference 19 notes that the magnitude of the plunge damping derivative, Z_w, decreases markedly between hover and the vortex-ring state. This trend is confirmed by the data of Reference 18. If $|Z_w|$ becomes sufficiently small, the helicopter's flying qualities will be degraded.

The Lower Boundary of the Vortex-Ring State

After entering the vortex-ring state, if the rate of descent is increased, eventually steady flow is re-established. The horizontal speed and rate of descent at which this occurs define the lower boundary of the vortex-ring state. The practical importance of the vortex-ring state depends, in part, on the distance between the lower and upper boundaries on the $V \cos \gamma$, $V \sin \gamma$ hodograph plane. If large areas of the plane are associated with unsteady flow, the operational utility of the helicopter will be correspondingly reduced.

A critical condition for the lower boundary will now be derived. As before, we postulate that the unsteady flow is associated with a breakdown in the protective sheath of vorticity surrounding the slipstream. However, for the lower boundary the "pileup" of vorticity occurs some distance above the rotor, as shown in the flow model of Figure 18.

---

* See Ref. 34 for an explanation of the influence of Z_w on handling qualities.
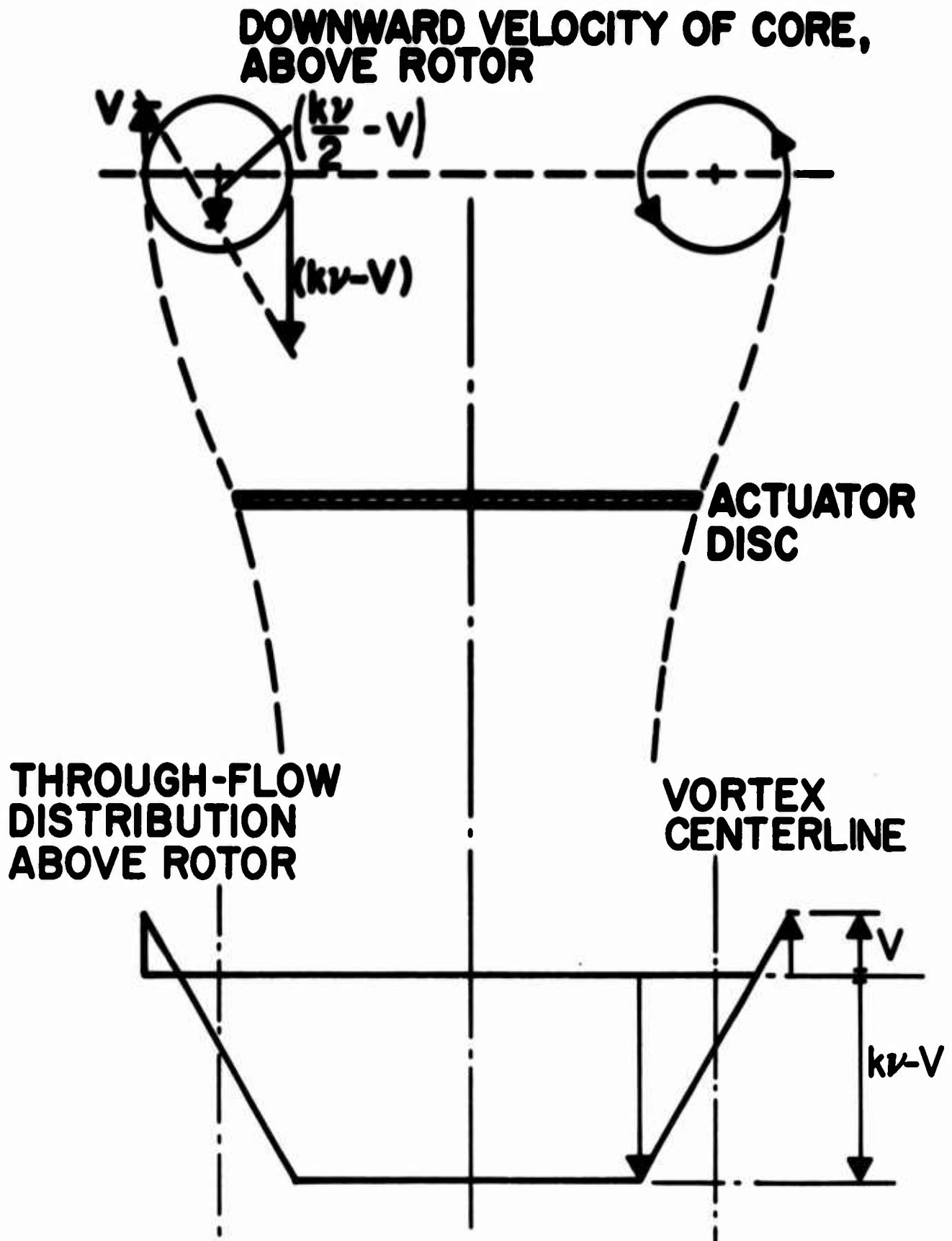
Figure 18. Flow Model for Lower Boundary of Vortex-Ring
State in Vertical Descent.
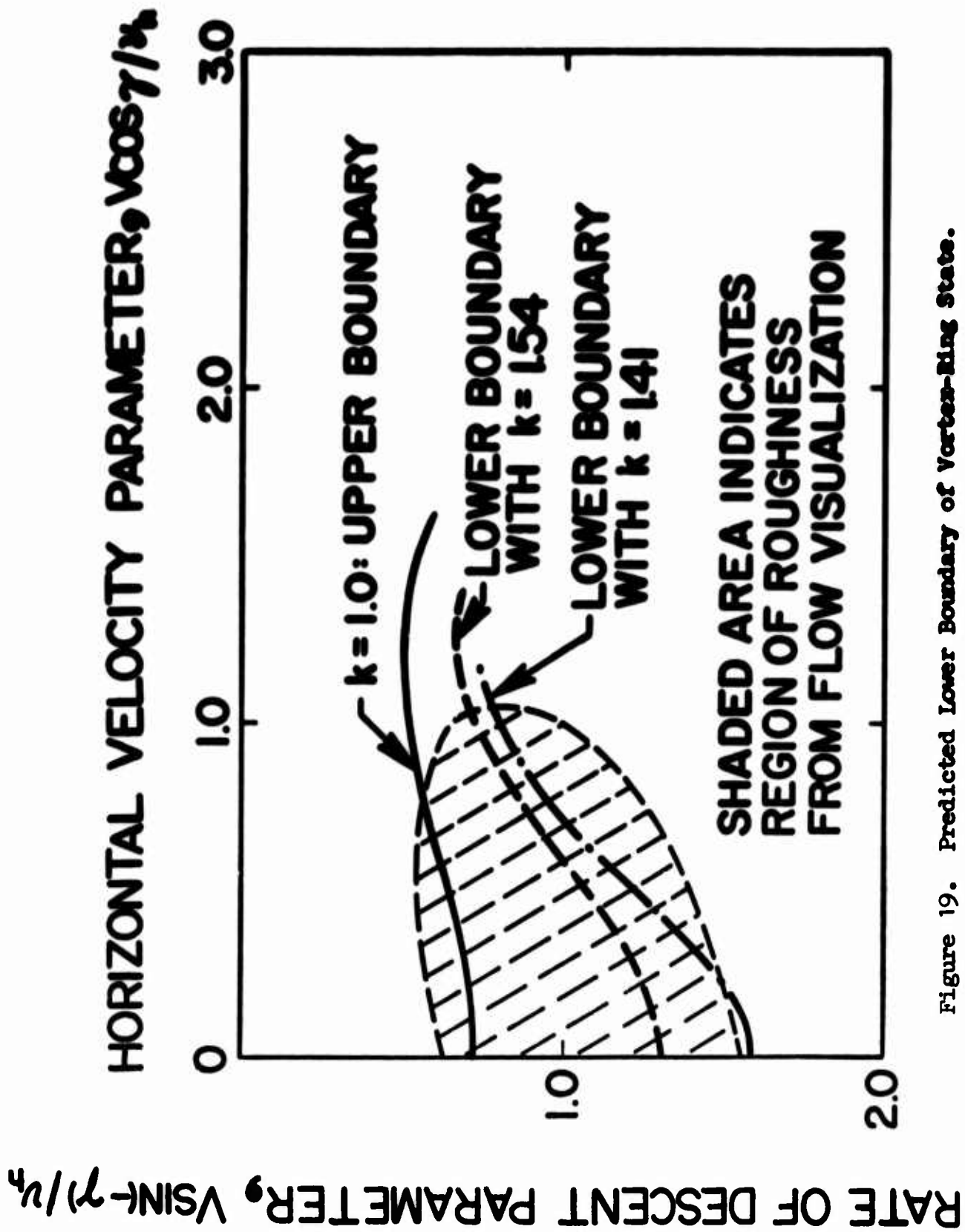
Figure 19. Predicted Lower Boundary of Vortex-Ring State.

Using momentum theory and the flow model of Figure 18, the critical condition is derived as follows. Inside the slipstream the induced velocity is kv, where the value of k varies from 1.0 at the rotor disc to 2.0 at infinity. The rate of ascent of the vortices is $V_{sink}-(kv/2)$. In determining the upper boundary, conditions at the disc are relevant, and so a value of $k = 1.0$ was used, giving the critical condition as Eq. (3), or more generally, Eq. (16). For the lower boundary the choice of k is not so clear-cut. At infinity $k = 2$, but this value is inappropriate because an accumulation of vorticity at infinity would not cause unsteady flow to be reflected back to the rotor. Therefore, the value of k must be less than 2.0. Tentatively, $1.4 < k < 1.6$ is suggested. Cross-plotting lines of slope $2/k$ on Figure 8 with $k = 1.41$ and $k = 1.54$ gives a lower boundary as indicated on Figure 19.

It is interesting to note that the "region of roughness" reported by Drees in Reference 11 on the basis of flow visualization agrees approximately with the predicted boundaries at low speeds.

The lower boundary is not as sharply defined as the upper boundary, in that the development of unsteady flow is less sudden (see, e.g., Figure 13). One would expect this, because the accumulation of vorticity and consequent breakdown of the slipstream are occurring farther away from the rotor. One would also expect momentum theory to become less accurate for predicting the lower boundary at higher forward speed, because distortion of the slipstream, rolling up of vortices, and other viscous phenomena not included in the theory become more important as the critical region moves away from the rotor with increase of k.

Tandem Rotors

Reference 17 describes experiments on tandem rotors in vertical and inclined descent. Data on fluctuating inflow (similar to Figures 15 and 16) are presented, normalized with respect to alternative parameters v_h and v_{h_e} where $v_h \overset{\Delta}{=} T/2\rho\pi R^2$, $v_{h_e} \overset{\Delta}{=} T/2\rho S_e$, where T = thrust per rotor, and S_e is one-half the projected area of the tandem rotors. The overlap between the rotors is small, so for the configuration of Reference 17, S_e should be defined in this way for momentum theory calculations; Reference 6, p. 312, suggests a larger area. This is the area formed by two semicircles of radius equal to the rotor radius, with centers spaced a distance equal to the hub separation of the actual configuration, plus the area enclosed by straight lines joining the semicircles.

39

The experimental data of Reference 17 indicate that severe induced flow fluctuations occur at a slightly lower value of $\dfrac{V}{v_h}$ than that for the single-rotor configuration. However, the periodicity noted in Reference 7 is hardly observable. Because of the mutual induction effect of tandem rotors, it is expected that the theory proposed here will require modification for such configurations.

III.5 SUMMARY AND RECOMMENDATIONS

Summary

1. The boundaries of the vortex-ring state can be predicted by momentum theory as described in this chapter. The predicted upper boundary corresponds to measured mean-to-peak thrust fluctuations of approximately 15% of the mean thrust.

2. In vertical descent, the upper boundary is approximately 0.707 times the mean induced velocity at hover. For inclined descents, the upper boundary is very sensitive to parasite drag, and for helicopters with large parasite drag, the vortex-ring state may vanish for descent angles shallower than 20 degrees.

Recommendations

1. Improved helicopter steep descent capability requires a more complete understanding of the vortex-ring state. The "upper" (k = 1) boundary is of principal interest for helicopters; but for STOL aircraft with reverse-pitch propellers descent angle is limited by the "lower" (k = 1.5) boundary, as shown in Figure 20. Further knowledge of the vortex-ring state is thus of importance in obtaining steep, slow flight of propeller-driven STOL aircraft as well as helicopters.

2. The present theory is limited by the assumptions of momentum theory, e.g., the rather arbitrary Glauert-Kussner hypothesis regarding the "area of capture" and the assumption of uniform induced velocity across the disc. Greater accuracy could be obtained by using more refined theories. A further area for exploration by such theories is the nature of the flow within the vortex-ring state. For example, it appears that the accumulation of vorticity either at or above the disc increases the induced velocity at the disc, thus removing the accumulated vorticity and returning the flow to that predicted by momentum theory. In turn, this causes the vorticity to re-accumulate, causing a cyclic oscillation characteristic of the vortex-ring state. Mathematical formulation of this physical model probably lies beyond the grasp of momentum theory.

3. Although the upper boundary is fairly sharply defined, slight unsteadiness does occur at smaller rates of descent, and even
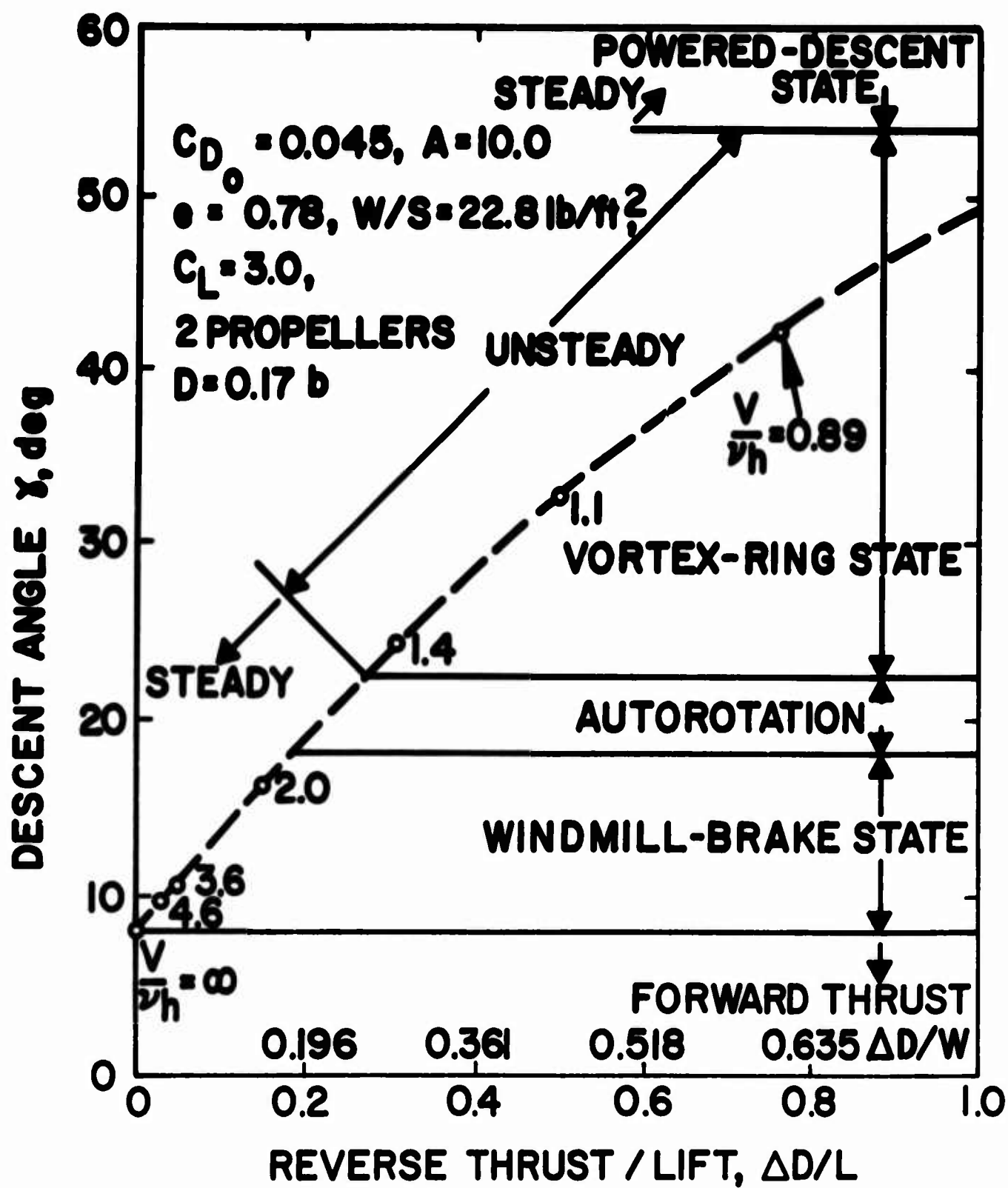
Figure 20.   Effect of Reverse-Thrust Propellers
on Descent Angle of a STOL Aircraft.

at hover according to the data of Reference 23. A more sophisticated theory is required to analyze this phenomenon.

4. More experimental data on the vortex-ring state are required. The present analysis could serve as a guide to the test conditions of primary interest.

5. The implications of the vortex-ring state on handling qualities and operational maneuvers require investigation. Suitable automatic control of collective pitch may smooth the thrust fluctuations sufficiently to permit comfortable, controlled flight at all descent speeds and angles.

CHAPTER IV. THRUST OF AN ISOLATED DESCENDING ROTOR

IV.1. INTRODUCTION AND SUMMARY

Standard methods for calculating helicopter stability
derivatives are based on momentum and blade-element theories (e.g.,
References 24, 25). As will be shown, these procedures do not
give good agreement with experimental data on rotors in descending
flight. This chapter therefore presents an analysis of rotors in
vertical descent using conventional momentum and blade-element
assumptions, plus some additional refinements. These include:

(i)   nonuniform downwash associated with rotor tip
        vortices

(ii)   the loss of lifting effectiveness of the tips
        due to three-dimensional flow (i.e., "spillage")

With these factors included, the theory agrees well with experiment.

The basic flow model is shown in Figure 6. The tip
vortices are modeled by vortex cores with boundary conditions
matched inside and outside the slipstream. This, of course, is a
highly simplified model of the actual flow, neglecting swirl, non-
uniform downwash due to non-ideal blade twist, unsteady effects, etc.
However, this model gives results which are sufficiently accurate
for stability and control calculations, predicting derivatives to
within $\pm$ 20% accuracy.

The chapter is organized as follows. In Section 2, mass
flow, momentum, and energy relationships are derived for the assumed
flow model, with the ratio of the parallel sides of the trapezoidal
distribution left variable. These basic relationships relate
conditions at the rotor disc to those in the ultimate wake. Because
of the nonuniform flow at the outer edge of the slipstream, the rela-
tionships are more complicated than for the standard model where
the flow is assumed to be uniform across the slipstream. Section 3
expresses rotor thrust in terms of blade-element angles of attack,
taking into consideration the trapezoidal induced velocity profile.
In Section 4 the vortex core model boundary conditions are established
in order to fix the geometry of the trapezoidal distribution both at
the disc and in the ultimate wake.

Section 5 discusses the loss of lifting effectiveness of blade elements near the tips due to three-dimensional flow. This is usually accounted for by a "tip loss factor", i.e., defining an effective rotor radius BR where $B = 1 - \sqrt{2c_T}/b$. This factor gives reasonable accuracy at hover, but it is not apparent how B should be modified for nonhovering conditions. Section 5 therefore presents an alternative derivation of B based on considerations of the loading at the rotor tips rather than the average loading per blade. This permits B to be calculated in a logical fashion for nonhovering conditions. It does, however, lead to a cyclic variation of B which causes some additional complication in calculating derivatives. The procedure adopted for incorporating a cyclic B in the rotor blade time history calculations is too detailed for discussion in the main text of the report and is therefore discussed in Appendix II, in conjunction with the description of the subroutine SWEEP which integrates the blade-element loads radially and with respect to time.

Section 6 shows how the tip loss factor B can be combined with the preceding analysis to compute thrust versus rate of descent for a given rotor. Section 7 compares theoretical predictions with wind-tunnel data on a descending rotor. Because no satisfactory data were available for inclined descent, it was not possible to validate the assumed cyclic component of tip losses, but good agreement is obtained with data for vertical descent for which only noncyclic tip losses are predicted.

Axial Velocity Distribution

A trapezoidal velocity distribution such as that shown in Figure 6 can be described as follows:

$$v(x) = \begin{cases} v - V & 0 \leq x \leq 1-\delta \\ \dfrac{v}{\delta}(1-x) - V & 1-\delta \leq x \leq 1 \end{cases} \tag{29}$$

This distribution can be nondimensionalized by dividing through by ΩR. The result is

$$\alpha(x) = \begin{cases} \lambda - \Lambda & 0 \leq x \leq 1-\delta \\ \dfrac{\lambda}{\delta}(1-x) - \Lambda & 1-\delta \leq x \leq 1 \end{cases} \tag{30}$$

The above equations apply near the rotor disc. Similar expressions hold in the wake, except that α_w is used in lieu of α. Of course, λ_w and δ_w must be used in the α_w expression corresponding to Eq. (30). In general, $\lambda_w \neq \lambda$ and $\delta_w \neq \delta$, but Λ is the same everywhere and requires no special subscript.

Mass Flow

The mass flow through the rotor disc can be obtained by integrating the trapezoidal velocity distribution over the entire disc. The result is

$$\dot{m} = \int_0^R 2\pi s \, \rho \, v\left(\frac{s}{R}\right) ds \tag{31}$$

$$\dot{m} = \rho\pi R^2 \Omega R \left[2\int_0^1 x\alpha(x)\,dx \right] \tag{32}$$

$$M_f = 2\int_0^1 x\alpha(x)\,dx \tag{33}$$

46

In the distant wake, Eq. (32) is applicable with R_w^2 substituted for R^2 in the area factor (note: the R in the ΩR factor remains nonsubscripted because this term was used to transform v_w and V to their nondimensional forms λ_w and Λ).

$$\dot{m} = \rho \pi R_w^2 \Omega R \left[2\int_0^1 x\alpha_w(x)dx \right] \qquad (34)$$

Dividing (34) by (32) and rearranging,

$$\epsilon \overset{\Delta}{=} \frac{R_w}{R} = \sqrt{\frac{\int_0^1 x\alpha(x)dx}{\int_0^1 x\alpha_w(x)d_x}} \qquad (35)$$

Momentum Considerations

The momentum flux of the air that is eventually encountered by the rotor while it moves in the distant atmosphere is

$$F_o = -\dot{m}V \qquad (36)$$

where positive F is downward.

In the distant wake, the momentum flux is calculated by integrating the trapezoidal distribution:

$$F_w = \int_0^{R_w} 2\pi s \rho v_w^2 \left(\frac{s}{R_w}\right) ds \qquad (37)$$

Nondimensionalizing the integral,

$$F_w = \rho \pi R_w^2 (\Omega R)^2 \left[2\int_0^1 x\alpha_w^2(x)dx \right] \qquad . \qquad (38)$$

or

$$F_w = \pi R^2 \rho (\Omega R)^2 \epsilon^2 \left[2\int_0^1 x\alpha_w^2(x)dx \right] \qquad (39) .$$

47

Clearly, the change in momentum flux must equal the rotor thrust.

$$T = + \dot{m}V + \pi R^2 \rho (\Omega R)^2 \epsilon^2 \left[2\int_0^1 x \alpha_w^2(x)dx \right] \tag{40}$$

Nondimensionalizing with the help of Eq. (33),

$$C_T = M_f \Lambda + \epsilon^2 \left[2\int_0^1 x \alpha_w^2(x)dx \right] \tag{41}$$

An alternative form to (41) is

$$C_T = 2\int_0^1 x \left[\Lambda\alpha(x) + \epsilon^2 \alpha_w^2(x) \right]dx \tag{42}$$

Energy (Power) Considerations

The energy flux (power) in the air before it reaches the rotor (i.e., when this air is in the distant atmosphere) is given by

$$P_0 = 1/2 \; mV^2 \tag{43}$$

The power added to the air by the rotor is

$$P_R = \int_0^R v(x)dT = \int_0^1 v(x)\left(\frac{dT}{dx}\right)dx \tag{44}$$

Eq. (44) can be verified from either force and momentum considerations or blade element considerations.

48

The assumed blade element has span ds and produces lift dL. The shaft torque produced by this element is

$$dQ = sdL \sin\alpha_i$$

For small α_i, $\alpha_i \approx \sin\alpha_i \approx \tan\alpha_i \approx \dfrac{v(x)}{\Omega s}$.

Then the torque is

$$dQ = s \frac{v(x)dL}{\Omega s} = \frac{v(x)dL}{\Omega}$$

Multiplying through by Ω and integrating,

$$Q\Omega \overset{\triangle}{=} P_R = \int_0^R v(x)dt = \int_0^1 v(x) \frac{dL}{dx} dx$$

Eq. (44) can be easily nondimensionalized. Putting $L \overset{\sim}{=} T$,

$$P_R = \pi R^2 \rho (\Omega R)^3 \int_0^1 \alpha(x) \left(\frac{d\,C_T}{dx} \right) dx \tag{45}$$

The power in the distant wake is assumed to be completely embodied in kinetic energy flux; i.e., the ambient pressure in the distant wake has returned to atmospheric pressure.

In the distant wake, currents flow in radial, tangential, and axial directions. The power could be broken into three corresponding portions denoted by the subscripts r, t, and a.

$$P_w = P_{rw} + P_{tw} + P_{aw} \tag{46}$$

The radial flows occur because of vortices (and vortex cores) in the wake. Tangential flows occur due to "swirl", which is caused by momentum imported to the slipstream by rotor shaft torque. The axial power is associated with the assumed trapezoidal velocity distribution.

Assume for the present that $P_r + P_t \ll P_a$. The axial power comes from integration of the trapezoidal distribution:

49

$$P_W = \int_0^{R_W} (1/2)\rho 2\pi s\, v_w{}^3\left(\frac{s}{R}\right) ds \qquad (47)$$

In the usual manner, the right-hand side of (47) is non-dimensionalized.

$$P_W = (1/2)\rho\pi R_w{}^2(\Omega R)^3\left[2\int_0^1 x\alpha_w{}^3(x)dx\right]$$

or

$$P_W = 1/2\ \pi R^2\rho(\Omega R)^3\epsilon^2\left[2\int_0^1 x\alpha_w{}^3(x)dx\right] \qquad (48)$$

The following balance of power must exist:

$$P_W = P_R + P_o \qquad (49)$$

Substituting (43), (45) and (48) into (49),

$$(1/2)\pi R^2\rho(\Omega R)^3\epsilon^2\left[2\int_0^1 x\alpha_w{}^3(x)dx\right] = \pi R^2\rho(\Omega R)^3\int_0^1\alpha(x)\left(\frac{dC_T}{dx}\right)dx + (1/2)\dot{m}V^2, \text{ or}$$

$$\epsilon^2\int_0^1 x\alpha_w{}^3(x)dx = \int_0^1\alpha(x)\left(\frac{dC_T}{dx}\right)dx + \Lambda^2\int_0^1 x\,\alpha(x)dx$$

This equation can be refined further after the blade element analysis, which follows, provides an expression for dC_T/ds. Looking ahead to Eq. (58),

$$\frac{dC_T}{dx} = \frac{\sigma a}{2}x[\theta_t - \alpha(x)]$$

Hence,

$$\epsilon^2\int_0^1 x\alpha_w{}^3(x)dx = \frac{\sigma a}{2}\int_0^1 x[\theta_t - \alpha(x)]\alpha(x)dx + \Lambda^2\int_0^1 x\alpha(x)dx$$

$$\qquad (50)$$

50

Up to this point, we have discussed only the mass flow, momentum, and energy in the slipstream, using the assumed trapezoidal distribution of induced velocity. Eqs. (33), (34), (35), (42) and (50) summarize the principal results. The next section develops the blade-element expressions for the rotor.

IV.3.   BLADE-ELEMENT CONSIDERATIONS

If $x \leq 1-\delta$, the axial velocity is constant and equal to $v-V$. In this region the thrust per blade is

$$dT_b = 1/2\ \rho(\Omega s)^2 ac\left[\theta - \frac{(v-V)}{\Omega s}\right]ds \qquad 0 \leq s \leq R(1-\delta) \qquad (51)$$

Assume the twist distribution*

$$\theta = \frac{R}{s}\theta_t \qquad (52)$$

Then

$$dT_b = 1/2\ \rho(\Omega s)^2\ ac\left[\frac{\theta_t\ \Omega R}{\Omega s} - \frac{(v-V)}{\Omega s}\right]ds$$

$$= 1/2\ \rho(\Omega s)ac\left[\Omega R\theta_t + V - v\right]ds \qquad (53)$$

Comparing this expression to the Kutta-Joukowski expression with $T \cong L$, one sees that

$$\frac{dT_b}{ds} = \rho V \Gamma \qquad (54)$$

Γ is constant for $0 \leq x \leq 1-\delta$ and is given by the expression

$$\Gamma = 1/2\ ac\left[\Omega R\ \theta_t + V - v\right] \qquad 0 \leq x \leq 1-\delta \qquad (55)$$

Since $\Gamma \rightarrow 0$ at the tip, the Γ strength given by (55) must shed as training vortices over the region $1-\delta \leq x \leq 1$.

----

*This distribution is usually called "ideal twist", since it causes uniform inflow (v constant over the disc), and constant circulation along the blade bound vortex system, i.e., in Eq. 55 Γ is constant for ideal twist.

From this system, it seems reasonable to assume that the Γ strength fed to the vortex core is given by (55). Nondimensionalizing (27), assuming constant chord c,

$$\Gamma = \frac{\sigma a}{2b} \ \pi R^2 \Omega \left[\theta_t + \Lambda - \lambda\right] \tag{56}$$

Continuing with the blade-element theory, from Eq. (53)

$$dT_b = 1/2 \ \rho(\Omega s) \ ac \left[\Omega R \theta_t - v(x)\right] ds \tag{57}$$

where $v(x)$ has been substituted for v-V in Eq. (53). Note that Eq. (57) holds over the entire blade, unlike Eq. (53).

$$dT_b = 1/2 \ \rho\Omega sac \left[\Omega R \theta_t - v(x)\right] ds$$

$$= 1/2 \ \rho(\Omega R)^2 Rac \ x\left[\theta_t - \alpha(x)\right] dx$$

$$= 1/2 \ \rho(\Omega R)^2 \pi R^2 a \ \frac{bc}{\pi R} \left(\frac{1}{b}\right) x\left[\theta_t - \alpha(x)\right] dx \tag{58}$$

For all b blades, the thrust expression becomes

$$dT = 1/2 \ \pi R^2 \rho(\Omega R)^2 \ a\sigma \ x\left[\theta_t - \alpha(x)\right] dx$$

For the case when the blade chord is constant, this thrust expression can be integrated and nondimensionalized to yield the equation

$$C_T = \frac{\sigma a}{4} \left\{ \theta_t - 2\int_o^1 x \ \alpha(x) dx \right\} \tag{59}$$

Note that the integral in (59) also appears in (33). Thus, an alternative form of (59) is

$$C_T = \frac{\sigma a}{4} \left(\theta_t - M_f\right) \tag{60}$$

IV.4.   VORTEX CORE MODEL

The trapezoidal induced velocity distribution shown in Figure 6 is composed of a uniform distribution plus two idealized vortex cores. These cores have a tangential velocity V_t which increases linearly with distance from the center of the vortex core until the core radius $R\delta/2$ is reached, beyond which point the vortex is assumed to induce no velocity either inside or outside the slipstream. Of course, this is a very simplified representation of the actual flow, and to obtain accurate results with this model, some consideration must be given to the characteristics of real viscous vortices. This forms the main topic of this section.

A viscous vortex model is given in Reference 27 which has the tangential velocity profile

$$V_t(r,t) = \frac{\Gamma}{2\pi r} \left(1 - e^{-r^2/4\nu_e t}\right) \tag{61}$$

This velocity distribution for some time, t, is shown in Figure 21.

For $r < r_c$, the model tends toward the simple inviscid vortex model

$$V_t = \frac{\Gamma}{2\pi r}$$

For $r < r_c$, the velocity profile tends toward that of a rigid body spinning at a rate ω, where

$$\omega = \frac{V_{max}}{r_c} \tag{62}$$

It was shown in Chapter III that the boundary condition required to fit the peripheral velocities of a vortex core to the slipstream velocities of a descending rotor is

$$\nu = 2V_t \tag{63}$$

where V_t is the tangential velocity of the core.

54
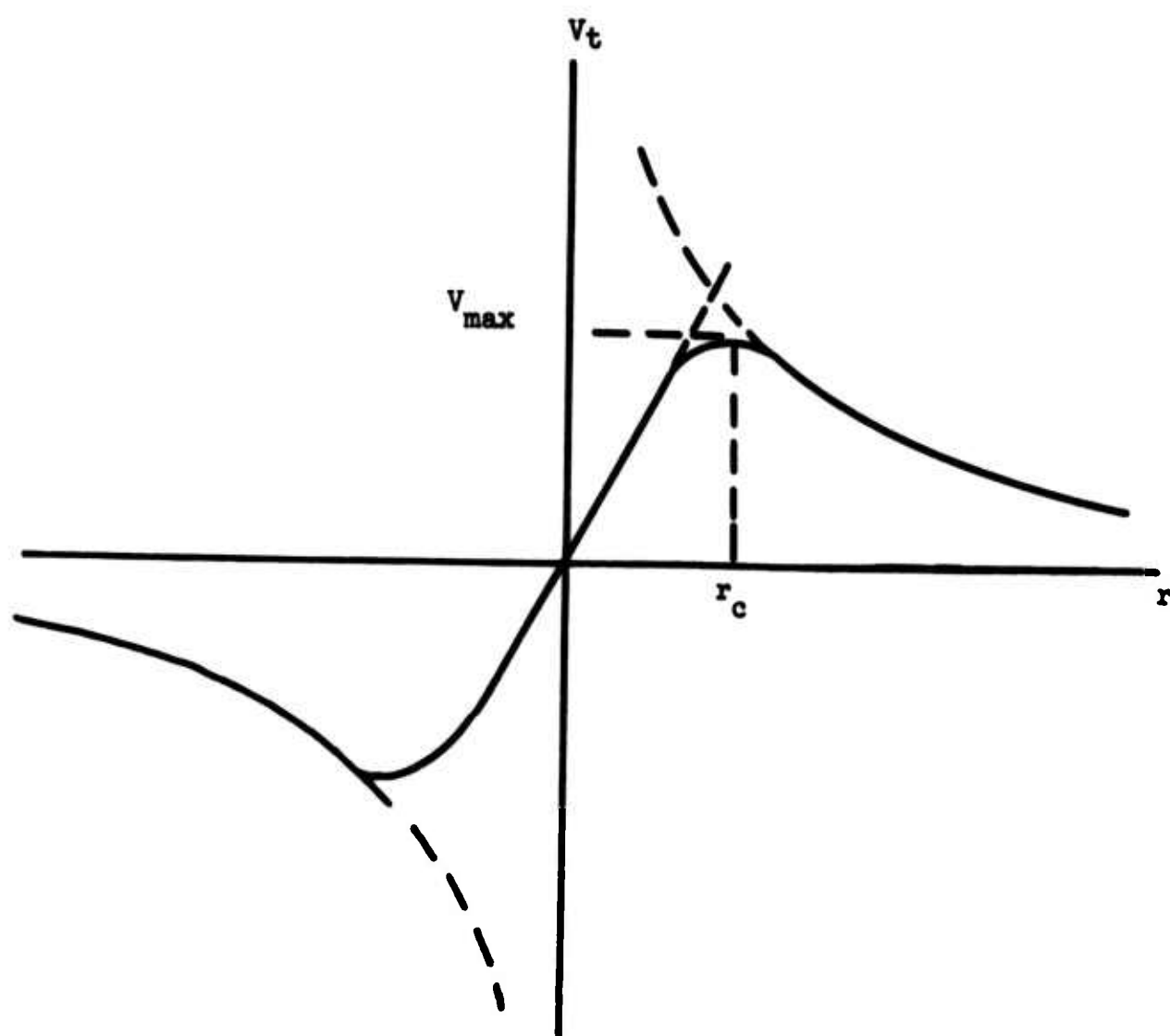
Figure 21. Vortex Model.

55

Assume that $V_t = V_{max}$ as depicted by Figure 21. Then Eq. (63) can be used to determine r_c, which will later be related to the coordinate δ on the trapezoidal velocity distributions.

To determine r_c, one must first differentiate Eq. (61) with respect to r:

$$\frac{\partial V(r,t)}{\partial_r} = \frac{\Gamma}{2\pi}\left[\frac{r\left(\frac{r}{2\nu_e t}\right)e^{-\frac{r^2}{4\nu_e t}} - \left(1 - e^{-\frac{r^2}{4\nu_e t}}\right)}{r^2}\right]$$

V_{max} occurs when this derivative vanishes, leaving the result

$$r_c\left(\frac{r_c}{2\nu_e t}\right)e^{-\frac{r_c^2}{4\nu_e t}} = 1 - e^{-\frac{r^2}{4\nu_e t}} \tag{64}$$

For simplicity, define

$$\zeta \triangleq \frac{r_c^2}{4\nu_e t} \tag{65}$$

Then (64) is written

$$1 + 2\zeta = e^\zeta \tag{66}$$

The approximate numerical solution to this equation is

$$\zeta \cong 5/4 \triangleq \zeta_s \tag{67}$$

as can easily be determined by direct substitution.

56

Combining (65) and (67),

$$4v_e t = \frac{r_c^2}{\zeta_s} \tag{68}$$

and substituting (68) into (61) to get V_{max},

$$V_{max} = \frac{\Gamma}{2\pi r_c} \left(1 - e^{-\frac{r_c^2 \zeta_s}{r_c^2}} \right) = \frac{\Gamma}{2\pi r_c} \left(1 - \frac{1}{e^{\zeta_s}} \right) \tag{69}$$

Using (66) to substitute for e^{ζ_s},

$$V_{max} = \frac{\Gamma}{2\pi r_c} \left(1 - \frac{1}{1 + 2\zeta_s} \right)$$

$$V_{max} = \frac{\Gamma}{\pi r_c} \left(\frac{\zeta_s}{1 + 2\zeta_s} \right) \tag{70}$$

Using the value 5/4 for ζ_s as given by (67), Eq. (70) becomes

$$V_{max} = \frac{5\Gamma}{14\pi r_c} \tag{71}$$

Assuming that $V_t = V_{max}$, Eqs. (63) and (71) can be combined to get

$$v = \frac{5\Gamma}{7\pi r_c}$$

or

$$r_c = \frac{5\Gamma}{7\pi v} \tag{72}$$

57

Eq. (72), when applied to the cores near the rotor, can be manipulated to get (since $\delta = 2r_c/R$)

$$\delta = \frac{10\Gamma}{7\pi R \nu} \tag{73}$$

The value of Γ applies for a single blade and is given by Eq. (56).

the Γ strength of the cores is constant. Thus,

$$\delta_w = \frac{10\Gamma}{7\pi R_w \nu_w} \tag{74}$$

An alternative form for (74) would be

$$\delta_w = \frac{10\Gamma}{7\pi R \nu_w \epsilon} \tag{75}$$

At this point, it is appropriate to combine Eqs. (56), (73) and (75).

$$\delta = \frac{10\Gamma}{7\pi R \nu} = \frac{10}{7\pi R(\Omega R)\lambda} \left(\frac{\sigma a}{2b}\right)\pi R^2 \Omega \ (\theta_t + \Lambda - \lambda)$$

$$\delta = \left(\frac{5\sigma a}{7b}\right) \frac{\theta_t + \Lambda - \lambda}{\lambda} \tag{76}$$

$$\delta_w = \left(\frac{5\sigma a}{7b}\right) \frac{\theta_t + \Lambda - \lambda}{\lambda_w \epsilon} \tag{77}$$

Having related the core model to the flow inside and outside the slipstream, the next step in calculating the rotor thrust is to allow for tip losses due to three-dimensional flow, or "spillage". This is discussed in Section 5.1 but before beginning that topic, it is convenient to summarize the major equations obtained up to this point and to restate them in convenient nondimensional forms.

58

Equation Summary

$$\alpha(x) = \begin{cases} \lambda - \Lambda & 0 \le x \le 1-\delta \\ \dfrac{\lambda}{\delta}(1-x) - \Lambda & 1-\delta \ x \le 1 \end{cases}$$

Flow model $\qquad\qquad\qquad\qquad\qquad\qquad\qquad\qquad\qquad\qquad\qquad\qquad$ (30)

$$\alpha_w(x) = \begin{cases} \lambda_w - \Lambda & 0 \le x \le 1-\delta_w \\ \dfrac{\lambda_w}{\delta_w}(1-x) - \Lambda & 1-\delta_w \le x \le 1 \end{cases}$$

Continuity $\quad \epsilon = \sqrt{\dfrac{\displaystyle\int_0^1 x\,\alpha(x)\,dx}{\displaystyle\int_0^1 x\,\alpha_w(x)\,dx}}$ $\qquad\qquad\qquad\qquad\qquad$ (35)

Momentum $\qquad C_T = 2\Lambda\displaystyle\int_0^1 x\alpha(x)\,dx + 2\epsilon^2\displaystyle\int_0^1 x\,\alpha_w^{\ 2}(x)\,dx$ $\qquad$ (42)

Energy $\qquad \epsilon^2\displaystyle\int_0^1 x\,\alpha_w^{\ 3}(x)\,dx = \dfrac{\sigma a}{2}\displaystyle\int_0^1 x(\theta_t - \alpha(x))\,\alpha(x)\,dx$

$\qquad\qquad\qquad\qquad\qquad\qquad\qquad + \Lambda^2\displaystyle\int_0^1 x\alpha(x)\,dx$ $\qquad\qquad\qquad$ (50)

Blade element $\qquad C_T = \dfrac{\sigma a}{4}\left(\theta_t - 2\displaystyle\int_0^1 x\,\alpha(x)\,dx\right)$ $\qquad\qquad$ (59)

Vortex Core model $\qquad \delta = \left(\dfrac{5\sigma a}{7b}\right)\dfrac{\theta_t + \Lambda - \lambda}{\lambda}$ $\qquad\qquad$ (76)

59

Vortex Core Model $\qquad \delta_w = \left(\dfrac{5\sigma a}{7b}\right) \dfrac{\theta_t + \Lambda - \lambda}{\lambda_w \epsilon}$ $\qquad\qquad$ (77)

To simplify the equations, introduce the notation

$$R_1 \stackrel{\triangle}{=} 2\int_0^1 x\alpha(x)dx \;=\; R_1(\Lambda,\lambda,\delta) \qquad\qquad (78)$$

$$R_2 \stackrel{\triangle}{=} 2\int_0^1 x\alpha^2(x)dx \;=\; R_2(\Lambda,\lambda,\delta) \qquad\qquad (79)$$

$$W_1 \stackrel{\triangle}{=} 2\int_0^1 x\alpha_w(x)dx \;=\; W_1(\Lambda,\lambda_w,\delta_w) \qquad\qquad (80)$$

$$W_2 \stackrel{\triangle}{=} 2\int_0^1 x\alpha_w^{\,2}(x)dx = W_2(\Lambda,\lambda_w,\delta_w) \qquad\qquad (81)$$

$$W_3 \stackrel{\triangle}{=} 2\int_0^1 x\alpha_w^{\,3}(x)dx = W_3(\Lambda,\lambda_w,\delta_w) \qquad\qquad (82)$$

The equations become

$$\epsilon = \sqrt{\frac{R_1}{W_1}} \qquad\qquad (83)$$

$$C_T = \Lambda R_1 + \epsilon^2 W_2 \qquad\qquad (84)$$

$$\epsilon^2 W_3 = \frac{\sigma a}{2}(\theta_t R_1 - R_2) + \Lambda^2 R_1 \qquad\qquad (85)$$

$$C_T = \frac{\sigma a}{4}(\theta_t - R_1) \qquad\qquad (86)$$

$$\delta = \left(\frac{5\sigma a}{7b}\right)\frac{\theta_t + \Lambda - \lambda}{\lambda} \qquad\qquad (87)$$

60

$$\delta_w = \left(\frac{5\sigma a}{7b}\right) \ \frac{\theta_t + \Lambda - \lambda}{\lambda_w \epsilon} \qquad\qquad (88)$$

The problem we have to solve can now be stated as

Given- $\Lambda, \theta_t, \sigma, a, b;$ Find: $\epsilon, C_T, \lambda, \lambda_w, \delta, \delta_w$

61

IV.5.   TIP LOSS FACTOR

The analysis presented to this point has not included a blade tip loss factor. The purpose of the following presentation is to derive a method for including such a factor.

Eq. (53) expresses blade element thrust for a single blade as:

$$dT_b = \frac{\rho ac}{2} \Omega s \left[\Omega R \theta_t + V - v \right] ds$$

This can be written in a somewhat more general form as

$$dT_b = \frac{\rho ac}{2} (\Omega R)^2 x (\theta_t + \Lambda - \lambda) ds \qquad (89)$$

The blade loading is defined by

$$T_b' \triangleq \frac{dT_b}{ds} = \frac{\rho ac}{2} (\Omega R)^2 x (\theta_t + \Lambda - \lambda) \qquad (90)$$

Eq. (89) can be integrated to get the thrust produced by one blade.* For b constant-chord blades, the thrust is

$$T = 1/4 \; b\rho ac (\Omega R)^2 R (\theta_t + \Lambda - \lambda)$$

$$= a/4 \left(\frac{bc}{\pi R} \pi R^2 \rho (\Omega R)^2 (\theta_t + \Lambda - \lambda) \right) \qquad (91)$$

---

* The integration assumes uniform inflow, i.e., λ is not a function of x. This is equivalent to replacing the trapezoidal inflow distribution by the classical uniform distribution. We do this, at this point in the derivation to obtain the classical tip loss factor. Subsequently we return to the trapezoidal distribution to get an improved tip loss factor.

The thrust coefficient is therefore given by Eq. (86) as

$$C_T = \frac{\sigma a}{4} (\theta_t + \Lambda - \lambda)$$

C_T can be expressed in terms of the blade loading at the tip, by combining this equation and Eq. (90) and setting x = 1 in Eq. (90). The result is

$$C_T = \frac{\sigma a}{4} \left(\frac{2 T_b'|_{tip}}{\rho a c (\Omega R)^2} \right) \qquad (92)$$

In Reference 27, a tip loss factor for hovering rotors is presented in terms of C_T as follows:

$$B = 1 - \sqrt{\frac{2 C_T}{b}} \qquad (93)$$

The "tip losses" occur because air flows from the bottom region to the top region of the blades at the tips. The flow occurs because of lift (pressure gradient between the upper and lower blade surfaces). Such flow "destroys" the lift on the blade elements in the immediate region of the tips, because it interferes with the two-dimensional lifting mechanism of the airfoil section.

Since tip losses are caused by flows at the tips due to lift at the tips, it seems that the blade distributed loading at the tips really controls the quantitative value of B, not the overall rotor thrust coefficient as suggested by Eq. (93). However, Eq. (93) is valid at hover (assuming the important factor is distributed loading at the tip), since C_T is directly related to T' by Eq. (64). A more general form of (93) can be expressed in terms of T_b', and, as shown below, this leads to a simple expression for B valid both at hover and in descent.

$$B = 1 - \frac{1}{b} \sqrt{\frac{\sigma a \; T_b'|_{tip}}{\rho a c (\Omega R)^2}} \qquad (94)$$

Eq. (94) has been derived for rotor systems with uniform induced velocity. Because B is expressed in terms of $T_b'|_{tip}$, however, it seems reasonable that it should be applicable to rotors operating with nonuniform inflow, inasmuch as the tip loss is a local phenomenon depending primarily on blade tip operating conditions.

63

For the descending rotor, Eq. (57) is applicable.

$$dT_b = 1/2 \ \rho(\Omega s)ac\left[\Omega R\theta_t - v(x)\right]ds$$

$$T_b' = -\frac{\rho ac}{2} \ (\Omega R)^2 x(\theta_t - \alpha(x)) \tag{95}$$

At the tip, T_b' becomes[*]

$$T_b'\Big|_{tip} = \frac{\rho ac}{2} \ (\Omega R)^2(\theta_t + \Lambda) \tag{96}$$

Substituting Eq. (96) into Eq. (94) gives the major result of this section, a general formula for B.

$$B = 1 - \frac{1}{b} \ \sqrt{\frac{\sigma a}{2} \ (\theta_t + \Lambda)} \tag{97}$$

---

[*] Note that λ disappears from the T_b expression at the tip. This is because $\alpha(x) = -\Lambda$ at $x = 1$, i.e., at the tip. The disappearance of λ is a consequence of the assumption of a trapezoidal inflow distribution. It accounts for the difference between the tip loss factor derived here (Eq. 97) and the classical tip loss factor, Eq. 93. Because the trapezoidal inflow model gives a higher T_b' than the uniform inflow model, at a given C_T and Λ, the tip loss is larger, i.e., B is smaller.

IV.6.   INCORPORATION OF THE TIP LOSS FACTOR

      All the equations required to solve for C_T versus rate of descent of a given rotor have now been obtained. At this point, the problem is to include the effects of B on Eqs. (83) through (88). One way to do this is outlined below.

      Solve Eqs. (83) through (88) in a normal way, without considering tip losses. Results of such a solution process can be expressed in nondimensional form, using the actual rotor radius R as the characteristic length.

      To include tip losses, say that the effective rotor radius, R_e, is given by

$$R_e \overset{\Delta}{=} RB = R\left[1 - \frac{1}{b}\sqrt{\frac{\sigma a}{2}(\theta_t + \Lambda)}\right] \tag{98}$$

      The solutions to (83) through (88) can be considered valid for a rotor with radius R_e and no tip losses (the no tip loss assumption being already embodied in Eq. (83) through (88)). Thus, when the nondimensional data representing the solutions to Eqs. (83) through (88) are dimensionalized, an effective radius R_e must be used to account for tip losses.

      Obviously, it is desirable to present data nondimensionalized by a constant characteristic length (e.g., R) rather than a variable characteristic length (e.g., R_e). To accomplish this, the non-dimensional data expressed in terms of R_e must be restated in terms of R. As an example of this process, consider a graph of C_T vs Λ, predicted for a rotor of given geometry by solving Eqs. (83) through (88). For a given Λ, the actual thrust T is given by

$$T = \pi R_e^2 \rho(\Omega R_e)^2 C_T = \rho\pi\Omega^2 R_e^4 C_T \tag{99}$$

65

Define C_T^* as the desired thrust coefficient, i.e., the thrust non-dimensionalized with respect to R. Then

$$T \triangleq \rho \pi \Omega^2 R^4 C_T^*$$

(100)

Combining (99) and (100) to eliminate T

$$C_T^* = \left(\frac{R_e}{R}\right)^4 C_T$$

(101)

Eqs. (101) and (98) can be combined to yield

$$C_T^* = \left(1 - \frac{1}{b} \sqrt{\frac{\sigma a}{2} \left(\theta_t + \Lambda\right)}\right)^4 C_T$$

The characteristic length, R_e, has also been used to produce Λ:

$$\Lambda = \frac{V}{\Omega R_e}$$

(102)

This process is applicable to the value for Λ in the original non-dimensionalized data $C_T = C_T(\Lambda)$.

The question arises, does the nondimensionalizing process (102) apply to Eq. (98)? [If R_e is included in the Λ in Eq. (98), then Eq. (98) becomes an implicit expression in R_e.] It is expected that the difference in results as to whether the Λ in (98) is nondimensionalized by R or R_e will be extremely small. Assuming this for the time being, substitute Λ^* into (98) and (101),

$$\Lambda^* \triangleq \frac{V}{\Omega R}$$

(103)

66

However, the effect of B should be included in determining the Λ in the original data. Combining (102) and (103) to eliminate V,

$$\Lambda^* = \Lambda \left(\frac{R_e}{R}\right) = \left(1 - \frac{1}{b}\sqrt{\frac{\sigma a}{2}\left(\theta_t + \Lambda^*\right)}\right)\Lambda \qquad (104)$$

which can be rewritten as

$$\Lambda = \frac{\Lambda^*}{1 - \frac{1}{b}\sqrt{\frac{\sigma a}{2}}\left(\theta_t + \Lambda^*\right)} \qquad (105)$$

Summarizing, the major results of this section are the following equations :

$$B = 1 - \frac{1}{b}\sqrt{\frac{\sigma a}{2}\left(\theta_t + \Lambda^*\right)} \qquad (97)$$

$$\Lambda = \frac{\Lambda^*}{B} \qquad (103)$$

$$C_T^* = B^4 C_T \qquad (101)$$

An example hand calculation of C_T^* versus the rate-of-descent parameter is done below, to show the method. Note that to obtain the graph of C_T^* vs J^*, it is necessary to assume an initial value of J^*, and later to determine what value of J this implies. Thus the method doesn't predict C_T^* for a given single value of J, but instead predicts the entire C_T^* versus J^* graph.

67

The derivations given in this chapter employ standard notation used in helicopter analysis. A different notation is traditional in propeller analysis. For example, J is used to denote nondimensional axial propeller velocity. J is related to Λ by

$$J = \pi\Lambda$$

The propeller thrust coefficient is denoted here as C_{T_p} and is related to the "helicopter" thrust coefficient by

$$C_{T_p} = 64\,\pi^3\,C_T$$

In the comparison of our predicted C_T versus measured, given in the next section, C_T the "propeller" notation is used, because the experimental data are presented in this notation.

The results of the calculation are shown in Figure 22 and are compared with the C_T versus J graph that would be obtained assuming zero tip loss factor. The difference in magnitude of C_T and slope $\partial C_T/\partial J$ at a given C_T is considerable.

TABLE I. EXAMPLE CALCULATION OF $C_{T_p}^*$ VERSUS J^*

σ = .186   β = 1.0 $θ_t$ = .25   a = 5.73   b = 3

(1) J^*	(2) $Λ^*$	(3) $θ_t+Λ^*$	(4) $\frac{σa}{2}×(3)$	(5) $\sqrt{(4)}$	(5)/b	B	J	c_{T_p}	B^2	B^4	$c_{T_p}^*$
-.40	-.127	.1230	.0658	.256	.0858	.9142	-.437	.123	.838	.700	.086
-.30	-.0955	.1545	.0828	.289	.0965	.9035	-.332	.152	.818	.669	.102
-.20	-.06366	.1863	.0995	.315	.1050	.8950	-.223	.182	.800	.640	.116
-.10	-.03183	.2182	.1160	.341	.114	.886	-.113	.210	.785	.617	.129
0	0	.2500	.1330	.365	.122	.878	0	.236	.769	.590	.137
.05	.01592	.2659	.1420	.377	.126	.874	.0571	.249	.765	.585	.146
.10	.03183	.2818	.1500	.387	.129	.871	.1145	.260	.760	.579	.150
.15	.04775	.2978	.1590	.398	.133	.867	.1740	.271	.751	.565	.153
.20	.06366	.3137	.1662	.410	.137	.863	.2310	.280	.746	.557	.155
.25	.07958	.3296	.1750	.420	.140	.860	.2910	.287	.740	.548	.156

69
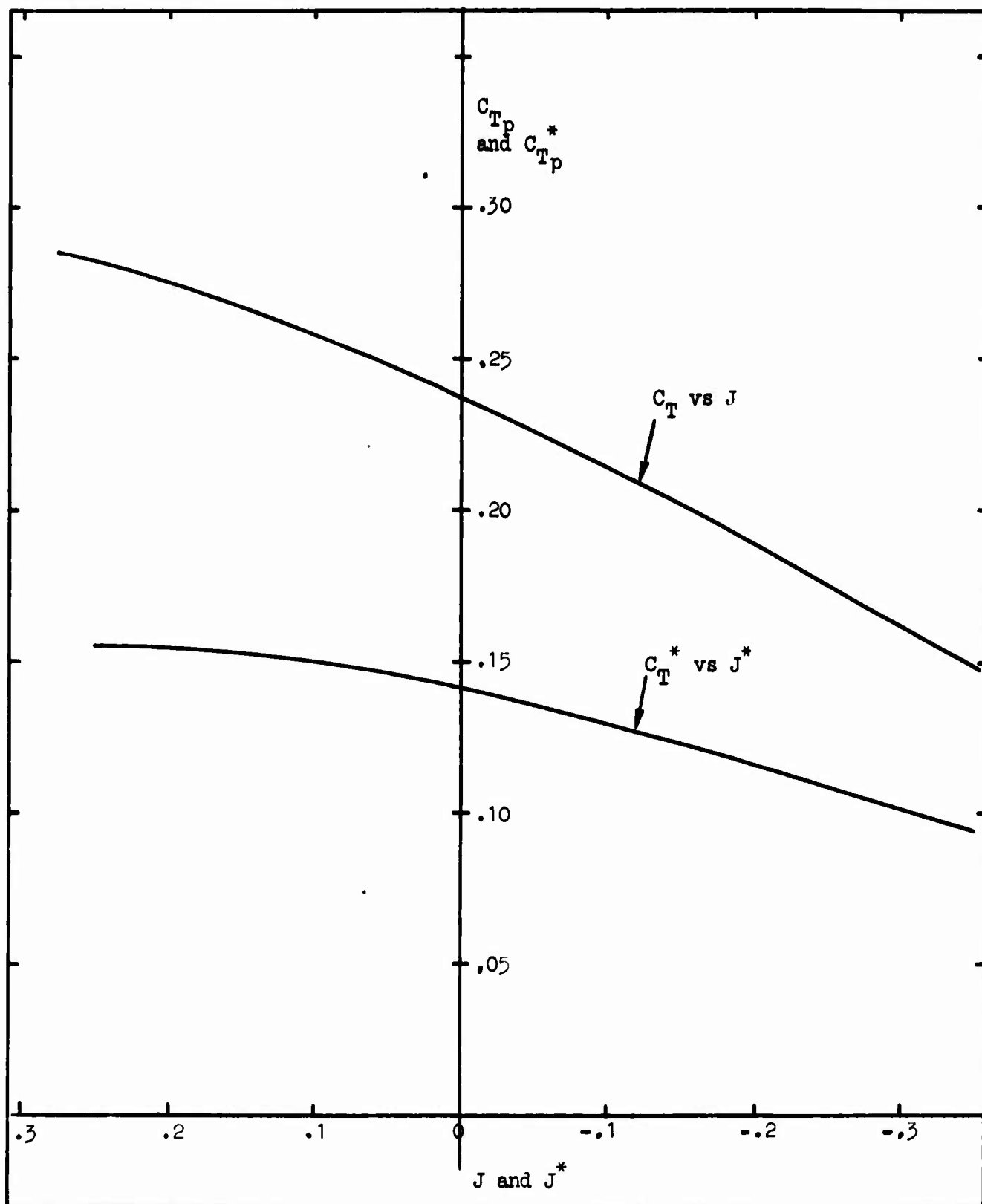
Figure 22. Results of Example Calculation of C_{T_p} Versus J.

Hardly any data on thrust of helicopter rotors in vertical descent has been published. Reference 19 describes flight tests on a Westland Whirlwind helicopter in vertical descent, but unfortunately the data obtained are not sufficiently complete to permit correlation with our theory. We therefore have to employ data on VTOL propellers. Reference 18 presents wind-tunnel data on VTOL propellers at shaft angles of attack representing vertical and inclined descents, and Reference 28 gives data on the same propellers in climb conditions (though not all the blade settings were duplicated). By combining these references the experimental data graphed on Figure 23 were obtained (solid lines). The dash-dot lines on Figure 23 show the results obtained by solving Eqs. (78)-(89) for the propeller and then modifying the results (as specified by Eqs. (97)-(101) to include the tip loss effects.

It will be seen that the theory agrees well with experiment for climb, hover, and rates of descent outside the unsteady region of the vortex-ring state.

Figures 24 through 27 are presented to show the comparison between experiment and theory for the following different theoretical approaches:

(1)   Vortex core wake model with variable tip loss factor (Eq. (97)).

(2)   Variable tip loss factor with no vortex cores (i.e., wake represented by uniform downwash over rotor disc of radius BR).

(3)   Conventional analytic model; i.e., constant tip loss factor (B = 1 in this case) and uniform downwash.

For all three of these cases, the solid lines represent the experimental data.

Figures 24 through 27 indicate a striking improvement in the accuracy of theoretical results when the descending rotor models described in this chapter are applied.

Another important conclusion that can be reached, by inspection of the figures, is that correlation between experiment and theory is good if the tip losses are accounted for while retaining the uniform inflow model. This does not mean that the vortex cores are unimportant, since this core model was an essential part of the derivation leading to the tip loss factor (Eq. (97)). However, once the existence of
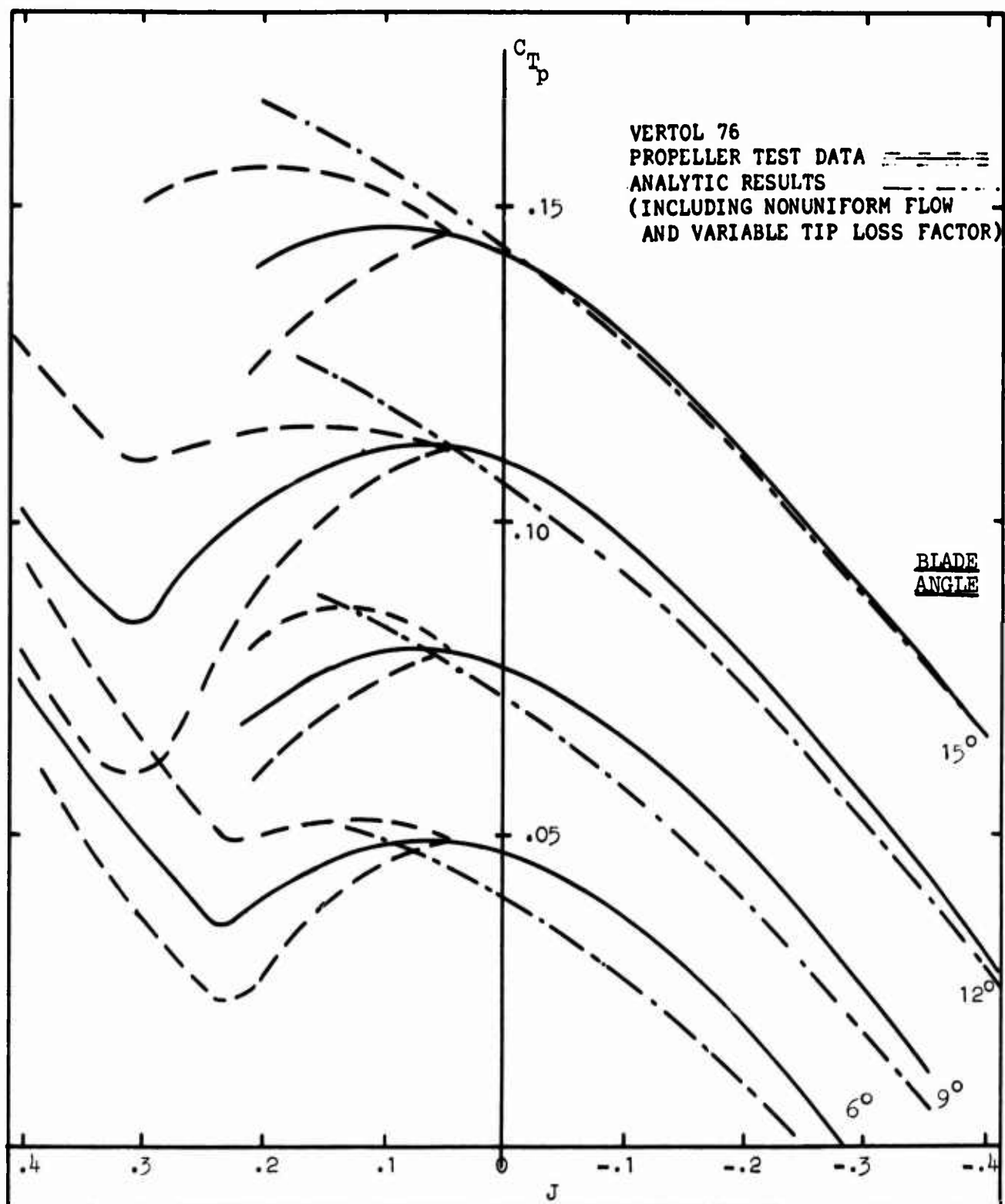
Figure 23. Comparison of Analytic and Experimental Results for
Thrust vs Descent Rate of a VTOL Propeller.

72
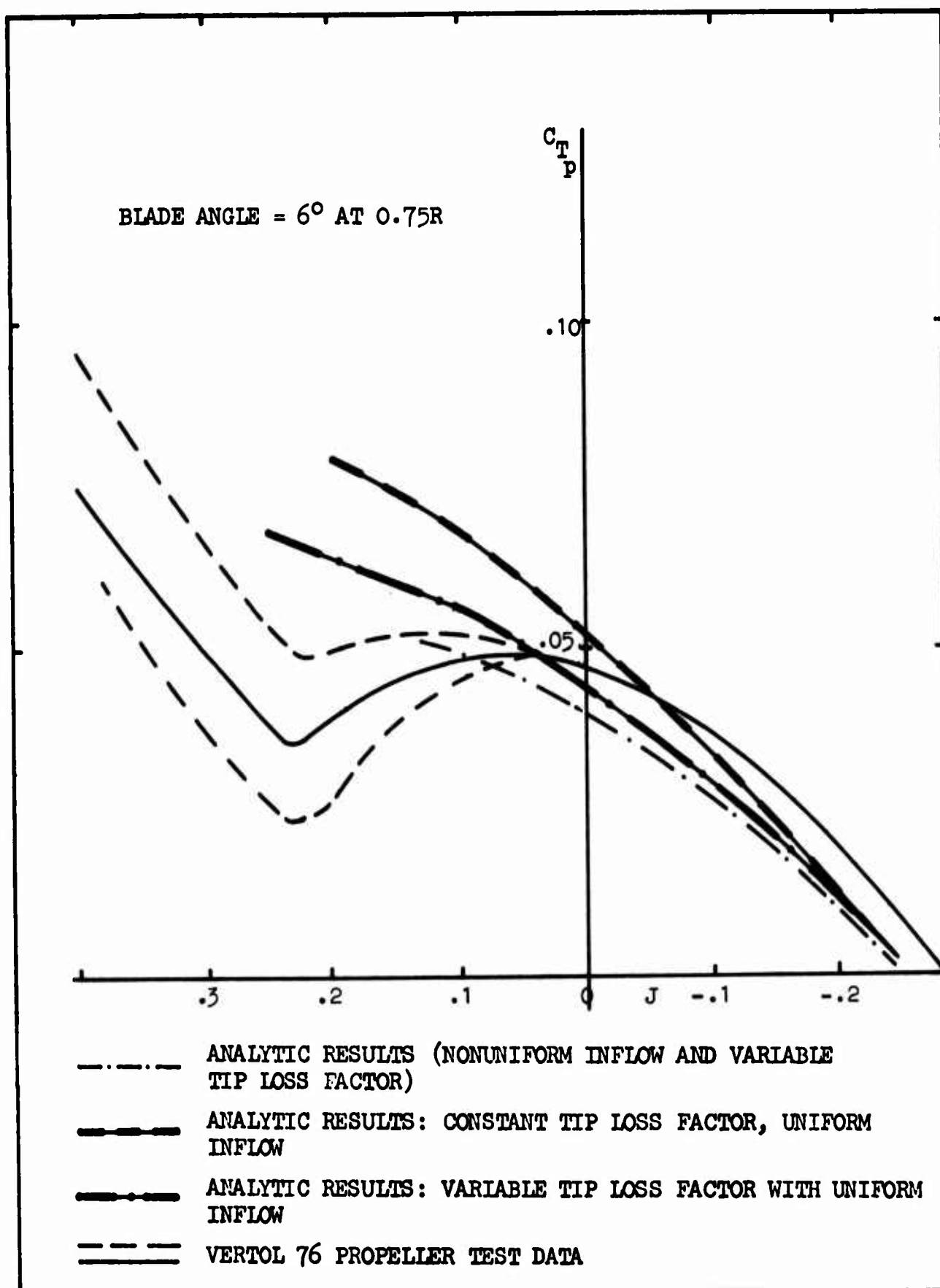
Figure 24. C_{T_p} vs J for 6-Degree Blade Angle.
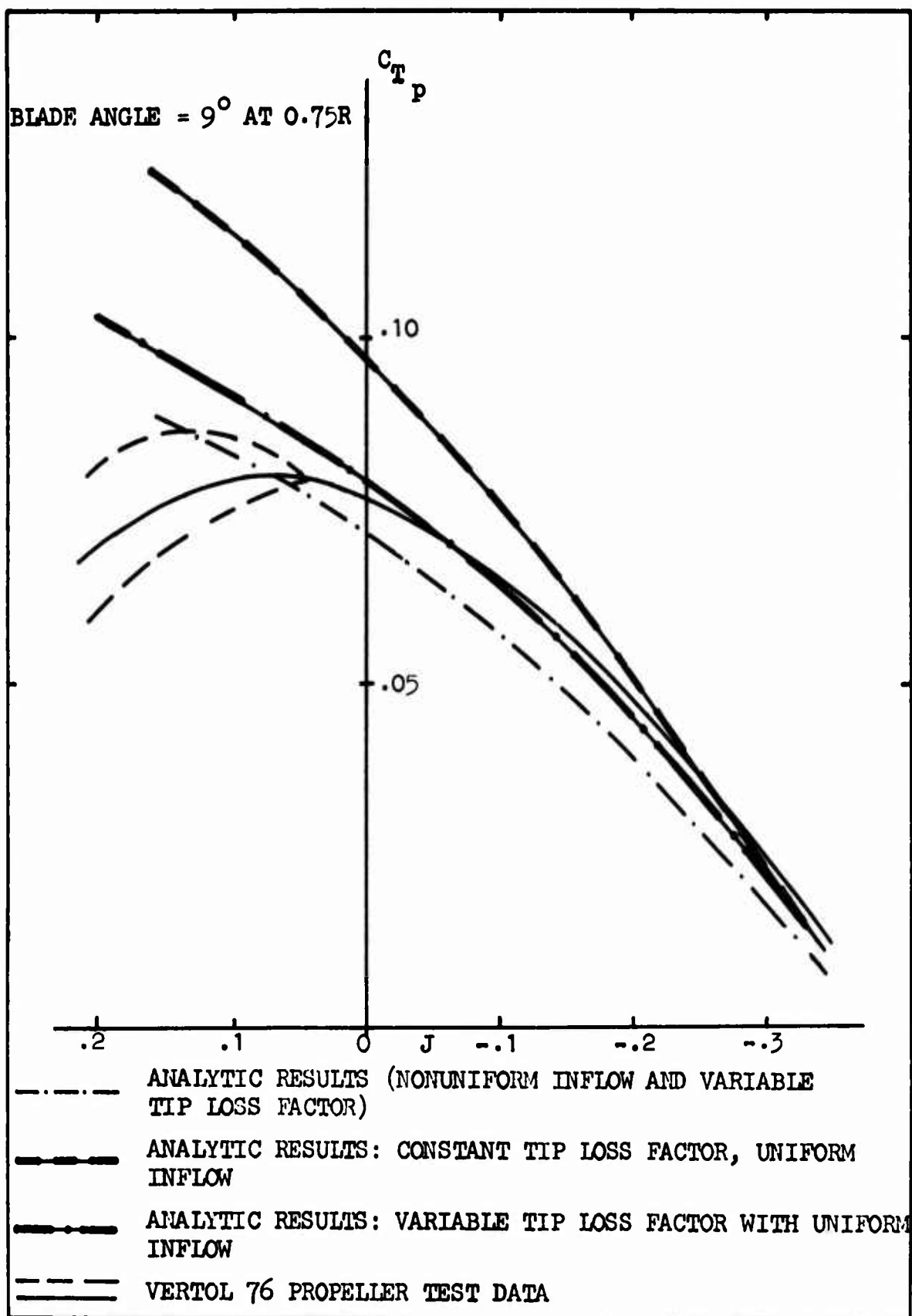
Figure 25. C_{T_p} vs J for 9-Degree Blade Angle.
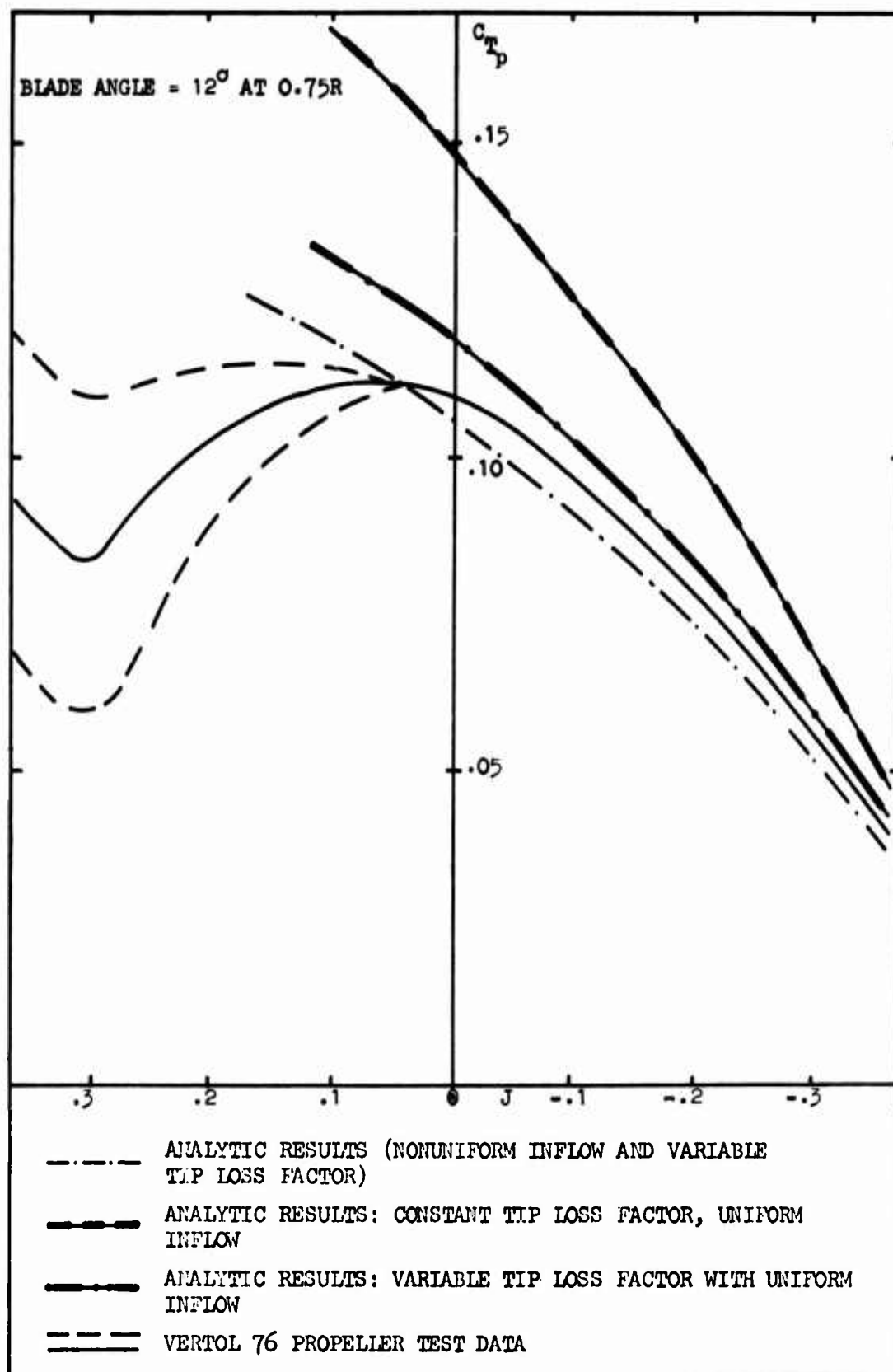
Figure 26. C_{T_p} vs J for 12-Degree Blade Angle.

75

FIGURE 8
BLADE ANGLE = 15° AT 0.75R

ANALYTIC RESULTS (NONUNIFORM INFLOW AND VARIABLE
TIP LOSS FACTOR)

ANALYTIC RESULTS: CONSTANT TIP LOSS FACTOR, UNIFORM
INFLOW

ANALYTIC RESULTS: VARIABLE TIP LOSS FACTOR WITH UNIFORM
INFLOW

VERTOL 76 PROPELLER TEST DATA
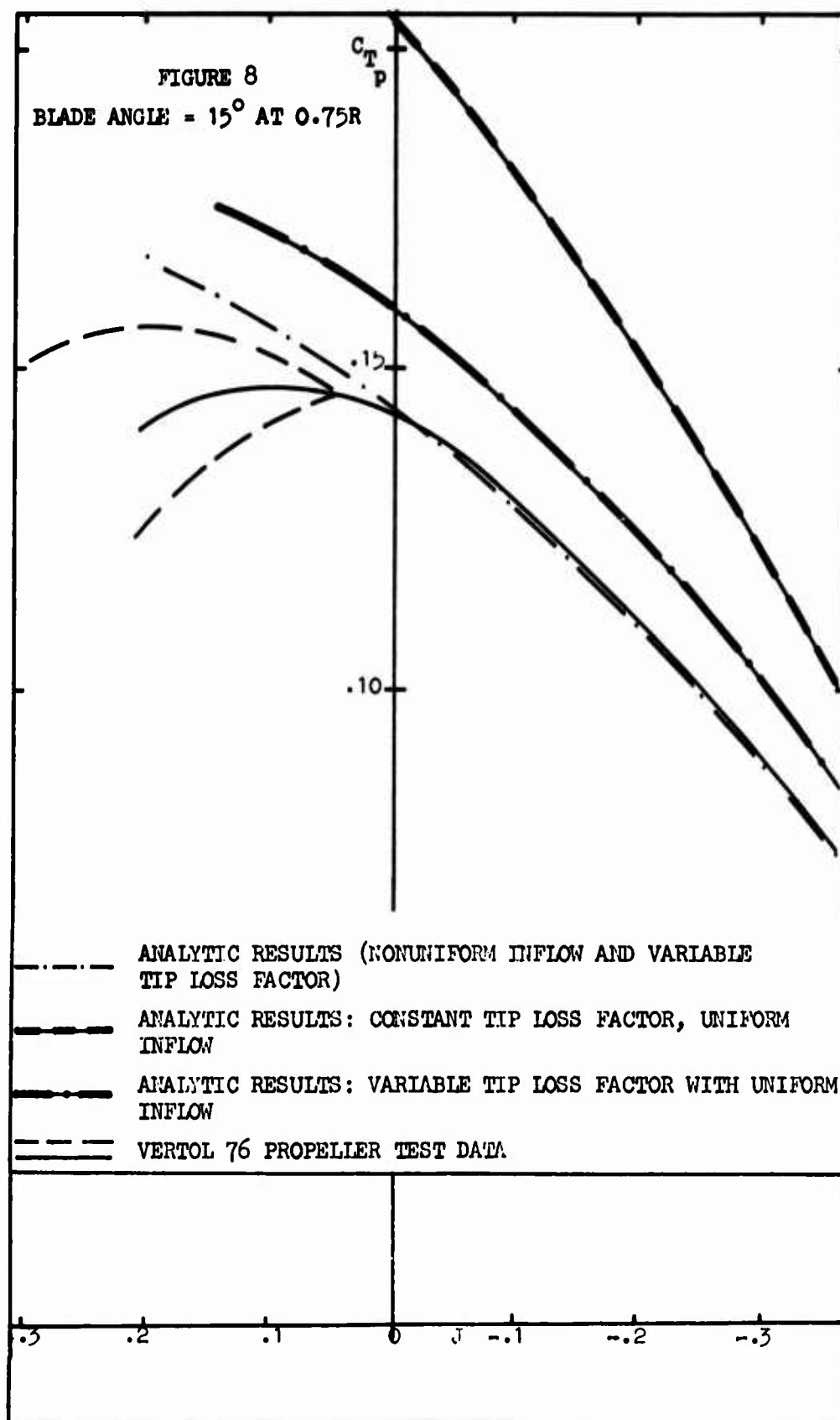
Figure 27. C_{T_p} vs J for 15-Degree Blade Angle.

the viscous "boundary layer" between the slipstream tube and the surrounding air mass is recognized, the simple tip loss factor can be derived. This situation is quite analogous to Prandtl's fixed-wing boundary layer model. The presence of the viscous region must be acknowleged to assess correctly the physical flow mechanisms which produce the wing loads. The results for lift and induced drag derived from inviscid theory (which does not include the boundary layer), however, are still accurate if the boundary layer has not separated, causing stall. For the descending rotor, the viscous region is analogous to the boundary layer. The nonuniform downwash indirectly causes a thrust loss by inducing higher blade loadings near the tips. This thrust loss greatly exceeds that due to the momentum loss associated with the nonuniform downwash.

IV.8.   Summary

The performance of a vertically descending rotor can be calculated using a "vortex-core" wake system and a suitable blade tip loss factor. The results obtained by analyzing this flow model show good correlation with available experimental data over the region from fast climb to descent rates outside the vortex-ring buffet boundaries. Although the vortex core model is required to derive the descending tip loss factor, the wake inflow distributions can be assumed uniform (retaining the tip loss factor only and assuming negligible vortex core radius) without seriously degrading the accuracy of numerical results.

The application of the tip loss factor to derivative calculations is discussed in Volume II. The necessity to consider inclined as well as vertical descent requires a cyclicly varying B. Experimental data are not sufficiently complete to check the accuracy of derivatives calculated using this approach; however, it follows logically from the assumption that conditions at the tip determine the tip losses.

CHAPTER V. THE MOSTAB MODULAR STABILITY DERIVATIVE PROGRAM AND ITS APPLICATION TO THE S-58 AND AH-56A HELICOPTERS

V.1. INTRODUCTION

This chapter describes how stability derivatives were calculated for the S-58 and AH-56A. (As explained below, published derivatives were used, for the YHC-1A.) The chapter is organized as follows:

Firstly, the MOSTAB modular stability derivative program is described. MOSTAB was specially evolved for this study; it calculates derivatives for any type of helicopter, with a wide variety of possible flow models. The description in this chapter is very general; full details of the equations used in MOSTAB and a listing are given in Volume II.

Secondly, the forms of the input data required for MOSTAB are summarized, and the specific data for the S-58 and AH-56A are presented. These data include three-view drawings, estimated aerodynamic coefficients for fuselages, rotors, etc., and the appropriate reference areas.

Thirdly, the flight conditions for which derivatives were calculated are tabulated. (The actual derivatives for each flight condition are listed in Volumes III and IV, with the transfer functions.)

Finally, the chapter concludes with a brief discussion of the accuracy of the MOSTAB derivatives.

V.2. THE NEED FOR MOSTAB

During the course of the study described here, it became apparent that it was difficult to obtain reliable stability derivatives for single-rotor, tandem-rotor, and compound helicopters in descending flight. In some cases derivatives were available for level flight, but the programs used to calculate these derivatives contained "built in" assumptions regarding flow models which were inappropriate for descending flight. It was not feasible to modify these programs to incorporate alternative flow models, such as those described in Chapter IV. Furthermore, only limited experimental data on derivatives in descending flight were available.

78

Accordingly, it was decided to start afresh, by writing a "universal" program to compute trim and stability derivatives for any type of helicopter, with little or no restriction as to the flow models that had to be used. Further requirements were that the stability derivatives should be printed-out in all axis systems of interest, in dimensional form and also divided by the appropriate inertias, and that the contribution of each component to the complete derivative should be printed-out so that the reasons for unexpected values of derivatives could be traced. The result of these requirements is the MOSTAB program described below.

The following description of MOSTAB is the bare minimum required to follow the subsequent discussion. For more details of MOSTAB, see Volume II.

V.3. PRINCIPAL FEATURES OF MOSTAB

MOSTAB currently calculates performance, trim, and stability derivatives for any type of subsonic aircraft. The program can be extended for use in hybrid simulation and may also be used to calculate limiting conditions such as 'g' boundaries. The unique feature of MOSTAB which gives such versatility is its modular construction, explained below.

Figure 28 shows a helicopter separated into elements. The physical characteristics of each element are specified in the input data. Separate sections of MOSTAB handle each element type. The influence of each element on the aircraft is summed to calculate dynamic characteristics of the assembled flight vehicle.

When an element (e.g., wing, propeller) produces a force (lift, drag, thrust), the air in the vicinity of the aircraft is set in motion. The induced velocities (sometimes called downwash and sidewash) affect other elements by changing their local airspeed and angle of attack. Interference velocities are thus very important and must be calculated accurately.

MOSTAB includes all of these "aerodynamic coupling" (interference velocity) effects in a single subroutine. Any desired model for interference velocities can be included in this subroutine, which performs all of the necessary interference velocity calculations. No fundamental program changes are required to modify interference velocity models as required to suit particular vehicles; only the interference subroutine need be changed.

79
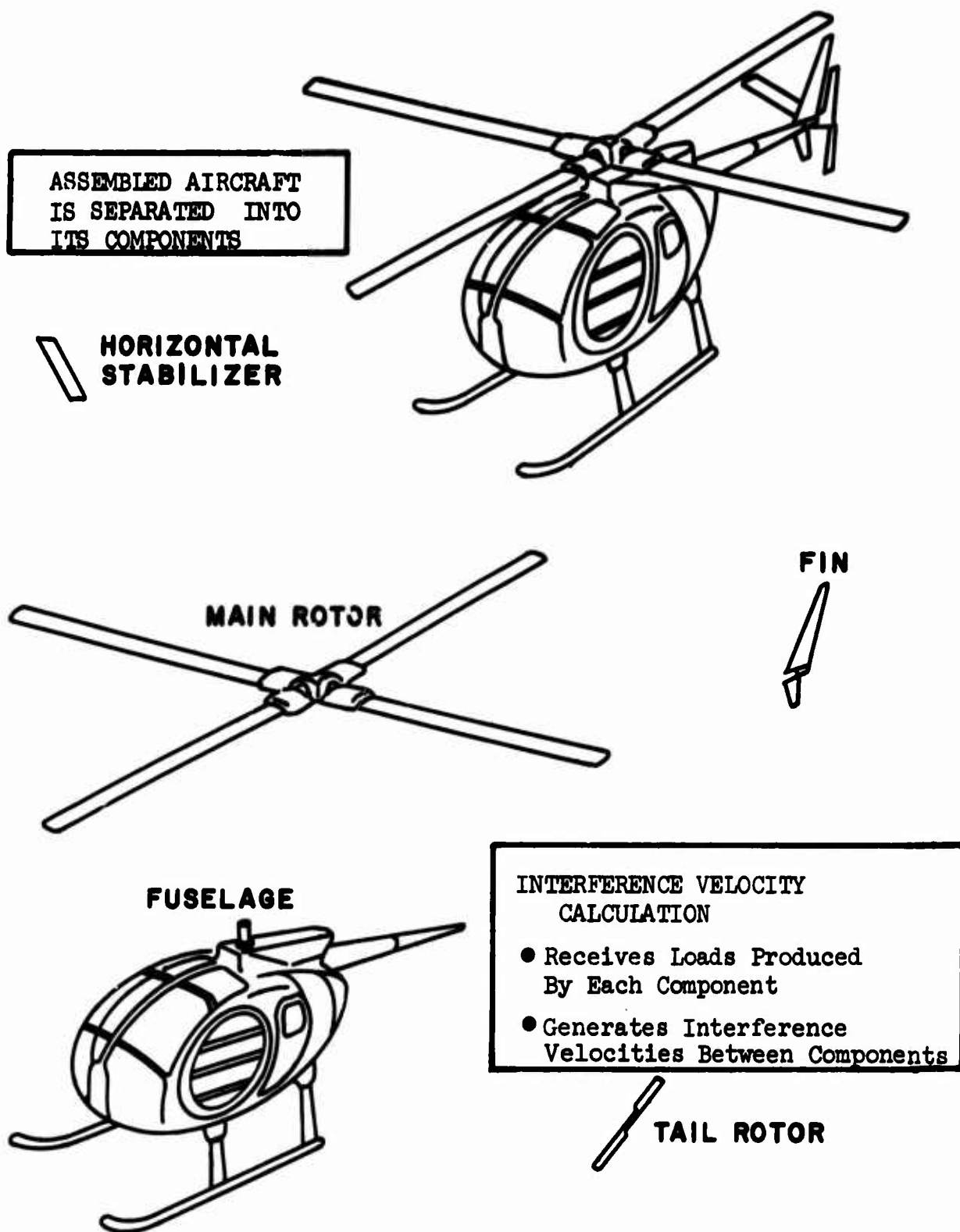
Figure 28. Modular Representation Used by MOSTAB.

Either rigid rotors (propellers) or flexible bladed rotors
(helicopter rotors - hinged or hingeless) can be studied by MOSTAB.
The modular nature of the program allows one to represent an air-
craft with as many rotors, aerodynamic bodies (fuselages, nacelles,
etc.), and lifting surfaces (wings, empennage surfaces, canard
surfaces, etc.) as desired.

Because aerodynamic rotors are the most complicated element
types, a brief description of the rotor analyses incorporated in
MOSTAB is presented here. "Rotors" are either of the flexible
bladed type (e.g., helicopter rotors with hinged blades, or the so-
called "rigid" rotors, whose blades deflect structurally to a
substantial degree) or of the truly rigid type (propellers). The
same subroutines compute flexible and rigid rotor characteristics
in MOSTAB. Since the rigid rotor (propeller) blades do not deflect,
they provide no particular analytic difficulty. MOSTAB numerically
integrates computed inertial and aerodynamic loads radially and
azimuthally to determine the characteristics of rigid rotors (propellers).
The blade motion of flexible rotors must be determined before loads
from such rotors can be determined. The "normal mode" method is
used in MOSTAB to represent the flexible blades. The normal mode shape
and frequency for the first flapping mode of the flexible blade are
inputted to MOSTAB. (Other modes can be added easily to MOSTAB if
required, but the first mode adequately represents flexible bladed
rotors when determining stability derivatives.) Generalized mass
and force are generated in the program, and the flapping motion of
the blades is then computed numerically. Blade motion histories
for all flexible blade rotors are printed out for the trim flight
condition.

Other Versions of MOSTAB

As the MOSTAB program undergoes more development, various
versions will appear, each useful for analyzing aircraft under
certain conditions. The first version, MOSTAB-A, is considered
obsolete and unusable. This report describes the MOSTAB-B version,
which will always have applicability if its basic assumptions and
aerodynamic models are appropriate for the vehicle and flight
regimes being studied. More advanced versions (-C, -D, etc.) will
subsequently appear, each with more refined aerodynamic models, or
with special effects added for specific vehicle studies (e.g.,
tilt-wing, ducted-fan, etc., configurations).

As of June 1970, MOSTAB-C had been completed, together with a user's manual. The principal improvements of MOSTAB-C over MOSTAB-B are:

(1) Airfoil data can be automatically corrected for compressibility effects by means of a subroutine which reads local Mach number. The subroutine applies to both stalled and unstalled flow regimes. This compressibility correction is important at moderate and high speeds. MOSTAB was originally developed for approach conditions; hence, compressibility is not explicitly included in MOSTAB-B although an overall correction can be made by modifying the two-dimensional lift-curve slope in the wing and rotor input data.

(2) MOSTAB-C has an option to print out forces and moments acting on each element due to overall vehicle velocity and the induced velocity of the element itself, but excluding induced velocities due to other elements. This is important for correlating " isolated rotor" tests and calculations with data determined for complete aircraft.

(3) Rotor integration subroutines have been refined by removing a number of small-angle assumptions.

(4) Derivatives can be called in "stability axes" for any flight condition including hover (this is done by extending the definition of stability axes to include hover).

(5) A number of improvements and extensions to the data input and print-out formats have been made.

V.4   MOSTAB INTERFERENCE VELOCITY SUBROUTINE

The interference velocities between the various modules are calculated by an extension of the classical Glauert expression which applies to fixed wings as well as rotors. The Glauert expression is

$$v = \frac{k \cdot T}{2\rho A \left| V_T \right|} \tag{102}$$

where T = Resultant aerodynamic force on the module (e.g., wing
         or rotor)

       v = The induced velocity at a specified location (e.g., down-
         wash at the rotor).

       ρ = Air density

       A = " Characteristic Area" ($= \pi R^2$ for a rotor of radius R,
         $= \frac{\pi}{4} b^2$ for an elliptic wing of span b)

       V_T = Resultant velocity at the module

       k = A factor which relates the downwash at the desired
         location to the downwash at the module. Thus at some
         distance away from a rotor, when the slipstream has
         fully contracted, k = 2, whereas in the plane of the
         rotor k = 1.

MOSTAB extends the above Glauert expression to a multidimensional
form so that all linear and angular components of the " wash" can be
related to the forces and moments acting on the module. Thus such effects
as swirl due to rotor torque, and nonuniform downwash can be included.
The generalized form of Eq. (102) consists of two matrix equations:

$$\{v_i\} = \frac{1}{2\rho \left|V_{T_i}\right|} \left[A_i\right] \{f_i\} \qquad (103)$$

$$\{v_j\} = \left[K\right]\{v_i\} \qquad (104)$$

where v_i = A 6-component vector, the elements of which are
         the linear and angular induced flow velocities at
         module i

       $\left|V_{T_i}\right|$ = Absolute magnitude of the airspeed at module i

       $\left[A_i\right]$ = A 6 x 6 matrix which is input to MOSTAB. Its
         elements have units of (1/area) and represent
         the reciprocals of the characteristic areas of
         module i.

83

$\left\{ f_i \right\}$ = A 6-component vector, the elements of which are the X, Y, Z forces and L, M, N moments acting on module i.

$\left\{ \nu_j \right\}$ = A 6-component vector, the elements of which are the linear and angular induced velocities at the location of module j induced by the forces and moments acting on module i (e.g., i could be the main rotor and j the horizontal tail)

$\left[K \right]$ = A 6 x 6 matrix of interference velocity coupling constants

In the complete MOSTAB program, the order of vectors is increased from 6 to 6N where N is the number of modules (e.g., N = 5 for a helicopter with a fuselage, a main rotor, a tail rotor, a horizontal tail, and a vertical tail). Thus a wide variety of interference effects can be modeled with ease.

V.5.   MOSTAB INPUT DATA

The numerical values of the derivatives calculated by MOSTAB for the S-58 and AH-56A are given in Volumes III and IV. To supplement these derivatives, this section presents data which permits the basic assumptions underlying the derivatives to be checked. That is, relevant dimensions and aerodynamic coefficients for each "module" (wing, fuselage, etc.) are tabulated, together with the assumptions regarding interference velocities between the modules. Because of the low speeds of interest to the present study, compressibility corrections are not included. Hence, the aerodynamic coefficients for each module are the same for all flight conditions.

To understand the input data, it is first necessary to review the axis systems used in MOSTAB.

Figure 29 presents a three-view drawing of the Hughes OH-6A helicopter with various coordinate systems attached. These axes will now be discussed under individual headings.

(1)   Overall vehicle reference axes - Axes x, y, z of Figure 29 are the "overall vehicle reference axes" or "overall vehicle axes". These coordinates are defined in the main text and are the most basic axes used in MOSTAB. The positions of all vehicle elements are specified in the basic MOSTAB input data deck in vehicle coordinates, and the first set of stability and control derivatives is output in vehicle axes.
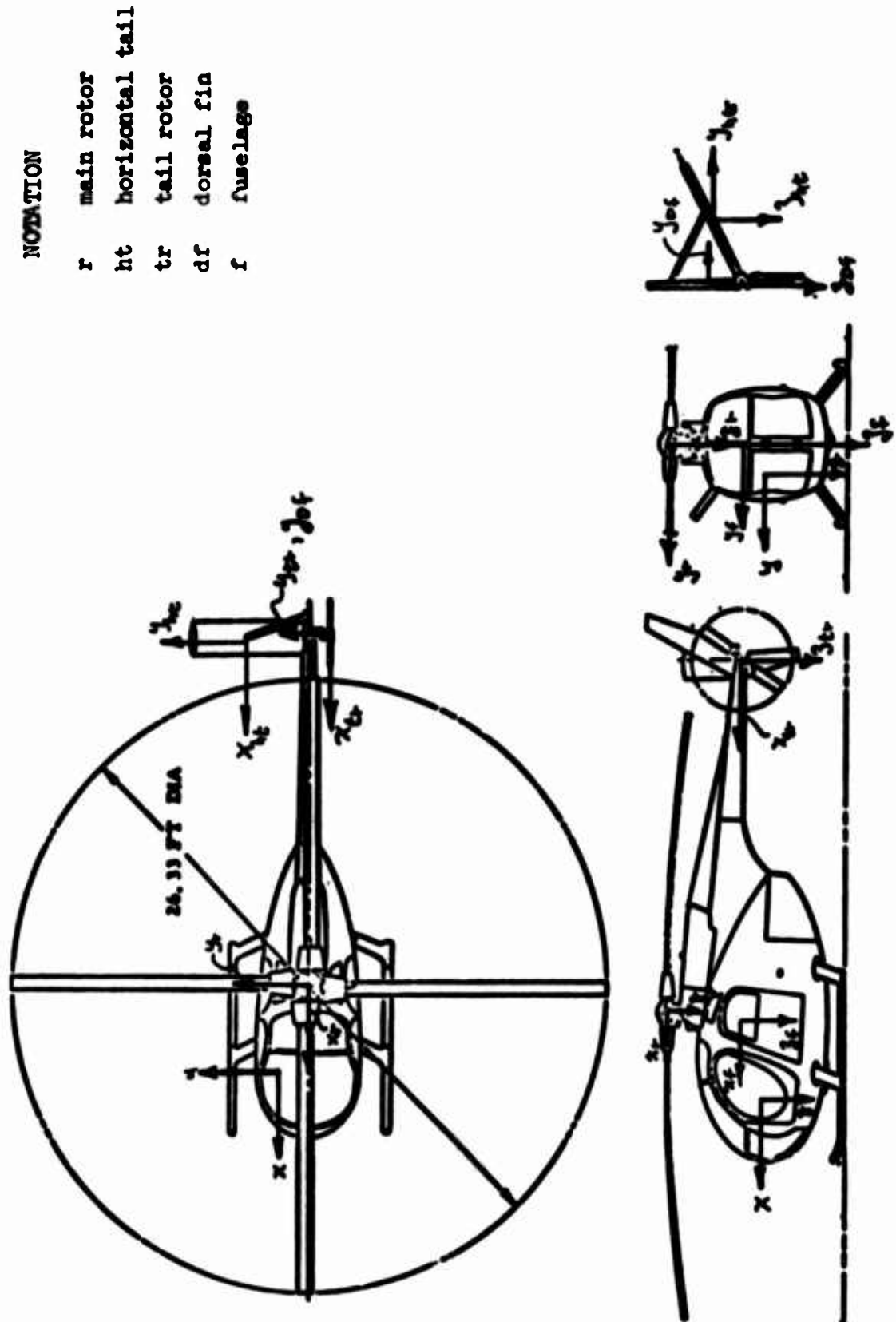
NOTATION

r   main rotor

ht   horizontal tail

tr   tail rotor

df   dorsal fin

f   fuselage

Figure 29. Standard OH-6A Three-View Drawing Including Example Overall Vehicle Reference Axes and Individual Aircraft Element Basic Axes.

85

(2) <u>Individual element axes</u> - basic element axes - All
coordinate systems shown by Figure 29, with the
exception of the overall vehicle axes, are " individual
element axes" or "individual element basic axes"
These axes all lie parallel to overall vehicle reference
axes, but with origins located at the " reference points"
of their respective aircraft components, as shown in the
figure. The F_{VA}, F_{VI} and F_C matrices printed as part of
MOSTAB output, and the columns DW, WE, WO, VIO, VAO and FO
printed as the trim-iteration solution all refer to these
basic element axes, as discussed in detail in Volume II.

(3) <u>Individual element local axes</u> - These coordinate systems
are not shown on Figure 29, but they are defined in
detail in Volume II. The "individual element local
axes" have their origins at the respective element
reference points (as do the individual element basic axes
discussed in (b) above), but they are rotated from the
basic axes to lie in a convenient position for analysis
of the particular aircraft component. For example, the
main rotor local axes are rotated from the basic axes
(coordinates x_r, y_r, z_r in Figure 29) so that their z
axis lies along the rotor shaft centerline. Also from
Figure 29, one sees that the tail rotor basic axes must
be rotated approximately 90 degrees about the x_{tr} axis
to become the tail rotor local axes (with the z axis
along the tail rotor shaft).

(4) <u>Stability axes</u> - These coordinates are translated and
rotated from " overall vehicle axes" so that their
origin lies at the aircraft's center of gravity and
so that the v and w airspeed components in stability
axes, at trim, vanish. This is the classical definition
of stability axes. In MOSTAB, stability axes are defined
with their z axis in the xz plane of the overall vehicle
axes. For hover, stability axes are arbitrarily defined
such that the x and y axes are horizontal with the
stability x axis parallel to the projection of the over-
all vehicle x axis on the horizontal plane.

V.6.   NUMERICAL DATA FOR S-58, AH-56A, and YHC-1A

Figures 30, 31, and 32 show 3-view drawings of the S-58,
AH-56A and YHC-1A. The input data for the S-58 and AH-56A are
summarized in Table II. All symbols are defined in Volume II.

86
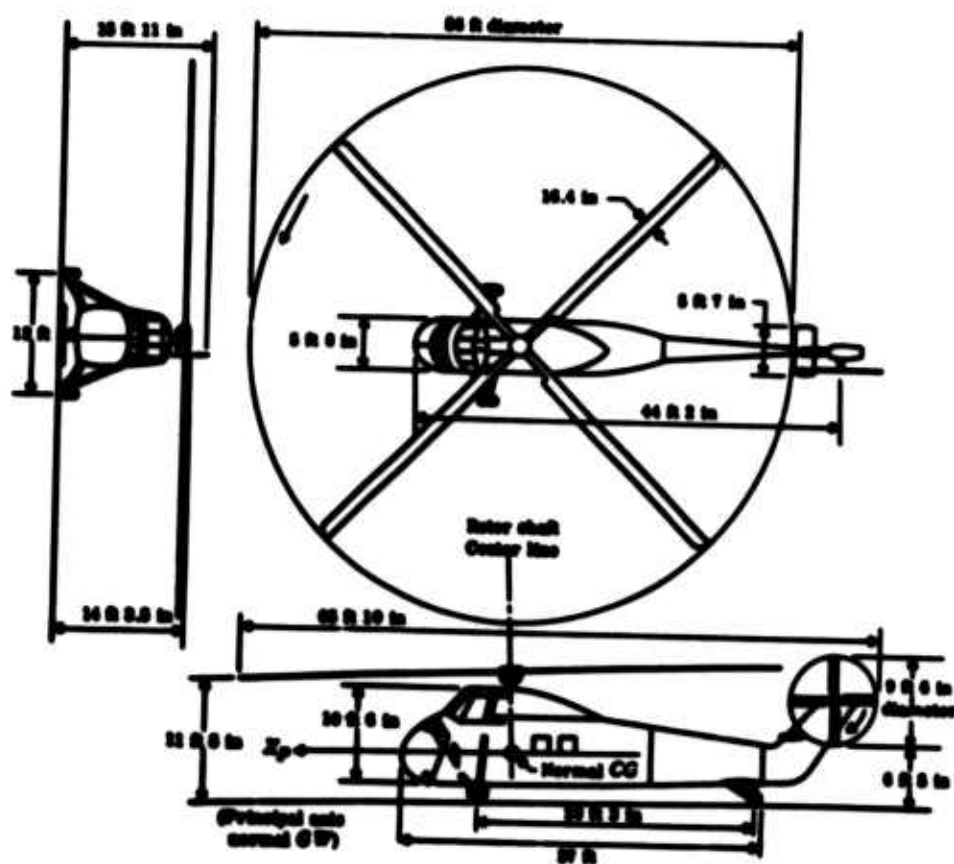
Figure 30. Three-View Drawing of Sikorsky S-58.
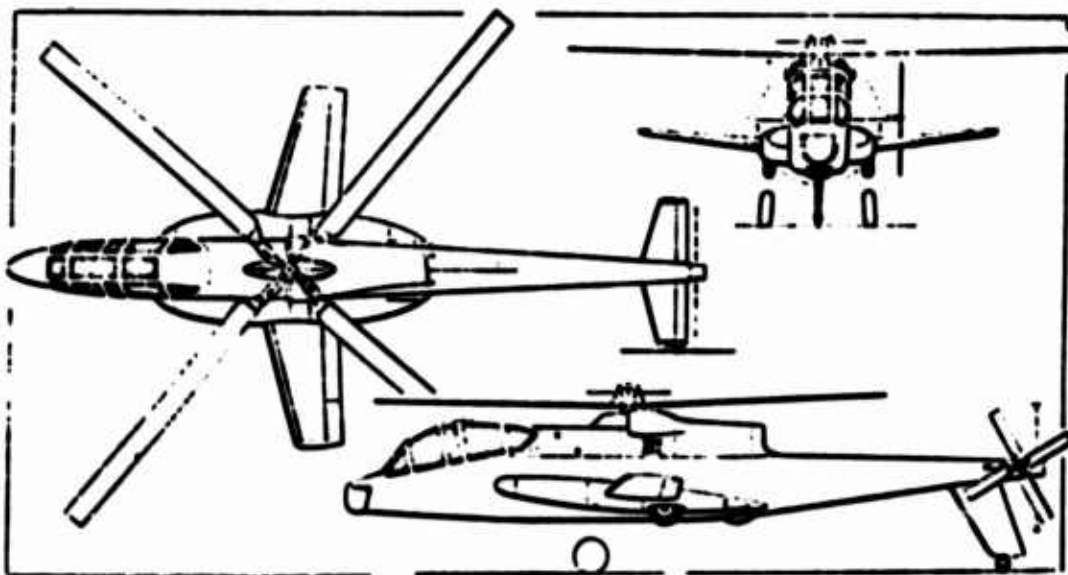
Figure 31. Three-View Drawing of Lockheed AH-56A.

Figure 32. Three-View Drawing of Boeing-Vertol YHC-1A.
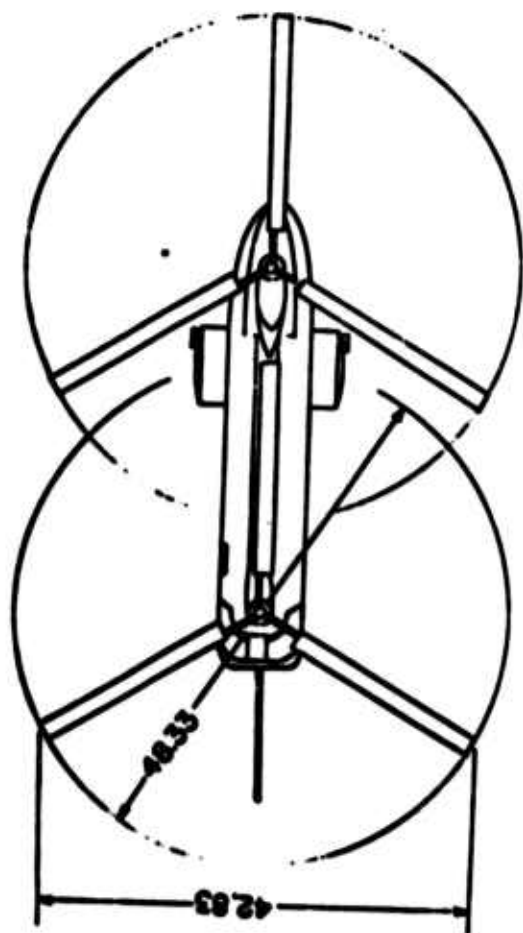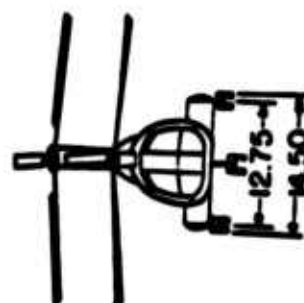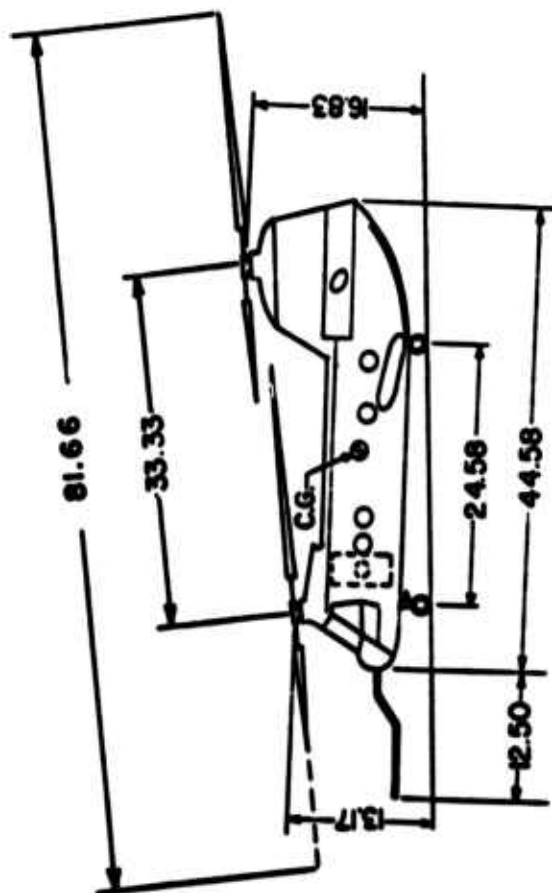
All dimensions are in feet.

Scale, ft
0 5 10

TABLE II - MOSTAB INPUT DATA
AIRCRAFT LOADING CONFIGURATION AND INERTIA (POUND,FOOT,SLUG)

MOSTAB SYMBOL	DEFINITION	SIKORSKY S-58	LOCKHEED AH-56A
GROSS WEIGHT		.1560+05	.1187+05
XCG		.3300-00	.0000
YGG	CENTER OF GRAVITY RELATIVE TO OVERALL VEHICLE COORDINATES	.0000	.0000
ZCG		.8750	.0000
IXX		.1150+05	.5895+04
IXY		.0000	.0000
IXZ	MOMENTS OF INERTIA WITH	.0000	.0000
IYX	RESPECT TO THE CENTER	.0000	.0000
IYY	OF GRAVITY WITH THE ≠X≠	.5000+05	.2750+05
IYZ	AXIS ALIGNED WITH O.V.C.	.0000	.0000
IZX	(O.V.C. = OVERALL VEHICLE	.0000	.0000
IZY	COORDINATES)	.0000	.0000
IZZ		.5500+05	.2309+05

CHARACTERISTIC AREA MATRIX ELEMENTS A(1,1)=A(2,2)=A(3,3)

ALL OTHER ELEMENTS ARE ZERO.

	SIKORSKY S-58	LOCKHEED AH-56A
FUSELAGE	.2770-01	.1350-01
HORIZONTAL TAIL	.4140-01	.1080-01
VERTICAL TAIL	.3000-01	.2500-01
MAIN ROTOR	.4100-03	.4800-03
TAIL ROTOR	.1400-01	.1270-01
WING		.1750-02
PROPELLER		.1270-01

TABLE II - MOSTAB INPUT DATA (CONTINUED)
FUSELAGE CHARACTERISTICS   (RADIAN,FOOT,SECOND)

MOSTAB SYMBOL	DEFINITION	SIKORSKY S-58	LOCKHEED AH-56A
PSI B		.0000	.0000
THETA B	ANGULAR DISPLACEMENTS RELATIVE TO OVERALL VEHICLE COORDINATES	.0000	.0000
PHI B		.0000	.0000
X		.0000	.0000
Y	LINEAR DISPLACEMENT RELATIVE TO OVERALL VEHICLE COORDINATES	.0000	.0000
Z		.0000	.0000
AB	REFERENCE AREA	.5400+02	.1500+03
C0	DRAG COEFF. ALPHA=0.	.4600+00	.1000-00
C1	DRAG COEFF/ALPHA	.0000	.3000-03
C2	DRAG COEFF/ALPHAXALPHA	.0000	.6000-03
CY0	SIDEFORCE COEFF.BETA=0.	.0000	.0000
CY1	-SIDEFORCE COEFF/BETA	.1400+01	.1000+01
CZ0	-Z-FORCE COEFF.ALPHA=0.	.0000	.2800-01
CZ1	-Z-FORCE COEFF/ALPHA	.7000-00	.4000-00
LB	REFERENCE LENGTH	.4400+02	.5260+02
CM0	PITCH COEFF.ALPHA=0.	.0000	.2000-02
CM1	PITCH COEFF/ALPHA	.3400-00	.2500-00
CN0	YAW COEFF ALPHA=0.	.0000	.0000
CN1	YAW COEFF/BETA	-.6600-00	-.6000-00

TABLE II - MOSTAB INPUT DATA (CONTINUED)
HORIZONTAL TAIL CHARACTERISTICS   (RADIAN,FOOT,SECOND)

MOSTAB SYMBOL	DEFINITION	SIKORSKY S-58	LOCKHEED AH-56A
PSI L		.0000	.0000
THETA L	ANGULAR DISPLACEMENTS RELATIVE TO OVERALL VEHICLE COORDINATES	.0000	.5240-01
PHI L		.0000	.0000
X		-.2830+02	-.2770+02
Y	LINEAR DISPLACEMENT RELATIVE TO OVERALL VEHICLE COORDINATES	.0000	.0000
Z		-.2000+01	.0000
AW	SECTION LIFT CURVE SLOPE	.6000+01	.6000+01
SW	REFERENCE AREA	.1238+02	.3450+02
CHORD	REFERENCE CHORD	.2220+01	.3180+01
CD0	SECTION CD AT ALPHA=0.	.0000	.0000
CD1	SECTION CD/ALPHA	.0000	.0000
CD2	SECTION CD/ALPHAXALPHA	.0000	.0000
AWCLD	ALPHA AT CD-MINIMUM	.0000	.0000
CAP GAMMA	DIHEDRAL ANGLE	.0000	.0000
BW	REFERENCE SPAN	.5550+01	.1083+02
LAMDA W	TAPER RATIO	.0000	.5700-00
CM0	CM AT ALPHA=0.	.0000	.0000
CMA	CM/ALPHA	.0000	.0000

TABLE II - MOSTAB INPUT DATA (CONTINUED)
VERTICAL TAIL CHARACTERISTICS   (RADIAN,FOOT,SECOND)

MOSTAB SYMBOL	DEFINITION	SIKORSKY S-58	LOCKHEED AH-56A
PSI L		.0000	.0000
THETA L	ANGULAR DISPLACEMENTS RELATIVE TO OVERALL VEHICLE COORDINATES	.6600	.0000
PHI L		.1570+01	.1570+01
X		-.3100+02	-.2666+02
Y	LINEAR DISPLACEMENT RELATIVE TO OVERALL VEHICLE COORDINATES	.0000	.0000
Z		-.3300+01	.2770+01
AW	SECTION LIFT CURVE SLOPE	.6000+01	.6000+01
SW	REFERENCE AREA	.2400+02	.2460+02
CHORD	REFERENCE CHORD	.3880+01	.4250+01
CD0	SECTION CD AT ALPHA=0.	.0000	.0000
CD1	SECTION CD/ALPHA	.0000	.0000
CD2	SECTION CD/ALPHA/ALPHA	.0000	.0000
AWCLD	ALPHA AT CD-MINIMUM	.0000	.0000
CAP GAMMA	DIHEDRAL ANGLE	.0000	.0000
BW	REFERENCE SPAN	.6200+01	.5800+01
LAMDA W	TAPER RATIO	.0000	.0000
CM0	CM AT ALPHA=0.	.0000	.0000
CMA	CM/ALPHA	.0000	.0000

93

TABLE II - MOSTAB INPUT DATA (CONTINUED)
WING CHARACTERISTICS   (RADIAN,FOOT,SECOND)

MOSTAB SYMBOL	DEFINITION	SIKORSKY S-5R	LOCKHEED AH-56A
PSI L			.0000
THETA L	ANGULAR DISPLACEMENTS RELATIVE TO OVERALL VEHICLE COORDINATES		.1660-00
PHI L			.0000
X			-.6500-00
Y	LINEAR DISPLACEMENT RELATIVE TO OVERALL VEHICLE COORDINATES		.0000
Z			.3400+01
AW	SECTION LIFT CURVE SLOPE		.6000+01
SW	REFERENCE AREA		.1950+03
CHORD	REFERENCE CHORD		.7250+01
CD0	SECTION CD AT ALPHA=0.		.8000-02
CD1	SECTION CD/ALPHA		-.7000-02
CD2	SECTION CD/ALPHA/ALPHA		.1470-00
AWCLD	ALPHA AT CD-MINIMUM		.1750-01
CAP GAMMA	DIHEDRAL ANGLE		.0000
BW	REFERENCE SPAN		.2700+02
LAMDA W	TAPER RATIO		.5100-00
CM0	CM AT ALPHA=0.		-.6100-01
CMA	CM/ALPHA		.0000

TABLE II - MOSTAB INPUT DATA (CONTINUED)
MAIN ROTOR CHARACTERISTICS   (RADIAN,FOOT,SECOND,SLUG)

MOSTAB SYMBOL	DEFINITION	SIKORSKY S-5A	LOCKHEED AH-56A
OMEGA	ROTATIONAL VELOCITY	.2325+02	.2570+02
B0	CONSTANT TIP LOSS FACTOR	.9700-00	.9700-00
BA	VARIABLE TIP LOSS FACTOR	.1680-02	.1760-02
BB	EXTRA TIP LOSS FACTOR	.0000	.0000
DELTA 0	SECTION CD AT ALPHA=0.	.7500-02	.7500-02
DELTA 1	CD/ALPHA	.0000	.0000
DELTA 2	CD/ALPHA/ALPHA	.3200-00	.3200-00
DELTA 3	PITCH/FLAP COUPLING	.0000	.0000
THETA 1	TOTAL BLADE TWIST	-.1395-00	-.8730-01
R	BLADE RADIUS	.2800+02	.2570+02
SMALL B	NUMBER OF BLADES	.4000+01	.4000+01
SMALL A	SECTION LIFT CURVE SLOPE	.6000+01	.6000+01
PSI R	ANGULAR DISPLACEMENTS RELATIVE TO OVERALL VEHICLE COORDINATES.	.0000	.0000
THETA R		-.3300-01	.0000
PHI R		.0000	.0000
X	LINEAR DISPLACEMENT RELATIVE TO OVERALL VEHICLE COORDINATES	.2700-00	.0000
Y		.0000	.0000
Z		-.8200+01	-.4150+01
P	NAT.FLAP.FREQUENCY/OMEGA	.1020+01	.1150+01
BOE	ESTIMATED BETA,PSI=0.	.0000	-.5000-02
BDOE	ESTIMATED BETADOT,PSI=0.	.0000	.1000-02
PB	BETA PERTURBATION	.5000-02	.5000-02
PBD	BETADOT PERTURBATION	.1000-00	.1000-00
CHORD	CONSTANT CHORD BLADES	.1360+01	.2320+01

95

TABLE II - MOSTAB INPUT DATA (CONTINUED)
MAIN ROTOR DISTRIBUTED BLADE PROPERTIES-

BLADE STATION NUMBER	SIKORSKY S-5A		LOCKHEED AH-56A	
	RADIAL DISTANCE	DISTRIBUTED MASS	RADIAL DISTANCE	DISTRIBUTED MASS
1	.0000	.1360-00	.0000+01	.1000+01
2	.1000+01	.1360-00	.7700+02	.3800-00
3	.8400+01	.1360-00	.1160+02	.3800-00
4	.1340+02	.1360-00	.1540+02	.2700-00
5	.1690+02	.1360-00	.1800+02	.2700-00
6	.1960+02	.1360-00	.2050+02	.2700-00
7	.2180+02	.1360-00	.2170+02	.2700-00
8	.2370+02	.1360-00	.2310+02	.2700-00
9	.2530+02	.1360-00	.2430+02	.2700-00
10	.2670+02	.1360-00	.2570+02	.2700-00
11	.2800+02	.1360-00		

	INITIAL SHAPE	FIRST FLAPPING MODESHAPE	INITIAL SHAPE	FIRST FLAPPING MODESHAPE
1	.0000	.0000	.0000	.0000
2	.0000	.0000	-.1000-00	-.3800+01
3	.0000	-.7400+01	-.1500-00	-.7180+01
4	.0000	-.1240+02	-.1500-00	-.1100+02
5	.0000	-.1590+02	-.1500-00	-.1350+02
6	.0000	-.1860+02	-.1500-00	-.1610+02
7	.0000	-.2080+02	-.1500-00	-.1730+02
8	.0000	-.2270+02	-.1500-00	-.1850+02
9	.0000	-.2430+02	-.1500-00	-.1980+02
10	.0000	-.2570+02	-.1500-00	-.2110+02
11	.0000	-.2700+02		

POINT MASSES-

STATION NUMBER	RADIAL DISTANCE	MASS	RADIAL DISTANCE	MASS
1	.2800+02	.3477-00	.2570+01	.7700+01
2			.8950+01	.1000+01
3			.2570+02	.5000-01

	INITIAL SHAPE	FIRST FLAPPING MODESHAPE	INITIAL SHAPE	FIRST FLAPPING MODESHAPE
1	.0000	-.2700+02	-.7500-01	-.7400-00
2			-.1500-00	-.4880+01
3			-.1500-00	-.2110+02

TABLE II - MOSTAB INPUT DATA (CONTINUED)
TAIL ROTOR CHARACTERISTICS (RADIAN,FOOT,SECOND,SLUG)

MOSTAB SYMBOL	DEFINITION	SIKORSKY S-58	LOCKHEED AH-56A
OMEGA	ROTATIONAL VELOCITY	.1390+03	.1300+03
BO	CONSTANT TIP LOSS FACTOR	.9700-00	.9500-00
BA	VARIABLE TIP LOSS FACTOR	.0000	.0000
BB	EXTRA TIP LOSS FACTOR	.0000	.0000
DELTA·0	SECTION CD AT ALPHA=0.	.1000-01	.1000-01
DELTA 1	CD/ALPHA	.0000	.0000
DELTA 2	CD/ALPHA/ALPHA	.3200-00	.3200-00
DELTA 3	PITCH/FLAP COUPLING	-.1000+01	.0000
THETA 1	TOTAL BLADE TWIST	.0000	.0000
R	BLADE RADIUS	.4670+01	.5000+01
SMALL B	NUMBER OF BLADES	.4000+01	.4000+01
SMALL A	SECTION LIFT CURVE SLOPE	.6000+01	.6000+01
PSI R		.0000	.0000
THETA R	ANGULAR DISPLACEMENTS RELATIVE TO OVERALL VEHICLE COORDINATES	.0000	.0000
PHI R		.1570+01	.1570+01
X		-.3300+02	-.2990+02
Y	LINEAR DISPLACEMENT RELATIVE TO OVERALL VEHICLE COORDINATES	-.1750+01	-.6000+01
Z		-.5750+01	.0000
P	NAT.FLAP.FREQUENCY/OMEGA	.1000+01	.1000+01
BOE	ESTIMATED BETA,PSI=0.	.0000	.0000
BDOF	ESTIMATED BETADOT,PSI=0.	.0000	.0000
PB	BETA PERTURBATION	.5000-02	.5000-02
PBD	BETADOT PERTURBATION	.1000-00	.1000-00
CHORD	CONSTANT CHORD BLADES	.6120-00	.1170+01

97

TABLE II - MOSTAB INPUT DATA (CONTINUED)
TAIL ROTOR DISTRIBUTED BLADE PROPERTIES-

BLADE STATION NUMBER	SIKORSKY S-58		LOCKHEED AH-56A	
	RADIAL DISTANCE	DISTRIBUTED MASS	RADIAL DISTANCE	DISTRIBUTED MASS
1	.0000	.2560-01	.0000	.1000-00
2	.1400+01	.2560-01	.1000+01	.1000-00
3	.2230+01	.2560-01	.1500+01	.1000-00
4	.2820+01	.2560-01	.2000+01	.1000-00
5	.3270+01	.2560-01	.2500+01	.1000-00
6	.3640+01	.2560-01	.3000+01	.1000-00
7	.3950+01	.2560-01	.3000+01	.1000-00
8	.4220+01	.2560-01	.4000+01	.1000-00
9	.4460+01	.2560-01	.4500+01	.1000-00
10	.4670+01	.2560-01	.5000+01	.1000-00
	INITIAL SHAPE	FIRST FLAPPING MODESHAPE	INITIAL SHAPE	FIRST FLAPPING MODESHAPE
1	.0000	.0000	.0000	.0000
2	.0000	.1400+01	.0000	.1000+01
3	.0000	.2230+01	.0000	.1500+01
4	.0000	.2820+01	.0000	.2000+01
5	.0000	.3270+01	.0000	.2500+01
6	.0000	.3640+01	.0000	.3000+01
7	.0000	.3950+01	.0000	.3500+01
8	.0000	.4220+01	.0000	.4000+01
9	.0000	.4460+01	.0000	.4500+01
10	.0000	.4670+01	.0000	.5000+01

TABLE II - MOSTAB INPUT DATA (CONTINUED)
PROPELLER CHARACTERISTICS   (RADIAN,FOOT,SECOND,SLUG)

MOSTAB SYMBOL	DEFINITION	SIKORSKY S-5A	LOCKHEED AH-56A
OMEGA	ROTATIONAL VELOCITY		.1800+03
BO	CONSTANT TIP LOSS FACTOR		.9500-00
BA	VARIABLE TIP LOSS FACTOR		.0000
BB	EXTRA TIP LOSS FACTOR		.0000
DELTA 0	SECTION CD AT ALPHA=0.		.8000-02
DELTA 1	CD/ALPHA		.0000
DELTA 2	CD/ALPHA/ALPHA		.3200-00
DELTA 3	PITCH/FLAP COUPLING		.0000
THETA 1	TOTAL BLADE TWIST		.2600-00
R	BLADE RADIUS		.5000+01
SMALL B	NUMBER OF BLADES		.3000+01
SMALL A	SECTION LIFT CURVE SLOPE		.6000+01
PSI R			.0000
THETA R	ANGULAR DISPLACEMENTS RELATIVE TO OVERALL VEHICLE COORDINATES		.1570+01
PHI R			.0000
X			-.3129+02
Y	LINEAR DISPLACEMENT RELATIVE TO OVERALL VEHICLE COORDINATES		.0000
Z			.0000
P	NAT.FLAP.FREQUENCY/OMEGA		.0000
BOE	ESTIMATED BETA,PSI=0.		.0000
BDOE	ESTIMATED BETADOT,PSI=0.		.0000
PB	BETA PERTURBATION		.0000
PBD	BETADOT PERTURBATION		.0000
CHORD	CONSTANT CHORD BLADES		.1000+01

TABLE II - MOSTAB INPUT DATA (CONCLUDED)
PROPELLER DISTRIBUTED BLADE PROPERTIES-

DISTRIBUTED BLADE PROPERTIES-

BLADE STATION NUMBER	SIKORSKY S-58		LOCKHEED AH-56A	
	RADIAL DISTANCE	DISTRIBUTED MASS	RADIAL DISTANCE	DISTRIBUTED MASS
1			.0000	.1000-00
2			.1000+01	.1000-00
3			.1500+01	.1000-00
4			.2000+01	.1000-00
5			.2500+01	.1000-00
6			.3000+01	.1000-00
7			.3000+01	.1000-00
8			.4000+01	.1000-00
9			.4500+01	.1000-00
10			.5000+01	.1000-00

	INITIAL SHAPE	FIRST FLAPPING MODESHAPE	INITIAL SHAPE	FIRST FLAPPING MODESHAPE
1			.0000	.0000
2			.0000	.1000+01
3			.0000	.1500+01
4			.0000	.2000+01
5			.0000	.2500+01
6			.0000	.3000+01
7			.0000	.3500+01
8			.0000	.4000+01
9			.0000	.4500+01
10			.0000	.5000+01

INDUCED VELOCITY ORIGINATING FROM LOADS ON THE FOLLOWING COMPONENTS		COMPONENT VELOCITY AFFECTED BY THE INDUCED VELOCITY		INDUCED VELOCITY MULTIPLYING FACTORS	
				SIKORSKY S-5A	LOCKHEED AH-56A
FUSELAGE	(U)	FUSELAGE	(U)	.0000	.1000+01
	(V)		(V)	.0000	.1000+01
	(W)		(W)	.0000	.1000+01
	(U)	HORIZONTAL	(U)	.1000+01	.0000
	(U)	VERTICAL	(U)	.1000+01	.0000
	(U)	PROPELLER	(U)		.1000+01
	(U)	TAIL ROTOR	(U)	.1000+01	
	(W)		(W)		.1500+01
HORIZONTAL TAIL	(U)	HORIZONTAL TAIL	(U)	.0000	.1000+01
	(V)		(V)	.0000	.1000+01
	(W)		(W)	.1000+01	.1000+01
WING	(U)	WING	(U)		.1000+01
	(V)		(V)		.1000+01
	(W)		(W)		.1000+01
	(W)	MAIN ROTOR	(W)		.1000+01
VERTICAL TAIL	(U)	VERTICAL TAIL	(U)	.0000	.1000+01
	(V)		(V)	.1000+01	.1000+01
	(W)		(W)	.0000	.1000+01
MAIN ROTOR	(U)	MAIN ROTOR	(U)	.1000+01	.1000+01
	(V)		(V)	.1000+01	.1000+01
	(W)		(W)	.1000+01	.1000+01
	(W)	WING	(W)		.1600+01
	(W)	HORIZONTAL	(W)	.1600+01	.0000
TAIL ROTOR	(U)	TAIL ROTOR	(U)	.0000	.1000+01
	(V)		(V)	.1000+01	.1000+01
	(W)		(W)	.0000	.1000+01
PROPELLER	(U)	PROPELLER	(U)		.1000+01
	(V)		(V)		.1000+01
	(W)		(W)		.1000+01

For the YHC-1A it was decided not to employ MOSTAB to calculate the derivatives. This was because published derivatives were available from Ref. 29. These derivatives were calculated by the manufacturer and use simple downwash models, not including the cyclic variation of tip loss factor, B. Some accuracy is lost because of this. On the other hand, the manufacturer undoubtedly possesses good information on the important interference effects between front and rear rotors. This would have to be estimated if the YHC-1A derivatives were calculated by MOSTAB. It was felt that the errors incurred in such estimates would exceed those caused by oversimplified tip loss models. Thus, the manufacturer's derivatives are used.

The resulting derivatives are presented in Volumes III and IV (together with the transfer functions) for the flight conditions tabulated in Table III below. For the S-58 and AH-56A, the maximum rate of descent corresponds approximately to the upper boundary of the vortex-ring state.

TABLE III. FLIGHT CONDITIONS		
HELICOPTER	TOTAL SPEED (knots)	RATE OF DESCENT (fps)
AH-56A	20, 40, 60, 100	0, 9.2, 19.2, 28.8, at each speed
	Vertical Descent	0, 9.2, 19.2, 28.8
S-58	20, 40, 60, 100	0, 7.5, 15 22.5 at each speed
	Vertical Descent	0.9, 9.2, 19.2, 28.8
YHC-1A	60.1	0, 25
	80.1	0, 25
	Vertical Descent	0, 25

V.7   CORRELATION OF DERIVATIVES WITH FLIGHT TEST DATA

Before presenting transfer functions based on the published YHC-1A derivatives and the AH-56A and S-58 derivatives calculated by MOSTAB, it is highly desirable to check the accuracy of these derivatives. The only really satisfactory check is to compare calculated derivatives with those deduced from flight tests. Unfortunately, many derivatives are hard to obtain from flight tests, and only incomplete flight test data were available for the helicopters of interest. However, an incomplete check is better than none at all, so this section summarizes the comparisons that were made between calculated derivatives and the available flight test data.

In brief:

(i)   For the YHC-1A, the results of steady sideslip flight tests were available. These substantiate the published derivatives $Y_{\delta A}$, $L_{\delta A}$, $N_{\delta A}$, Y_v, L_v, N_v, and $Y_{\delta R}$, $L_{\delta R}$, $N_{\delta R}$.

(ii)   For the S-58 flight test data showing time histories of responses to B_{1c}, longitudinal control inputs were compared to time histories predicted from the calculated derivatives. The agreement is good for the longitudinal degrees of freedom, but less so on the lateral motions induced by longitudinal-lateral cross-coupling. Unfortunately, it is not known whether any lateral control inputs were applied, so the accuracy of the cross-coupling derivatives remains uncertain. However, the longitudinal derivatives appear to be substantially correct.

(iii)   No flight test data were available for the AH-56A; wherever possible, manufacturer's wind-tunnel data were used as inputs to MOSTAB, and derivatives appear to be reasonable.

In general, there is little value in making comparisons between the MOSTAB derivatives and other calculated derivatives. This is because the other derivatives are generally calculated by less sophisticated programs which do not include all the interference velocities between components. For example, Ref. 24 presents S-58 derivatives and flight test data; however, the derivatives yield responses which do not agree with the test data. This is principally due to the neglect of main rotor downwash on the tail and tail rotor, giving inaccurate M_w. Adequate flight test data are difficult to obtain, but they constitute the only valid criteria against which calculated derivatives may be checked.

YHC-1A Flight Tests

Ref. 30 describes steady sideslip tests performed on a
YHC-1A in level flight at forward speeds of 45, 60, and 80 knots.
Derivatives for the latter two speeds are presented in Volume
III; and as shown in Ref. 30, the steady-state variation of lateral
stick position (δ_A) and rudder pedal position (δ_R) with sideslip
angle (B) can be predicted from the following equation, using
stability axis derivatives.

$$
\begin{bmatrix} Y_v & g & Y_{\delta_R} \\ L_v & 0 & L'_{\delta_R} \\ N_v & 0 & N_{\delta_R} \end{bmatrix} \begin{bmatrix} v \\ \phi \\ \delta_R \end{bmatrix} = - \begin{bmatrix} Y_{\delta_A} \\ L_{\delta_A} \\ N_{\delta_A} \end{bmatrix} \delta A
\tag{105}
$$

This solution applies even to a basically unstable aircraft such
as the YHC-1A, provided it is stabilized by feedbacks from yaw
and roll rates, these feedbacks being supplied either by the pilot
or the stability augmenter system. Figures 33 and 34 (taken from
Ref. 31) indicate that the calculated v, δ_R, and δ_A derivatives are
in reasonable agreement with flight test. Furthermore, the helicopter's
behavior is fairly linear with sideslip angle for moderate per-
turbations.

S-58 Flight Tests

Seckel (Ref. 25) presents geometric and inertial data on
the S-58, wind-tunnel data on components, and manufacturer's
estimates of derivatives for the helicopter flying at 5,000 feet
with a gross weight of 11,600 pounds. Flight test data are also
shown, i.e., time histories of a response to a longitudinal stick
input in pitch rate, angle of attack, normal acceleration, and
airspeed. These time histories are reproduced from the original
flight test report (Ref. 32), but for some variables the reproduction
is not sufficiently precise for purposes of checking derivatives.
Ref. 32 should, therefore, be used in preference to Ref. 25. In
addition, Ref. 32 includes the time histories of the lateral degrees
of freedom (although the lateral control time histories are not
recorded).
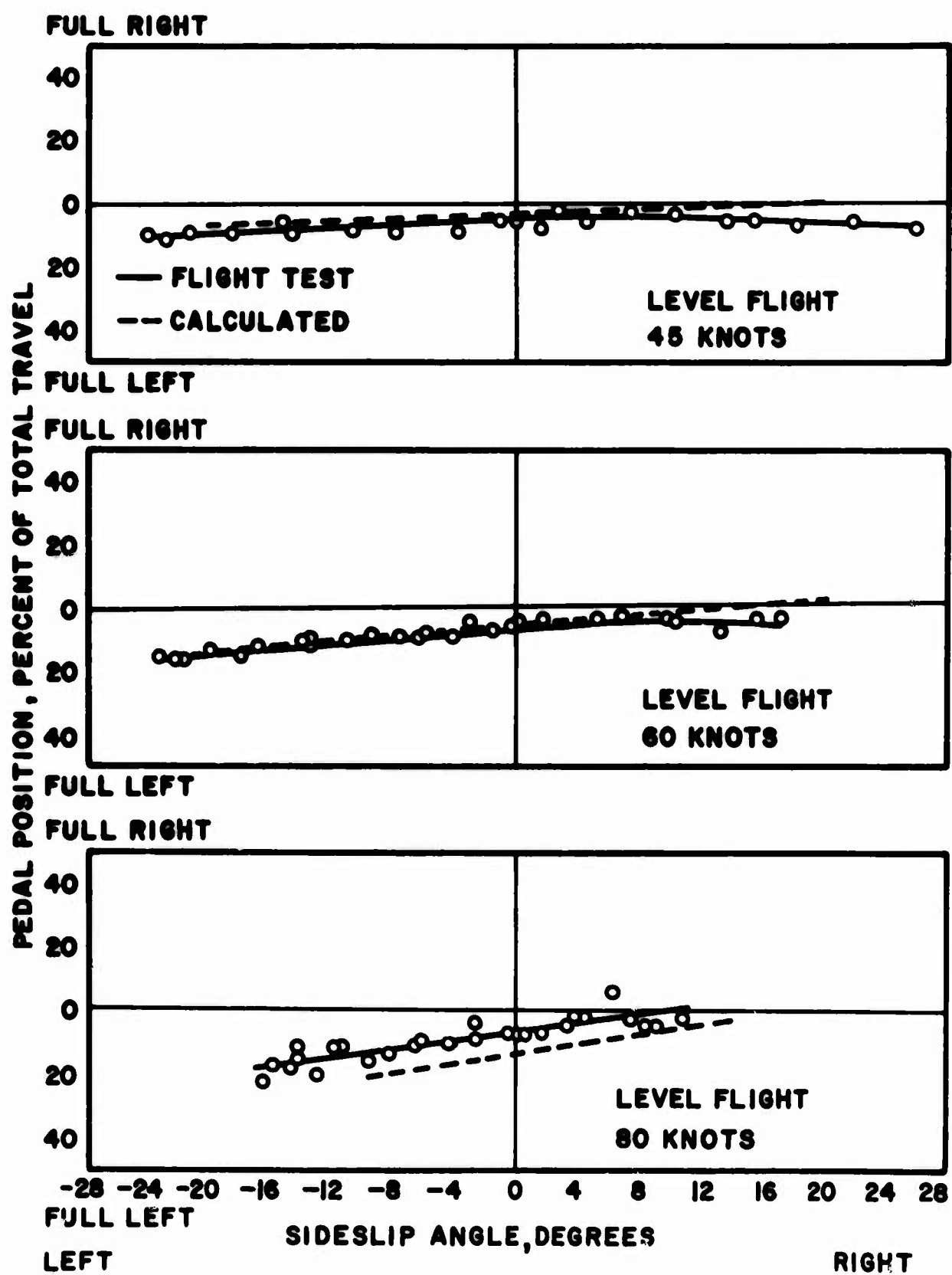
Figure 33. YHC-1A Pedal Position Versus Sideslip Angle.

105
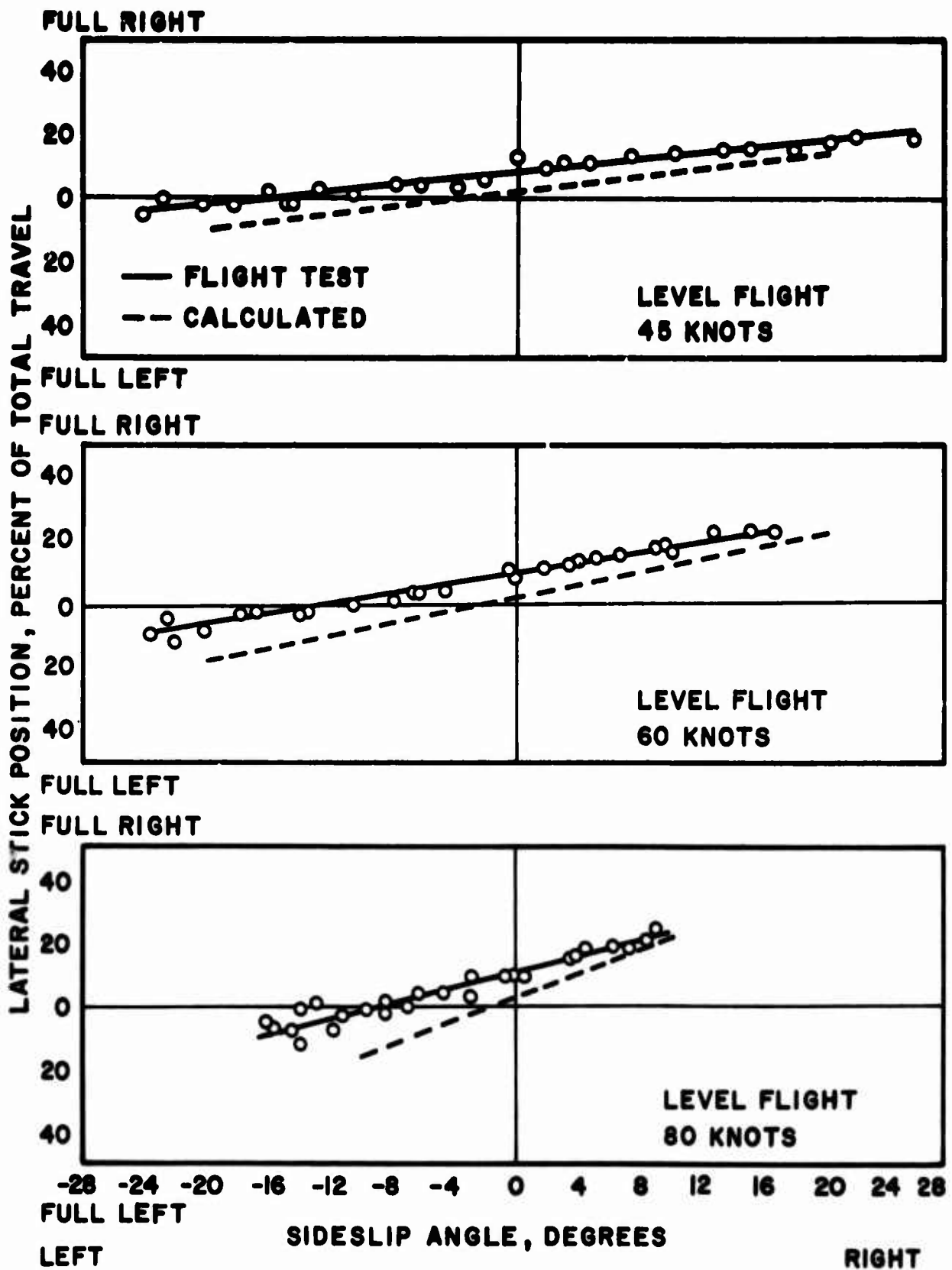
Figure 34. YHC-1A Stick Position Versus Sideslip Angle.

106

The time history response following a step B_1 input from trim (-0.015 rad.) at 74 knots C.A.S., 5000 ft., level flight, was selected from the available flight test histories of Ref. 32. The appropriate six-degree-of-freedom stability derivatives generated from MOSTAB are shown in Table IV. The derivatives were input into program ZEPLIN, which solves the six-degree-of-freedom, small-perturbation, linear equations of motion and obtains eigenvalues $(R + jI)$ and the modulus and angle of corresponding residue vectors (L, A) for response to a unit B_1 step. The eigenvalues and residue matrix are shown

on Table V. The aircraft response was then obtained using the following relationship:

$$\text{Response} = B_1 \sum_{r=1}^{r=n} e^{R_r t} \left[(L_r \, Cos A_r) \, Cos \, I_r t - (L_r Sin \, A) \, Sin \, I_r t \right]$$

(106)

The comparison of the MOSTAB-generated and experimental time histories for the selected flight condition is shown on Figure 35. For longitudinal motions, there is excellent agreement with airspeed, pitch angle, and angle of attack, but poor agreement with pitch rate. This discrepancy is attributed to malfunctioning pitch rate instrumentation, because the measured pitch rate does not agree with the differentiated pitch attitude.

For lateral - directional motion (Figure 36), the flight test results show an initial roll and yaw to the right; however, MOSTAB derivatives show a roll and yaw to the left. There is a possibility that the pilot applied some roll control as he pulled back the stick, but the disagreement may be due to too large a MOSTAB-generated value for L_q (-10,940 ft - lb -sec), causing a strong left rolling moment as the vehicle pitches up. Further studies and flight test comparisons will be required to produce a suitable explanation for this disagreement between time histories.

Summary

The MOSTAB program has been described in general, avoiding technical detail which is given in Volume II. Flight test data are limited, but they generally support the values of derivatives used for the YHC-1A and S-58.

TABLE IV S-58 DERIVATIVES FOR FLIGHT TEST CONDITION

SIKORSKY S-58 73 KNOTS 5000 FT. LEVEL FLIGHT FWD. C.G.
SEE REFS. 25 AND 32

VEHICLE
WEIGHT	XCG	YCG	ZGG
.1197+05	.9400-00	.0000	.0000

STABILITY DERIVATIVE MATRICES

	U	V	W	P	Q	R
X	-.1361+02	-.2267-00	-.1557+01	-.7005+03	.1244+04	-.1142+03
Y	.1098+01	-.3349+02	-.2662+01	-.1360+04	-.6969+03	.4766+03
Z	-.7200+01	-.3777+01	-.2183+03	-.7174+03	-.3487+02	.9191+03
L	.2137+02	-.2062+03	.1326+02	-.2033+05	-.1094+05	.2179+04
M	.1106+03	.1790+02	.5892+02	.1070+05	-.2400+05	.1189+04
N	-.7655+02	.3494+03	-.2985+03	-.4758+03	.1070+05	-.1969+05

	U DOT	V DOT	W DOT	P DOT	Q DOT	R DOT
X	.3690-02	-.8526-03	-.4382-01	-.2570+02	-.9115+01	-.2130+01
Y	-.7242-02	.6685-01	.8638-01	.9947+01	-.2444+02	-.1500+01
Z	.1053-03	-.1471-02	-.8709-03	-.8389-00	-.8005-00	-.2350-01
L	-.1981-00	.5054-00	.2353+01	.2673+04	-.3945+03	.2080+03
M	-.1607-00	-.5245-01	.1959+01	.4154+03	.2672+04	.3676+02
N	.8099-02	-.2248+01	-.1042+00	-.4841+02	-.5217+02	.7643+02

	C(1)	C(2)	C(3)	C(4)
X	-.3872+04	-.6976+03	.1218+05	-.1047+03
Y	-.6522+03	.1258+05	.1009+04	.4204+04
Z	-.9315+05	-.3025+02	.2802+05	-.1032+03
L	.6394+03	.1882+06	.3210+04	.3163+05
M	.9605+05	.5190+04	-.1940+06	-.3360+04
N	.7851+05	.4805+03	.3463+05	-.1414+06

THE INERTIA TENSOR	.5940+04	.0000	-.8800+03
	.0000	.2750+05	.0000
	-.8800+03	.0000	.2304+05

TRIMMED VELOCITIES WITH RESPECT TO OVERALL VEHICLE REFERENCE AXES-

U	V	W	P	Q	R
.1230+03	-.0000	-.6314+01	-.0000	.0000	-.0000

TRIMMED ITERATION COLUMN VECTOR, TE-
.2507-00 -.1755-01 .2118-01 .8137-01 -.5127-01 -.1546-01
STABILITY AXIS SYSTEM EULER ANGLES- THETA= .1220-04 PHI -.1544-01
AIRCRAFT INERTIAL SPEED= .1232+03

TABLE V S-5A RESIDUES AND EIGENVALUES FOR FLIGHT TEST CONDITION

EIGENVALUES

R	-.1178+00	-.6281+01	-.6549-00	.4182-01	.4182-01	-.3357-00
I	.0000	.0000	.0000	.3289-00	-.3289-00	.1316+01
L	.1178+00	.6281+01	.6549-00	.3316-00	.3316-00	.1358+01
A	.1800+03	.1800+03	.1800+03	.8275+02	-.8275+02	.1043+03

VECTORS

U	L	.4269+01	.8381-01	.7356+02	.8357+03	.8357+03	.2774+01
	A	.0000	.0000	.0000	.1754+03	-.1754+03	-.9867+02
V	L	.1443+02	.6195-00	.1719+04	.3806+03	.3806+03	.1377+03
	A	.0000	.0000	.0000	.1592+03	-.1592+03	-.1795+03
W	L	.8962-00	.4391-00	.1775+04	.4901+03	.4901+03	.2077+02
	A	.0000	.0000	.0000	.1308+03	-.1308+03	-.1427+03
P	L	.1140+00	.2586-00	.1626+02	.4366+01	.4366+01	.1251+01
	A	.1800+03	.0000	.1800+03	-.2918+02	.2918+02	-.3267+01
Q	L	.5689-02	.1626-01	.1407+01	.2941+01	.2941+01	.2553-00
	A	.1800+03	.1800+03	.1800+03	.1572+03	-.1572+03	-.6254+02
R	L	.2623-00	.1257-01	.1492+02	.2467+01	.2467+01	.1322+01
	A	.0000	.0000	.0000	-.1046+03	.1046+03	.1077+03

EIGENVALUES

R	-.3357-00	-.1267+01	.0000	.0000	.0000	.0000
I	-.1316+01	.0000	.0000	.0000	.0000	.0000
L	.1358+01	.1267+01	.0000	.0000	.0000	.0000
A	-.1043+03	.1800+03	.0000	.0000	.0000	.0000

VECTORS

U	L	.2774+01	.1487+03	.1502+03	.0000	.0000	.0000
	A	.9867+02	.1800+03	.1800+03	.0000	.0000	.0000
V	L	.1377+03	.9137+03	.0000	.1084+05	.0000	.0000
	A	.1795+03	.1800+03	.0000	.0000	.0000	.0000
W	L	.2077+02	.1158+04	.0000	.0000	.1160+03	.0000
	A	.1427+03	.1800+03	.0000	.0000	.0000	.0000
P	L	.1251+01	.5993+01	.0000	.0000	.0000	.3745-03
	A	.3267+01	.0000	.0000	.0000	.0000	.0000
Q	L	.2553-00	.6573+01	.0000	.0000	.0000	.4741-00
	A	.6254+02	.0000	.0000	.0000	.0000	.0000
R	L	.1322+01	.1028+02	.0000	.0000	.0000	.3070+02
	A	-.1077+03	.1800+03	.0000	.0000	.0000	.1800+03
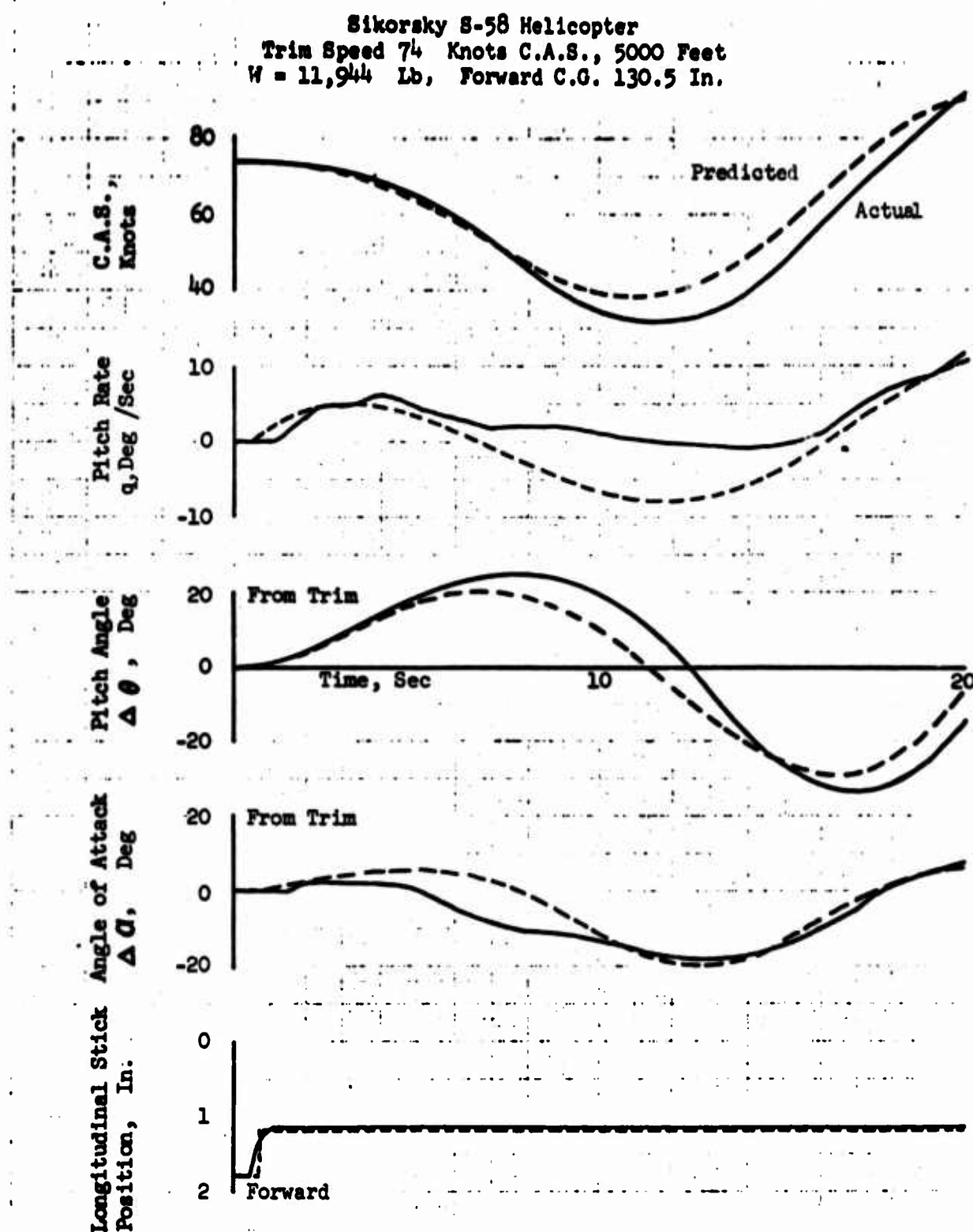
Figure 35. A Comparison of Longitudinal Flight Test Response Following a Step Pitch Control Input to a Response Based on Stability Derivatives Obtained From MOSTAB.

110
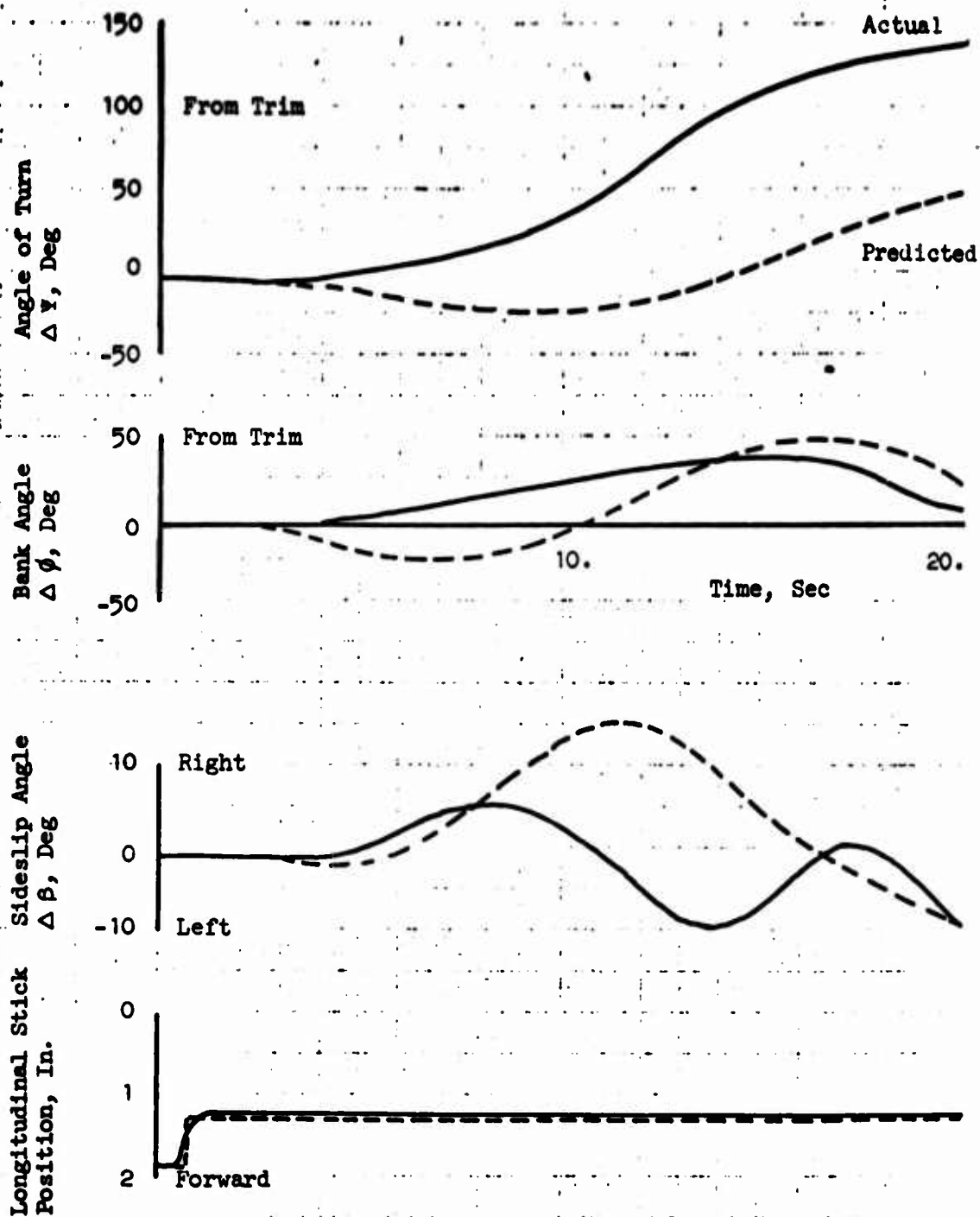
Figure 36. A Comparison of Lateral Flight Test Response
Following a Step Pitch Control Input to a Response
Based on Stability Derivatives Obtained from MOSTAB.

111

CHAPTER VI. TANDEM-ROTOR HELICOPTER
OPEN-LOOP DYNAMICS

VI.1 INTRODUCTION

In this section we consider the transfer functions of the YHC-1A, which is taken to represent a typical tandem-rotor helicopter. The transfer functions are presented in Volume III. Unlike the single-rotor and compound configurations, for the tandem configuration lateral-longitudinal cross-coupling effects were neglected; thus, separate lateral and longitudinal transfer functions were calculated.* The format of the transfer function print-out is explained below.

The format is basically similar to that of Reference 33, but a number of detailed refinements have been added. These include additional sets of numerators referred to a station distant from the c.g. The coordinates of this station are conveniently chosen as the location of the pilot, to relate pilot cues to the motion of the c.g. of the aircraft.

VI.2 LONGITUDINAL DYNAMICS

As noted in Volume III, the derivatives are inputted in body (i.e., waterline) axes. The input format of the program used contains a number of redundancies, e.g., Mach number, which are arbitrarily put to zero.

The print-out, in Volume III, gives:

(i)   Derivatives in stability axes

(ii)   Eigenvalues, and associated information, such as
       the coefficients of the denominator quartic

(iii) Numerators for the pitch attitude control, which is
       here designated " CYCLIC " .

Actually, the YHC-1A control is predominantly differential collective, though some cyclic variation is included as shown by the non-zero X_{δ_e} at hover. For each numerator the roots, D.C. gain (i.e., Bode gain), and root locus gain are presented. In addition, various secondary items of information such as the coefficients of the numerator polynomial are printed out. The numerators correspond to θ, u, w, a_z (as measured by an accelerometer, $a_z = \overset{\circ}{w} - U_o q + g \sin \gamma_o \int q \, dt$), and

---

*   The equations of motion are the standard longitudinal and lateral
     sets. These can be obtained from the coupled equations given in
     Chapter VII by neglecting all cross-coupling terms.

horizontal velocity perturbations $\overset{\circ}{x}$ ($= u$ for $\gamma_0 = 0$). In addition, the print-out includes rate-of-climb perturbations ($\overset{\circ}{h} - h_0$) and perturbations in velocities parallel and normal to the undisturbed flight path. Note that only for $\gamma_0 = 0$ is the normal velocity perturbation equal to the rate-of-climb perturbation.

For steep approaches, the "normal velocity" perturbation indicates the rate of deviation from the desired flight path. The "parallel velocity" perturbation indicates the rate of deviation from the desired position along the desired flight path. Hence, this quantity is important for stationkeeping, e.g., in formation flight or scheduling of multiple operations.

Longitudinal Eigenvalues

For ease of reference in the subsequent discussion, the eigenvalues are summarized in Table VI below.

TABLE VI. TANDEM-ROTOR LONGITUDINAL DENOMINATORS			
Rate of Descent (fpm)	Horiz.* Speed (knots)	Case No.	Eigenvalues (rad/sec)
0	0	L5	$-.974, \ -.35, \ .099 \pm .45\,j$
1500	0	L6	$-.824, \ -.25, \ .109 \pm .70\,j$
0	60	L3	$-2.34, \ -.214 \pm .345j, \ .473$
1500	60	L4	$-2.35, \ -.35 \pm .29j, \ .406$
0	80	L1	$-2.50, \ -.212 \pm .33j, \ .43$
1060	80	--	$-2.37, \ -.31 \pm .32j, \ .400$
1500	80	L2	$-2.36, \ -.35 \pm .29j, \ .406$

Before discussing the changes that occur between level flight and steep descent, the nature of the modes for level flight will be reviewed.

---

* This column shows horizontal speed, not total speed, and is therefore zero for vertical descent.

For level flight, the eigenvalues are distributed similarly to those of the HUP-1 given in Reference 34 (p. 258). The principal difference is about a 50% reduction in the magnitude (i.e., frequency). This would be expected from the increased mass and size of the YHC-1A (see Reference 35). It appears, therefore, that the general conclusions of Reference 34 regarding the physical nature of the modes should still be valid. That is, away from hover, the motion consists of three modes, one of which is aperiodic and appreciably larger than the others. This mode is a degenerate short-period mode with time constant T_{sp_1} approximated by the standard formula

$$\frac{1}{T_{sp_1}} = \frac{-(M_q + Z_w + U_o M_{\dot{w}})}{2} + \sqrt{\frac{(M_q + Z_w + U_o M_{\dot{w}})^2}{2} + U_o M_w - M_q Z_w}$$

(107)

This mode contains little u and is dominated by w and θ motions.

The remaining modes involve u, w, and θ and can be traced to the effect of the negative M_u on the short-period roots. The root-locus presentation of page 119 of Reference 34 can be used to predict the eigenvalues, with the condition that $-Z_w + (Z_u M_w/M_u) < 0$. In summary, the open-loop longitudinal modes in level flight are the conventional modes for a tandem-rotor helicopter, as predicted in Reference 34.

In this report, our principal concern is to detect and study changes in dynamic characteristics from the level flight condition, so we shall now consider the descent cases; a more complete discussion of level flight dynamics of tandem-rotor helicopters is given in Reference 34.

At 60 and 80 knots, descent angle has little effect on the denominator roots, as shown by Table VI. The only significant change is an increase in phugoid damping. This would be expected, since the phugoid damping increases with $-X_u$. X_u depends on the trimmed drag/lift ratio, which of course must increase to balance out the X-force gravity component in descent.

For vertical descent, the changes are also rather small. Hence, if any marked changes in tandem-rotor control characteristics occur, when going from level flight to descent at the same horizontal speed, the changes must be associated with the transfer function numerators. These will now be discussed.

114

At a given horizontal speed, the $\theta/\delta e$ numerator shows little change with rate of descent. For ease of reference, the $\theta/\delta e$ numerators are summarized below. We employ the convention that a positive time constant is "stable"; i.e., the zero is in the left-half complex plane.

TABLE VII. TANDEM-ROTOR θ/δ_e NUMERATORS					
Rate of Descent (fpm)	Horiz. Speed (knots)	Case No.	Root-Locus Gain	$1/T_{\theta_1}$ (rad/sec)	$1/T_{\theta_2}$ (rad/sec)
0	0	L5	.355	+.019	+.3789
1500	0	L6	.3436	+.0156	+.267
0	60	L3	.45	+.035	+.817
1500	60	L4	.47	+.0312	+.912
0	80	L1	.48	+.043	+.935
1500	80	L2	.50	+.038	+.99

The effect of descent on $1/T_{\theta_1}$, $1/T_{\theta_2}$ is slight. As noted above, the changes in the denominator roots are also small. Hence, any effect of descent on pitch control must be associated with feedbacks other than θ. One of the most common feedbacks for tandem-rotor configurations is $u \rightarrow \delta e$. This is employed to correct the negative M_u characteristic of tandem-rotor helicopters at forward speed. Accordingly, the u/δ_e transfer functions are examined below.

Volume III presents u numerators in stability axes, and also in axes parallel to the stability axes, but located 17 feet farther forward, at the cockpit. The latter axis system is appropriate when considering feedbacks from air data, since such data are measured well forward on the fuselage to minimize rotor downwash effects. For inertial systems using stable platforms or frequently updated corrections obtained from ground tracking equipment applied to strapdown components, "stability axes" with origin at the c.g. appear to be more appropriate. Thus, for S.A.S. design and such pilot tasks as stationkeeping, the "cockpit" axes are appropriate, whereas for inertial guidance the usual "stability" axes are relevant. As shown below, the two sets of numerators show marked differences.

First, consider the $u \to \delta_e$ stability axis numerators tabulated below. Root locations are presented here, not inverse time constants; i.e., a negative real part of the root location indicates a "stable" root.

TABLE VIII. TANDEM-ROTOR u/δ_e NUMERATORS IN STABILITY AXES				
Rate of Descent (fpm)	Horiz. Speed (knots)	Case No.	Root-Locus Gain	Root Locations (rad/sec)
0	80	L1	.185	-9.99, -1.14, 6.84
1500	80	L2	.312	-10.35, -.656, 7.45
0	60	L3	.189	-10.2, -.87, 7.07
1500	60	L4	.37	-9.08, -.567, 6.83
0	0	L5	.178	-9.05, -.37, 7.118
1500	0	L6	.13⁴	-1.045, 6.68, 14.39

At 60 and 80 knots, there is little change in the numerator with descent angle. The vertical descent case shows a marked change; however, u/δ_e referred to stability axes is unimportant for control in vertical descent, since u is then vertical, and is more logically controlled by collective, rather than by δ_e, which is the pitch attitude control.

Thus we conclude that, for inertial feedbacks referred to the c.g. and to the aircraft's desired flight path, there is little effect of descent on the vehicle open-loop or closed-loop dynamics. By contrast, for feedbacks using air data, or other data referred to the pilot's location, ahead of the c.g., the effect of descent angle is considerable, as indicated overleaf, in Table IX.

116

Rate of Descent (fpm)	Horiz. Speed (knots)	Case No.	Root-Locus Gain	Root Locations (rad/sec)
		TABLE IX.	TANDEM-ROTOR u/δ_e NUMERATORS IN COCKPIT AXES	
0	80	L1	.164	-1.71, 3.22, 16.1
1500	80	L2	.146	-.796 $\pm$ .639j, 105.9
0	60	L3	.142	-2.53, -1.34, 24.8
1500	60	L4	.126	-.789 $\pm$ .53j, 122.1
0	0	L5	.177	-9.05, -0.37, 7.11
1500	0	L6	.166	-1.32, -0.285, 50.36

Some significant changes occur in going from level flight to descent. At 80 knots, the right-half plane zero at 3.22 rad/sec joins with the left-half plane zero at 1.71 and forms a complex pair in the left-half plane. The third zero moves into the distant right half-plane, becoming too far out to be significant. Similar changes occur at 60 knots. These changes are potentially significant, because there are no near-cancellations between numerator and denominator in the transfer functions, listed below for ease of reference.

u/δe Transfer Functions at 80 Knots Horizontal Speed

Level Flight:

$$\frac{u}{\delta_e} \bigg/ _{cockpit} = \frac{.164\ (s + 1.71)(s - 3.22)(s - 16.1)}{(s + 2.50)(s + .212 \pm .33j)(s - .43)}$$

1500 fpm Descent:

$$\frac{u}{\delta_e} \bigg/ _{cockpit} = \frac{.146(s + .796 \pm .639\,j)(s - 105.9)}{(s + 2.36)(s + .35 \pm .29\,j)(s - .406)}$$

117

The rather small $1/T_{\theta_1}$ (see Table VII) limits the degree to which the unstable eigenvalue can be stabilized by θ and q feedback. Hence it is quite possible that the $u \rightarrow \delta_e$ feedback will be required to achieve stability, even if θ and q feedbacks are also employed. In these circumstances, the changes in the u/δ_e transfer function should be considered carefully when designing stability augmentation systems using air data recorded away from the c.g.

Let us now consider the effects of descent on collective pitch control. The primary function of collective pitch is to control the deviation of the aircraft c.g. normal to the desired flight path. The appropriate transfer function numerators are summarized below.

Rate of Descent (fpm)	Speed (knots)	Case No.	Root-Locus Gain	Root Locations (rad/sec)
		TABLE X. TANDEM-ROTOR COLLECTIVE PITCH NUMERATORS FOR VELOCITY PERTURBATIONS OF C. G. NORMAL TO DESIRED FLIGHT PATH		
0	80	L1	-9.51	-1.87, -.209, .495
1500	80	L2	-8.99	-1.13, -.778, .2148
0	60	L3	-8.56	-1.84, -.217, .548
1500	60	L4	-7.85	-.952 $\pm$ .3735j, .267
0	0	L5	-7.43	-.953, .105 $\pm$ .445j
0	1500	L6	-1.466	-.652, .054 $\pm$ 1.26j

At hover, the usual cancellation of the denominator roots occurs, leaving the transfer function as $\dot{h}/\delta_c = Z_{\delta_c}/(s - Z_w)$. For vertical descent, the above transfer function becomes $\dot{x}/\delta_c$ and is not important for practical flight control. Chapter VII shows that for single-rotor helicopters, control of velocity normal to the unperturbed flight by collective pitch becomes difficult at very low speeds ($\doteq 20$ knots) in steep descents. Unfortunately, derivatives were not available for the YHC-1A in such conditions, so it is not known whether this effect (due to an uncancelled right-half plane zero) also occurs on tandem-rotor helicopters.

118

The importance of the changes in the above numerators for descending flight is hard to assess in general, because the "normal velocity" collective control is affected by feedbacks to cyclic from u, q, and θ. Such feedbacks will probably be employed for inner-loop stabilization.

It is not feasible to discuss all the tandem-rotor longitudinal transfer functions that are tabulated in Volume III. However, from those that have been examined here, it would appear that descent angle does not cause radical changes in the transfer functions. The most important exception to this generalization is $u/\delta_e/$ cockpit. The numerator of this transfer function exhibits some significant changes, which should be considered when designing stability augmenter systems that employ M_u augmentation based on air data sensors located away from the c.g.

VI.3 LATERAL DYNAMICS

The lateral transfer function denominators for the YHC-1A are presented in Table XI. The table has been arranged to fit the following discussion which first considers the variation of the level flight denominators with forward speed, and then analyzes the effects of descent.

TABLE XI. TANDEM-ROTOR LATERAL EIGENVALUES						
Rate of Descent (fpm)	Horiz. Speed (knots)	Case No.	Eigenvalues (rad/sec)			
0	0	L5	.0594	$\pm$	.511j	-.057	-.975
0	60	L3	.225	$\pm$	.604j	-.058	-1.29
0	80	L1	.281	$\pm$	.642j	-.0768	-1.36
1500	0	L6	.052	$\pm$	.707j	-.052	-.925
1500	60	L4	.134		.542	-.048	-1.77
1500	80	L2	-.140		.772	.0023	-1.832

119

The hover behavior is standard and closely analogous to the longitudinal case illustrated in Table VI. Note the close proximity of the frequencies of the longitudinal hovering phugoid ($\omega_p = 0.45$ rad/sec) and the lateral hovering dutch roll ($\omega_{dr} = 0.51$ rad/sec). As stated in Chapter V, for the tandem configuration, longitudinal-lateral cross-coupling was arbitrarily neglected. Undoubtedly, some coupling exists, and the near-coincidence of ω_{dr} and ω_p may make this coupling important for the YHC-1A. The question will only be settled by more extensive measurements of derivatives and flight test responses to control inputs.

The principal effect of descent at the higher speeds, is to change the unstable dutch roll oscillatory roots into an aperiodic pair. At 60 knots, both these roots are unstable; but as speed is increased one becomes stable while the other root moves farther out into the right-half plane. For the YHC-1A, this degeneration of the dutch roll roots into an aperiodic pair is a consequence of the low (actually negative) N_v.

N_v remains negative for all the level and descending forward flight conditions considered here, when measured in stability axes (which is the appropriate axis system for defining directional stability). It is difficult to design a tandem-rotor configuration with the c.g. far removed from the mid-point of the rotor axes; hence, negative N_v is characteristic of these configurations. It is usually "fixed" by feeding back p to δ_R to achieve static stability, plus additional feedbacks of $\dot\phi$ to δ_A, and possibly r to $\delta_{R \text{ command}}$, to move all the roots into the right-half plane and to achieve good turn coordination.

Feedback of sideslip alone is usually insufficient to ensure stability. This is illustrated in Figure 37 for the 80-knot level-flight case. Note the awkwardly-placed zero of the sideslip numerator. Because of the fundamental importance of directional stability for good handling qualities, particular interest attaches to the variation of the v/δ_R transfer functions with descent angle. Numerators of these transfer functions are tabulated below.

120
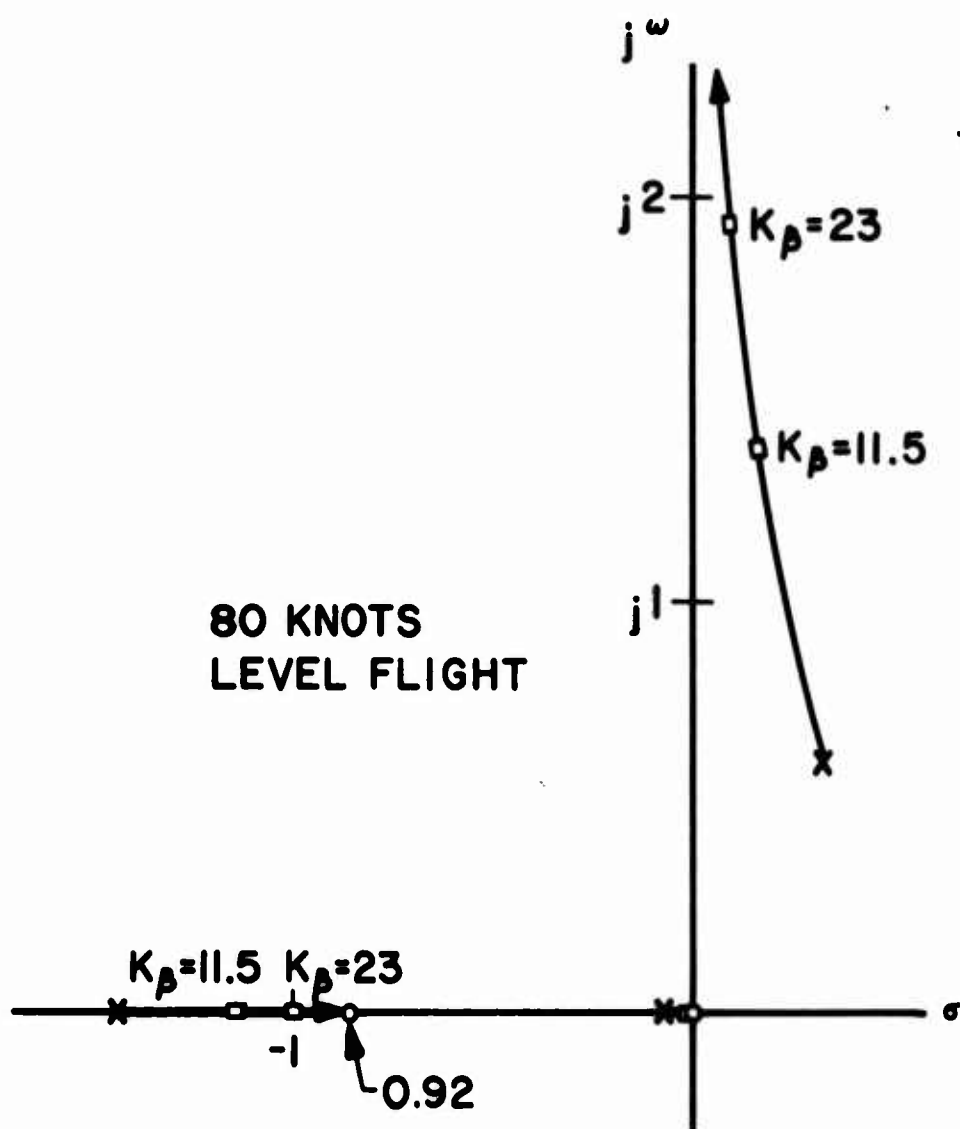
Figure 37. Root Locus for v → δ_R Feedback on
Tandem-Rotor Helicopter.

121

Rate of Descent (fpm)	Horiz. Speed (knots)	Case No.	Root -Locus Gain	Root Locations (rad/sec)
0	80	L1	.099	- .92, -.00145, 256.9
1500	80	L2	.07	- .41, -.020, 422.9
0	60	L3	.106	- .86, -.0025, 163.5
1500	60	L4	.073	- .151, -.0239, 524.9
0	0	L5	.146	- .0226, .79 $\pm$ 6.04j
1500	0	L6	.143	-1.33, -.055, 77.96

TABLE XII. TANDEM-ROTOR v/δ_R NUMERATORS

In these numerators, v is referred to stability axes. For analyzing stability augmenter systems, it is perhaps more meaningful to refer v to a location near the cockpit, where the sideslip sensing ports are located. However, as shown in Volume III , there is relatively little difference between the v/δ_R transfer functions referred to either location at 60 and 80 knots. The v/δ_R transfer function is not particularly important at zero forward speed, since v is then controlled directly through lateral cyclic pitch.

From Table XII, the effect of the descent on the v/δ_R numerators is seen to be relatively minor at 60 and 80 knots. The low-frequency zero limits the possible improvement of the unstable spiral root at 80 knots, suggesting that additional feedbacks (e.g., $\phi \rightarrow \delta_A$) are required to stabilize this root. The degenerate dutch roll modes may also require excessive gain for stabilization through $v \rightarrow \delta_R$ feedback alone. (The low accuracy to which v can be measured constrains practical $v \rightarrow \delta_R$ feedbacks to rather low gains.) The net effect of descent upon $v \rightarrow \delta_R$ feedback control seems to be adverse, and it appears that a system designed for level flight would not necessarily be suitable for steep approaches.

From the above discussion, $v \to \delta_R$ feedback appears to be mandatory for tandem-rotor helicopters. Such feedback represents an "inner loop" which will affect the other loop closures such as $\phi \to \delta_A$. In level flight, the ϕ/δ_A numerator exhibits some undesirable nonminimum phase characteristics[*] as noted in Reference 34. These become appreciably worsened in descent, as shown in Table XIII.

TABLE XIII. TANDEM ROTOR ϕ/δ_A NUMERATORS				
Rate of Descent (fpm)	Horiz. Speed (knots)	Case No.	Root -Locus Gain	Root Locations (rad/sec)
0	80	L1	.495	- .70, .543
1500	80	L2	.48	-1.09, .911
0	60	L3	.51	- .496, .368
1500	60	L4	.45	- .856, .70
0	0	L5	.55	- .249, -.057
1500	0	L6	.52	- .055 ± .02j

The poor handling qualities associated with the unaugmented ϕ/δ_A closure in level flight noted in Reference 34 are likely to become even more degraded in descent. For example, at 80 knots, the ϕ/δ_A transfer fraction has one right-half plane zero and two right-half plane real poles, thus presenting a situation which is quite difficult to stabilize.

An important feedback for human-pilot control is $y \to \delta_A$, where y is the lateral displacement of the helicopter measured either at the c.g. or at the cockpit.

---

[*] A nonminimum phase transfer function is one with one or more right-half plane zeros.

The print-out in **Volume** II includes both alternatives, however at the higher speeds the differences between the transfer functions for $y/\delta_{A/cockpit}$ and $y/\delta_{/c.g.}$ are relatively minor. For vertical descent the differences become more pronounced, as shown by the following comparison.

TABLE XIV.	EFFECT OF VERTICAL DESCENT ON TANDEM-ROTOR y/δ_A NUMERATORS MEASURED AT THE CENTER OF GRAVITY AND AT THE COCKPIT			
Flight Condition	Case No.	Location of Origin	Root -Locus Gain	Root Location (rad/sec)
Hover	L5	c.g.	.998	$-.082 \pm 4.22j$, $-.037$, $-.0177$
Hover	L5	cockpit	3.26	$-.108 \pm 2.33j$, $-.053$, $-.0123$
Vertical Descent	L6	c.g.	.98	$-.083 \pm 4.05j$, $-.051$, 0
Vertical Descent	L5	cockpit	$-.0116$	-26.7, $-.083$, 0, 52.8

A complete assessment of the significance of this difference in y/δ_A is beyond the scope of this report. It would involve loop closures using assumed models for the pilot; e.g. the "series closure" model used in Reference 36 and in the PAPER PILOT program described in Reference 37. The validity of these closures for conditions other than hover is subject to question. However, if the series closure is employed, the $y/\delta_{A/cockpit}$ and θ/δ_A transfer functions would be relevant for the inner and outer loops. As shown in Tables XIII and XIV, marked changes in these transfer functions occur between hover and vertical descent. It is therefore to be expected that correspondingly large changes in handling qualities will appear when going from hover to vertical descent.

Summary

In this chapter, we have reviewed the major effects of descent on the transfer functions of a typical tandem-rotor helicopter. It was assumed that longitudinal and lateral motions were uncoupled. Longitudinally, the effects of descent (at normal approach speeds of 60 to 80 knots) are generally minor. Some increase in phugoid damping occurs, but the important $\theta/\delta e$ pitch attitude control numerator hardly changes. Similarly, little change was observed in the u/δ_e numerator referred to stability axes.

However, marked changes occur in the u/δ_e numerator referred to body axes with origin at the cockpit. These changes are potentially significant for stability augmenter systems which employ air data sensors to augment M_u.

Laterally, the effects of descent are more noticeable. At forward speed the unstable dutch roll degenerates into an aperiodic pair, having at least one unstable root. This unstable root is usually stabilized by $v \rightarrow \delta_R$ feedback; however, this feedback has little effect on the spiral mode (which may be unstable) because of a "close-in" zero in the v/δ_R transfer function. This awkwardly placed zero is retained in descending flight. Thus, additional feedbacks (e.g., $\phi \rightarrow \delta_A$, $r \rightarrow \delta_R$) are still required to achieve good handling qualities. The nonminimum phase characteristics of the ϕ/δ_A numerator worsen in descent, thus increasing the need for still further feedbacks, such as $r \rightarrow \delta_p$. Because of the large number of feedbacks required, it is hard to form an assessment of the effects of descent on closed-loop characteristics without performing detailed calculations on various alternative loop closures. However, the changes in the transfer functions are sufficiently large and numerous to indicate the necessity of performing these calculations for descent in addition to level flight.

CHAPTER VII. SINGLE-ROTOR HELICOPTER DYNAMICS

VII.1. INTRODUCTION

This chapter discusses the open-loop and closed-loop dynamics of a typical single-rotor helicopter, the Sikorsky S-58. The basic data are presented in Volume III, which tabulates derivatives and eigenvalues.

The flight conditions presented in Volume III include level flight and rates of descent of 7.5 fps, 15 fps, and 22.5 fps. At low speeds the latter condition is virtually at the boundary of the vortex-ring state. For each rate of descent, true airspeeds of 0, 20, 40, 60 and 100 knots are considered.

All lateral-longitudinal cross-coupling derivatives were included, as shown by the equations of motion presented in Figure 38. To illustrate the importance of cross-coupling, one case was re-run with all cross-coupling derivatives set to zero. This was done for level flight at 100 knots.

The cyclically varying tip loss factor was included in all cases. To demonstrate the effect of tip losses on open-loop dynamics, two cases were re-run with tip losses removed. These cases were 22.5 fps rate of descent with 40 knots airspeed, and vertical descent at 22.5 fps.

Eigenvectors for u, v, w, p, q, r, in stability axes, residues for unit impulse inputs in A_{1s}, B_{1s}, θ_o, θ_{oTR}, and transfer functions relating u, v, w, p, q, r, to A_{1s}, B_{1s}, θ_o, θ_{oTR}, were also calculated for all the above cases. To save space, these data are not presented in full in Volume III, but selected values are given in this chapter where appropriate.

The main points discussed here are:

(i)   The effects of forward speed, rate of descent, and tip losses on the eigenvalues

(ii) Cross-coupling effects on open-loop dynamics as demonstrated by the eigenvectors

(iii) Cross-coupling effects on closed-loop dynamics and human pilot control as demonstrated by the transfer functions and residues

126

The volume of data generated for the S-58 is large, and it is not easy to condense it to its essentials. Only the "highlights" can be indicated here. The reader will gain worthwhile insight into helicopter dynamics by examining Volume III in detail.

$$[B]\{\dot{x}\} + [C]\{x\} = [F]$$

where

$$\{x\} = [\ u\ w\ q\ \theta\ v\ p\ \phi\ r\ ]^T$$

$$[C] = \begin{bmatrix}
-X_u & -X_w & -X_q & g\cos\gamma_o & -X_v & -X_p & 0 & -X_r \\
-Z_u & -Z_w & -U_o-Z_q & g\sin\gamma_o & -Z_v & -Z_p & 0 & -Z_r \\
-M_u & -M_w & -M_q & 0 & -M_v & -M_p & 0 & -M_r \\
0 & 0 & -1 & 0 & 0 & 0 & 0 & 0 \\
-Y_u & -Y_w & -Y_q & 0 & -Y_v & -Y_p & -g\cos\gamma_o & U_o-Y_r \\
-L_u & -L_w & -L_q & 0 & -L_v & -L_p & 0 & -L_r \\
0 & 0 & 0 & 0 & 0 & 1 & 0 & \tan\gamma_o \\
-N_u & -N_w & -N_q & 0 & -N_v & -N_p & 0 & -N_r
\end{bmatrix}$$

$$[F] = [\ X_\delta\ \ Z_\delta\ \ M_\delta\ \ 0\ \ Y_\delta\ \ L_\delta\ \ 0\ \ N_\delta\ ]^T$$

$$[B] = \begin{bmatrix}
1-X_{\dot u} & -X_{\dot w} & -X_{\dot q} & 0 & -X_{\dot v} & -X_{\dot p} & 0 & -X_{\dot r} \\
-Z_{\dot u} & 1-Z_{\dot w} & -Z_{\dot q} & 0 & -Z_{\dot v} & -Z_{\dot p} & 0 & -Z_{\dot r} \\
-M_{\dot u} & -M_{\dot w} & 1-M_{\dot q} & 0 & -M_{\dot v} & -M_{\dot p} & 0 & -M_{\dot r} \\
0 & 0 & 0 & 1 & 0 & 0 & 0 & 0 \\
-Y_{\dot u} & -Y_{\dot w} & -Y_{\dot q} & 0 & 1-Y_{\dot v} & -Y_{\dot p} & 0 & -Y_{\dot r} \\
-L_{\dot u} & -L_{\dot w} & -L_{\dot q} & 0 & -L_{\dot v} & 1-L_{\dot p} & 0 & \dfrac{-I_{xz}}{I_x} \\
0 & 0 & 0 & 0 & 0 & 0 & -1 & 0 \\
-N_{\dot u} & -N_{\dot w} & -N_{\dot q} & 0 & -N_{\dot v} & \dfrac{-I_{xz}}{I_z} & 0 & 1-N_{\dot r}
\end{bmatrix}$$

Figure 38. Aircraft Equations of Motion in Stability Axes for Small Perturbations from Straight-Line Flight with Zero Bank Angle.

128

VII.2. EIGENVALUES

The eigenvalues are summarized in Table XV and are discussed below.

The effects of cross-coupling on most eigenvalues are not large. For example, at 100 knots in level flight, only two modes are significantly changed when the cross-coupling derivatives are suppressed. This is illustrated by the excerpt from Table XI reproduced below.

S-58, 100 Knots Level Flight

Cross-Coupling	Eigenvalues					
Yes	$-.46 \pm 1.63j$,	-4.96,	$-.12$,	$-.47$,	-1.82,	$.12 \pm .33j$
No	$-.48 \pm 1.73j$,	-5.23,	$-.11$,	$-.32$,	-1.79,	$.22 \pm .34j$

As will be shown later, the fact that most eigenvalues are essentially unchanged by the cross-coupling derivatives does not mean that cross-coupling effects are unimportant.

For level flight, the eigenvalues change only slightly as forward speed is increased. The unstable phugoid mode and the degenerate short-period modes characteristic of hover remain remarkably unchanged with forward speed. This is contrary to the usual trend noted in Reference 34, where the phugoid becomes stable and the $1/T_{sp1}$, $1/T_{sp2}$ modes merge to form the conventional short-period.

The roll subsidence root remains roughly equal to L_p over the speed range 0 to 100 knots. The dutch roll mode is stable even at hover due to the N_v of the tail rotor as explained in Reference 38, page 15). The frequency increases from $\omega = 0.73$ to $\omega = 1.163$ rad/sec, and the damping ratio rises slightly from 0.098 to 0.131.

In descent, at the higher speeds there is not much change in the eigenvalues. By analogy to fixed-wing aircraft, in which the phugoid damping ratio is roughly proportional to (D/L), one would expect that ω_p would increase in descent. This does occur, but the effect is not large. Thus at 100 knots in level flight, $\zeta_p = -.172$, whereas at the same horizontal speed and 22.5 fps rate of descent, $\zeta_p = -.14$. At lower speeds a similar effect occurs. For 20 knots forward speed in level flight, $\zeta_p = -.111$; with the same horizontal speed and 22.5 fps rate of descent, $\zeta_p = -.057$.

The largest effect of descent on the eigenvalues occurs at very low forward speeds. In addition to the increased phugoid damping noted above, the degenerate short-period roots coalesce to form a heavily damped oscillatory pair.

129

TABLE XV. SIKORSKY S-58 EIGENVALUES WITH SIX DEGREES OF FREEDOM.

CASE	VTAS FPS	γ DEG	DUTCH ROLL MODE	ROLL-SPIRAL-SPEED-PITCH MODES				PHUGOID	REMARKS
				ROLL	SPIRAL-SPEED		PITCH		
RATE OF DESCENT = 0									
5	0	0	-.088 ± .49j	-4.49	-.266 +	.075j	-1.14	.093 +|− .367j	
6	33.8	0	-.146 ± .73j	-4.76	-.197 ∓	.385	-1.15	.061 ± .334j	
7	67.8	0	-.24 ± .985j	-5.08	-.141	-.479	-1.33	.085 ± .374j	
8	101.5	0	-.323 ± 1.23j	-5.15	-.118	-.577	-1.42	.058 ± .324j	
9	169.0	0	-.46 ± 1.63j	-4.96	-.117	-.466	-1.82	.121 ± .331j	
9-	169.0	0	-.475 ± 1.73j	-5.23	-.111	-.323	-1.79	.219 ± .336j	Uncoupled
RATE OF DESCENT = 7.5 FT/SEC									
10	7.5	-90.0	-.116 ± .466j	-4.56	-.256 ±	.103j	-1.11	.082 ± .376j	
11	33.8	-12.8	-.162 ± .712j	-4.88	-.185	-.381	-1.13	.048 ± .332j	
12	67.8	- 6.35	-.255 ± 1.003j	-5.24	-.127	-.589	-1.23	.035 ± .316j	
13	101.5	- 4.12	-.343 ± 1.205j	-5.29	-.107	-.579	-1.42	.044 ± .315j	
14	169.0	- 2.54	-.492 ± 1.6j	-5.05	-.108	-.455	-1.83	.11 ± .326j	
RATE OF DESCENT = 15 FT/SEC									
15	15.0	-90.0	-.147 ± .445j	-4.63	-.247 ±	.12j	-1.08	.069 ± .388j	
16	33.8	-26.4	-.179 ± .687j	-4.97	-.176	-.366	-1.103	.039 ± .334j	
17	67.8	-12.8	-.271 ± .95j	-5.4	-.115	-.603	-1.214	.023 ± .308j	
18	101.5	- 8.5	-.357 ± 1.18j	-5.44	-.098	-.58	-1.42	.031 ± .305j	
19	169.0	+ 5.1	-.518 ± 1.57j	-5.15	-.10	-.44	-1.84	.10 ± .319j	
RATE OF DESCENT = 22.5 FT/SEC									
2	22.5	-90.0	-.179 ± .42j	-4.68	-.245 ±	.129j	-1.05	.054 ± .4j	
4	22.5	-90.0	-.221 ± .439j	-3.5	-.254 ±	.133j	-.993	.069 ± .396j	
20	33.8	-41.8	-.196 ± .646j	-4.98	-.181	-.312	-1.07	.035 ± .34j	No Tip Loss
1	67.8	-18.5	-.283 ± .924j	-5.57	-.104	-.616	-1.2	.011 ± .3j	
3	67.8	-18.5	-.281 ± .925j	-4.66	-.107	-.744	-1.06	.015 ± .286j	
21	101.5	-12.8	-.467 ± 1.154j	-5.59	-.089	-.58	-1.52	.019 ± .292j	
22	169.0	- 7.65	-.529 ± 1.54j	-5.25	-.093	-.42	-1.86	.091 ± .31j	No Tip Loss

130

In summary, it appears that the variation of the eigenvalues both with horizontal speed and rate of descent is less than one might have expected. In part, this is due to the small and rather low aspect ratio tail surfaces of the S-58. These are extremely ineffective, in that M_w remains positive throughout the speed range 0-100 knots. A more effective tail would tend to produce "airplane" type modes, i.e., oscillatory short-period and stable phugoid, as speed is increased.

VII.3. CROSS-COUPLING EFFECTS

As noted above, only minor changes in the eigenvalues occurred when the cross-coupling derivatives were set to zero. This trend is shown on Table XV for 100 knots level flight, but has also been verified by some calculations (not published here) for descending flight and lower speeds with and without the coupling terms. From this, it might be inferred that cross-coupling effects are minor. Nothing could be further from the truth! Examination of the print-outs (Volume III) reveals strong cross-coupling at all flight conditions.

In this section we demonstrate lateral-longitudinal cross-coupling by three complementary approaches:

1. Calculation of transfer functions with and without the cross-coupling derivatives

2. Calculation of the residues of the partial fraction expansion of the Laplace transform of the time response to a given input, such as a step or impulse in B_{1s}, or θ_o.

3. Study of the eigenvectors (the ratios of which equal the ratios of the residues in each degree of freedom for a given eigenvalue).

We show that the cross-coupling between longitudinal and lateral motions is strong for many of the modes. Furthermore, the cross-coupling occurs at all forward speeds and rates of descent examined here. In this respect the S-58 is believed to be representative of single-rotor helicopters in general. Little change occurs in the lateral-longitudinal cross-coupling for each mode as descent angle is increased at a given forward speed. Hence, the explanation of the difficulties encountered in flight path control in steep descent must be elsewhere. In the final section of this chapter, the culprit is identified as a nonminimum phase* γ/θ_o transfer function. This transfer function is crucial in flight path control at low speeds, and it is shown that in descent a nonminimum phase zero appears which causes a marked deterioration in the achievable level of accuracy with which the desired approach path can be followed.

---

*A nonminimum phase transfer function has one or more right-half plane zeros. The terms 'nonminimum phase zero' and 'right-half plane zero' are synonymous.

Effect of Cross-Coupling Derivatives on the Transfer Functions

For brevity, transfer functions will not be written in the usual form; e.g.,

$$\frac{\text{Output}(s)}{\text{Input}(s)} = \frac{(\text{Root locus gain}) \; \prod_{r=1}^{r=n} (s + z_r)}{\prod_{i=1}^{i=m} (s + p_i)}$$

Instead, we adopt the equivalent notation

$$\frac{\text{Output}}{\text{Input}} = \frac{(\text{Root locus gain}) \; \prod_{r=1}^{r=n} (-z_r)}{\prod_{i=1}^{i=m} (-p_i)}$$

For example, the transfer function

$$\frac{w(s)}{\theta_o(s)} = \frac{154.4 \; (s + 0.802) \; (s - 0.32)}{(s + 0.312)(s - 0.0354 + 0.34j)(s - 0.0354 - 0.34j)}$$

is written as

$$\frac{w}{\theta_o} = \frac{154.4 \; (-0.802) \; (+ 0.32)}{(-0.312)(+ 0.0354 \pm 0.34j)}$$

In this abbreviated style, right-half-plane poles and zeros are indicated by numbers with positive real parts.

As noted in Table XV, the 100-knot, level-flight case was run twice. Firstly, all the derivatives calculated from MOSTAB were included. Secondly, all derivatives coupling longitudinal forces or moments with lateral perturbations and vice versa were dropped. In addition, all lateral forces and moments produced by θ_o and B_{1s} were put equal to zero, as were all longitudinal forces and moments produced by θ_{oTR} and A_{1s}.

The results are compared in Table XVI.

TABLE XVI. EFFECT OF CROSS-COUPLING DERIVATIVES;
SIKORSKY S-58, 100 KNOTS, LEVEL FLIGHT

Cross Coupling	Pitch Rate/B_{1s} Transfer Function
No	$$\frac{8.43(-0.657)(-0.029)(0)}{(-0.33)(-1.79)(0.219 \pm 0.336j)}$$
Yes	$$\frac{8.48(0.017)(-0.061)(-0.109)(-5.25)(-0.46 \pm 1.69j)(-0.66)}{(0.117)(-4.96)(-0.466)(0.12 \pm 0.33j)(-0.46 \pm 1.63j)(-1.82)}$$

With approximate pole-zero cancellations removed, this becomes:

Yes	$$\frac{8.48(0.017)(-0.061)(-0.66)}{(-0.466)(-1.82)(0.12 \pm 0.33j)}$$

- -

Cross Coupling	Roll Rate/A_{1s} Transfer Function
No	$$\frac{-59.0(0.0000017)(-0.60 + 1.64j)}{(-0.11)(-5.23)(-0.476 \pm 1.73j)}$$
Yes	$$\frac{-58.9(0.000053)(-0.58 + 1.69j)(0.234 \pm 0.328j)(-1.86)(-0.31)}{(-0.117)(-4.96)(-0.466)(0.12 \pm 0.33j)(-0.46 \pm 1.63j)(-1.82)}$$

With approximate pole-zero cancellations removed, this becomes:

Yes	$$\frac{-58.9(0)(-0.577 \pm 1.69j)(-0.311)}{(-0.117)(-4.96)(-0.46 \pm 1.63j)(-0.466)}$$

133

Table XVI shows that the q/B_{1s} transfer function and the p/A_{1s} transfer function are hardly changed by the presence or omission of cross-coupling terms. Of course, if the cross-coupling terms are omitted, then the p/B_{1s} and q/A_{1s} transfer functions will be zero. This would be a serious error. To see just how serious, consider the p/B_{1s} and q/A_{1s} transfer functions. These are listed in Table XVII.

**TABLE XVII. CROSS-COUPLED TRANSFER FUNCTIONS;
SIKORSKY S-58, 100 KNOTS, S. L., LEVEL FLIGHT**

$$\frac{q}{A_{1s}} = \frac{-0.906(-30.27)(-0.56 \pm 1.67j)(0.077)(-0.67)(-0.086 \pm 0.95j)}{(-0.117)(-4.96)(-0.466)(0.12 \pm 0.33j)(-0.46 \pm 1.63j \quad -1.824)}$$

$$\frac{p}{B_{1s}} = \frac{0.048(0.093)(597.2)\ (-0.11 \pm 1.83j)(0.000012)\ (1.94)\ (-1.37)}{(-0.117)(-4.96)(-0.466)(0.12 \pm 0.33j)(-0.46 \pm 1.63j)(-1.824)}$$

Expanded in partial fractions

$$\frac{p}{B_{1s}} = \frac{0.061}{s + 0.117} - \frac{6.99}{s + 4.96} + \frac{4.91}{s + 0.466} + \frac{1.82 \angle 24.4^{\circ}}{s - 0.12 - 0.33j}$$

$$\frac{+1.82 \angle -24.4^{\circ}}{s - 0.12 + 0.33j} + \frac{1.63 \angle 96.9^{\circ}}{s + 0.46 - 1.63j} + \frac{1.63 \angle 96.9^{\circ}}{s + 0.46 + 1.63j} - \frac{0.96}{s + 1.824}$$

It is not easy to assess the relative magnitude of the pitch versus the roll motions produced by B_{1s} by comparing the transfer functions as listed in Tables XVI and XVII. A more direct comparison is obtained by expanding the q/B_{1s} and p/B_{1s} transfer functions into partial fractions and comparing the magnitude of each coefficient in the expansion, i.e., each residue, as shown in the lower half of Table XVII. Table XVIII shows such a comparison. For compactness, some numbers have been rounded off in Table XVIII, and only the residue corresponding to the upper-half plane root of each complex pair is shown.

TABLE XVIII. CROSS-COUPLING EFFECTS ON B_{1s} IMPULSE INPUT; SIKORSKY S-58 AT 100 KNOTS, SEA LEVEL					
Level Flight			7.65 Deg. Descent		
Root	Residues		Root	Residues	
s, rad/sec	p	q	s, rad/sec	p	q
- .117	.061	.0033	- .0926	- .0062	- .797
-4.96	-6.99	.7245	-5.25	-5.59	.469
- .466	4.91	- .622	- .421	6.16	- .797
.121 + .33j	1.82 ∠24°	1.2 ∠-152°	.091 + .31j	2.39 ∠19°	1.18 ∠-147°
- .46 + 1.63j	1.63 ∠97°	.264 ∠24°	- .541 + 1.54j	3.14 ∠107°	.511 ∠29°
-1.824	- .955	-6.942	-1.865	-2.37	-6.851

Table XVII shows p and q residues for B_{1s} inputs at two flight conditions. To form a complete picture of cross-coupling, u, v, w, and r must also be considered. However, Table XVII suffices to demonstrate that, in level flight at 100 knots, B_{1s} induces considerable roll (compared to pitch) and that this cross-coupling is not much changed by descent.

To understand Table XVIII, first compare the relative magnitudes of the residues for each mode. The relative importance of p to q in each mode depends upon the ratio of the residues. For example, Table XVIII shows that the rapidly decaying s = 4.96 mode is predominantly roll. On the other hand, the unstable oscillatory mode displays almost as much pitch as roll, and the s = -1.824 mode has about seven times as much pitch rate as roll rate.

The above remarks indicate the relative magnitude of pitch and roll in each mode, but this information, by itself, is insufficient to predict the cross-coupling induced by the pitch control, B_{1s}. To determine that, we must scrutinize the absolute magnitude of each of the q residues. If the residues of the "pitch" modes (s = 0.12 ± 0.33j, s = -1.824) are very much larger than the residues of the other "coupled" or "roll" modes, then the response will be dominated by pitch, and B_{1s} will induce little cross-coupling. Examining Table XVIII leads to the conclusion that although the residues of the "pitch" modes are somewhat larger than those of the other modes, the difference in magnitude is not so overwhelming that we can say that the roll induced by B_{1s} is small. We therefore conclude that B_{1s} induces appreciable roll in level flight at 100 knots.

The descent situation is summarized by the right-hand side of Table XVIII. Overall, there is very little change in the residues between level flight and descent at 100 knots. If this result is representative, it implies that the difficulties in control in steep approaches due to cross-coupling are no worse than those encountered in level flight. Hence, we cannot ascribe the difficulties experienced in following steep glide slopes to changes in cross-coupling between level flight and descent.

To verify that the above result is representative, we have calculated the residues for u, v, w, p, q, r, to A_{1s}, B_{1s}, θ_o, θ_{oTR} for a wide range of flight conditions.

Table XIX illustrates a typical comparison between level flight and two descending cases, all at 40 knots airspeed. This confirms the conclusions of Table XVIII that descent angle has only a minor influence on cross-coupling. From examination of the residues for the entire range of flight conditions presented here (0 to 100 knots airspeed, and zero to 22.5 fps rate of descent), the effect of descent angle is quite small. We therefore conclude that variations in cross-coupling between level flight and descent are not a major source of difficulty in controlling steep approach paths on single-rotor helicopters.

Before leaving the subject of cross-coupling, it should be noted that, although the effect of descent rate is small, cross-coupling varies significantly with airspeed. This can be seen by examining the transfer functions presented in Volume III . It is usual to reduce the effects of cross-coupling by suitable phasing of A_{1c} and B_{1c} to B_{1s}, through offset of the servos. This correction can be exact only at a single flight condition.

TABLE XIX. EFFECT OF DESCENT ON CROSS-COUPLING
SIKORSKY S-58 AT 40 KNOTS T.A.S. SEA LEVEL.

	ROOTS			q RESIDUES TO B_{1s}			p RESIDUES TO B_{1s}		
	$\gamma = 0$	$\gamma = -6.4°$	$\gamma = -19.4°$	$\gamma = 0$	$\gamma = -6.4°$	$\gamma = -19.4°$	$\gamma = 0$	$\gamma = -6.4°$	$\gamma = -19.4°$
	$-.14$	$-.127$	$-.104$	-0.8×10^{-5}	$-.0067$	$-.0058$	-0.9×10^{-4}	$-.045$	$.124$
	-5.078	-5.24	-5.56	$.351$	$.258$	$.097$	-4.17	-3.31	-1.44
	-0.479	-0.589	-0.616	$-.226$	$.34$	$.447$	2.73	3.67	1.29
	$.085 +.37j$	$.035 +.316j$	$.011 +.298j$	$1.2 \angle -135°$	$.99 \angle -119°$	$.94 \angle -110°$	$1.24 \angle 52°$	$1.16 \angle 66°$	$1.05 \angle 58°$
	$-.24 +.99j$	$-.255 +.97j$	$-.28 +.924j$	$0.15 \angle 71°$	$.26 \angle 90.9°$	$.395 \angle 95°$	$0.54 \angle 147°$	$0.88 \angle 163.4°$	$1.39 \angle -172°$
	-1.33	-1.23	-1.198	-6.045	-7.10	-7.11	2.45	2.64	4.89

The effect of descent angle on the transfer function relating flight path angle, γ, to collective pitch is most significant. The difference between level flight and steep descent cases for this transfer function is such that control at low speeds is seriously degraded in descent. As explained below, the effect is caused by a right-half plane zero. It appears that this zero is the primary cause of the control difficulties experienced in steep descent.

It is first necessary to define the quantities of importance in precise flight path control for slow, steep approaches.

The key quantity determining how accurately a given approach flight path is followed is, in general, not height, nor flight path angle, but the displacement of the helicopter from the desired approach path. This quantity is illustrated in Figure 39. For brevity we shall call it "height error", denoted by the symbol $\hat{h}$.

This section:

(1)   defines $\hat{h}$ in terms of w and q (for which transfer functions have been calculated)

(2)   presents transfer functions relating $\hat{h}$ to collective pitch

(3)   demonstrates that, at low speeds, control of $\hat{h}$ by collective pitch is relatively easy in level flight but difficult in steep descents

(4)   traces the reason for the difficulty to a nonminimum phase zero in the $\hat{h}/\theta_o$ transfer function

(5)   investigates methods for alleviating the difficulty through typical stability augmenter systems

Definition of Height Error, $\hat{h}$

Consider Figure 39. This indicates the distance of the helicopter c.g. from the desired flight path. Call this distance the "height error" $\hat{h}$.

Using stability axis quantities,

$$\frac{d\hat{h}}{dt} = U_O \int q \, dt - w$$

Note that this expression neglects products of small-perturbation quantities, and also products of small-perturbation quantities with the small trim bank angle ϕ_o which is typically of the order of 1 degree.

138
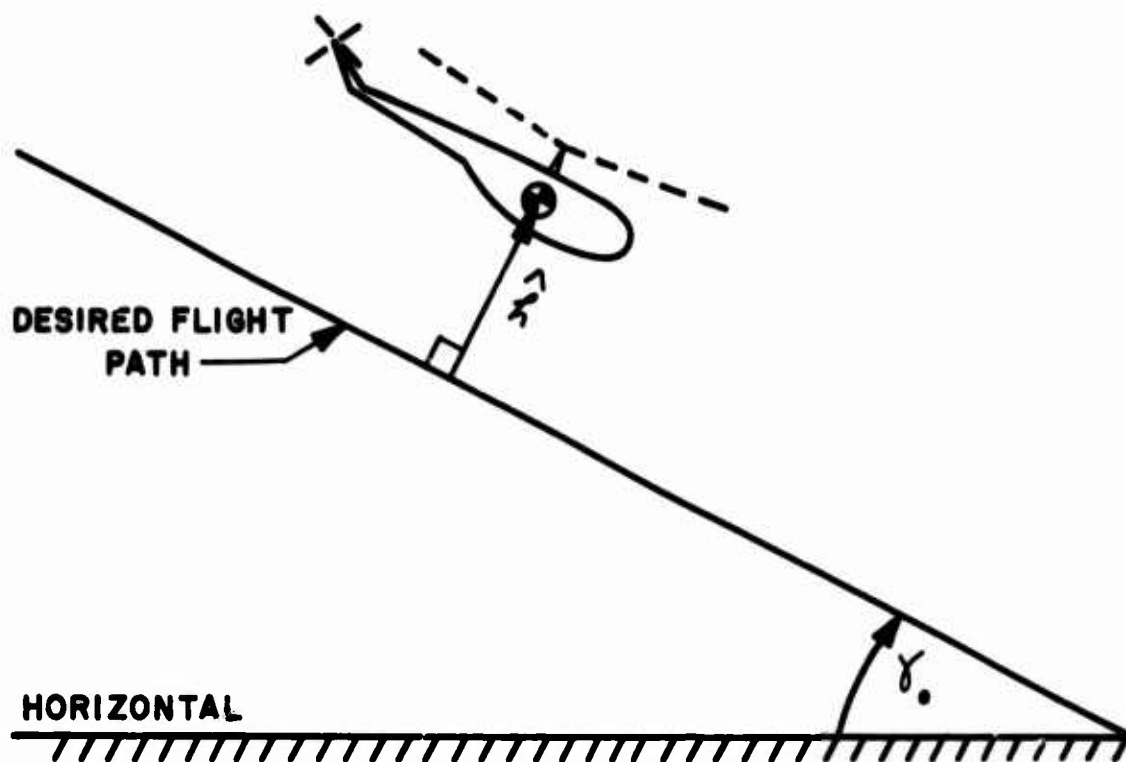
Figure 39. Definition of Height Error, $\hat{h}$.

The flight path angle perturbation, with the same assumptions, becomes

$$\gamma = \frac{\hat{h}}{\int (U_o + u)dt}$$

For vertical and almost-vertical descents the above expressions are not appropriate. Vertical descents are usually made close to the ground and the key parameter is the height above the ground. Using stability axes, in vertical descent this parameter is given by

$$h = \int (U_o + u)dt$$

Transfer Functions for $\hat{h}$ to Collective Pitch

Volume III does not give the h numerators directly, but these can be constructed from the q/s and w transfer functions. The results are displayed in Table XX.

As will be shown, the significant feature to note in Table XX is the right-half plane zero. At 20 knots (Cases 6, 11, and 20), this zero increases with descent angle. This trend is reversed at the higher speeds, but this reversal is not relevant to height-control because above about 40 knots B_{1s} becomes more effective than θ_o in controlling height. However at low speeds $\hat{h} = \int (U_o qdt - wdt)$ is dominated by the w term and cannot effectively be controlled by cyclic pitch. The $\hat{h}/\theta_o$ transfer function is thus of prime importance, at low speeds.

Height Error Response to Collective Input

Figure 40 shows the time histories of the responses to a unit collective pitch input for the S-58 at 20 knots (1) in level flight and (2) in a steep descent ($\gamma_o = -41.8$ deg). Note that, in the descending case, the height error goes the "wrong way" after about 8 seconds, never returning to the "right" direction. By contrast, for level flight during the first 30 seconds the height error moves only a little way in the wrong direction, between 17 and 22 seconds after the step input.

Both responses are oscillatory. This is due to the unstable phugoid mode. As shown later, this oscillatory mode can be stabilized by standard feedback of pitch rate to longitudinal cyclic. Considering the remaining modes in Figure 40, there is a fundamental similarity between the responses, in that both ultimately go in the wrong direction.* This is characteristic of the step response of a system with one nonminimum phase zero. It can be proved (from the Laplace transform initial and final value theorems) that for such a system,

---
* This is shown by the partial fractions listed on page 143.

TABLE XX. SIKORSKY S-58 NUMERATORS FOR COLLECTIVE CONTROL OF NORMAL DISTANCE FROM UNPERTURBED FLIGHT PATH $\hat{h}/$, θ_o.

Case	V_{TAS} fps	γ_o Deg	Root Locus Gain	Numerator Root Locations (rad/sec)					
				LEVEL FLIGHT					
5	1.0	0*	236.1	-.087 ± .50j	-4.48	0	-.159	-1.15	.091 ± .37 j
6	33.8	0*	227.5	-.073 ± .72j	-4.74	.078	-.22	-1.05	-.0435 ± .263j
7	67.8	0*	249.7	-.139 ± .896j	-5.08	.056	-.252	-.796	-.173 ± .356j
8	101.5	0*	276.2	-.064 ± 1.18j	-5.19	.043	(-.795 ± .736j)		-.121 ± .093j
9	169	0*	318.8	-.121 ± 1.54j	-5.13	.035	(-.89 ± 1.5 j)		-.113 ± .071j
				7.5 fps RATE OF DESCENT					
10	7.5	-90*	235.9	-.115 ± .474j	-4.57	0	-.18	-1.11	.082 ± .379j
11	33.8	-12.8	214.7	-.108 ± .725j	-4.87	.1143	-.247	-1.05	-.029 ± .172j
12	67.8	-6.35	243.8	-.157 ± .918j	-5.24	.054	(-.64 ± .385j)		-.103 ± .129j
13	101.5	-4.12	274.6	-.616 ± 1.31j	-5.34	.029	(-.278 ± .836j)		-.109 ± .079j
14	169.	-2.54	154.4						
				22.5 fps RATE OF DESCENT					
2	22.5	-90*	238.5	-.181 ± .435j	-4.69	0	-.227	-1.05	.054 ± .402j
20	33.8	-41.8	154.4	-.164 ± .711j	-4.0	.268	-.256	-1.11	-.04 ± .0923j
1	67.8	-18.5	223.9	-.221 ± .891j	-5.58	.036	(-.701 ± .334j)		-.015 ± .038j
21	101.5	-12.8	267.5	-.275 ± 1.08j	-5.64	-.062	(-.723 ± .786j)		-.013 ± .04j
22	169.	-7.65	319	-.244 ± 1.46j	-5.42	.0039	(-.916 ± 1.46j)		-.068 ± .028j

* For perturbations from level flight, $\hat{h}$ = height. For vertical descent, $\hat{h}$ is defined as vertical distance from the unperturbed position.
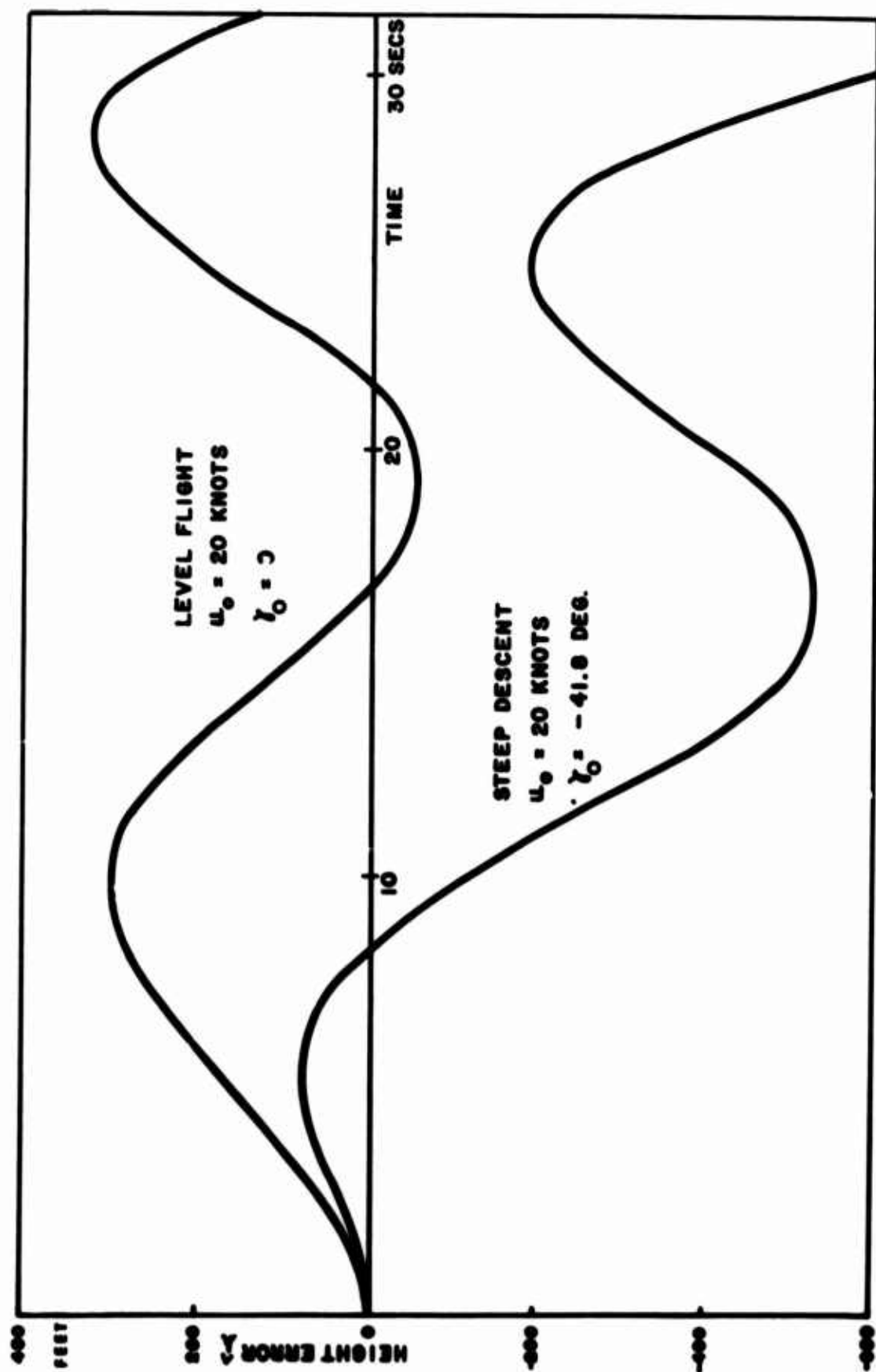
141

Figure 40. Sikorsky S-58: 20 Knots, S.L. Time History of Height Error (Perpendicular Distance From Unperturbed Flight Path) Due to + 0.1 Radian Step Input Increase in Collective Pitch.

142

the sign of the initial slope of the step response is different from
the sign of the final value of the response.

The difference between the responses of Figure 40 lies in the
rapidity with which they move in the wrong direction, and it is this
factor which causes difficulty of control. To demonstrate this, form
the unit step response time history by expanding the Laplace transform
of $1/s$ times the transfer function, and taking the inverse transform
of each partial fraction. This yields, per radian of increased collective,

Level Flight:

$$\hat{h} = -670 + 377.2t -13.6t^2 + 869e^{-0.385t} +465e^{-0.197t}$$
$$-675e^{0.06t} (\cos 0.33t -0.28 \sin 0.33t)$$
$$+0.038e^{-4.76t} +21.7e^{-1.15t} -28e^{-0.146t}(\cos 0.73t -2.4 \sin 0.73t)$$

Steep Descent

$$h = -1,298 +7.1t -9.94t^2 +568e^{-0.385t} +1,496e^{-0.18t}$$
$$-812e^{.035t} (\cos 0.34t -1.5 \sin 0.34t)$$
$$-0.031 e^{-4.98t} -6.9e^{-1.07t} +53e^{-0.196t}(\cos 0.65t +1.72 \sin 0.65t)$$

Figures 41 and 42 show how the above components sum to form the complete
response. The $\hat{h}/\theta_o$ transfer function has two poles at the origin (see
Figure 43, or Tables XX and XV); hence, the step input yields partial
fractions involving $1/s^3$, $1/s^2$, and $1/s$, corresponding to parabolic, ramp,
and constant components of the step response time history. These
components are primarily responsible for the differences between the
responses for level flight and descent. The components depend on the
vector distances from the poles at the origin to other uncancelled poles
and zeros, and are markedly affected by the change in the right half plane
zero from $s = 0.074$ for level flight to $s = 0.268$ for steep descent.

Closed-Loop Control of Height Error

The adverse effect of the shift in the nonminimum phase zero from
0.078 rad/sec for level flight to 0.268 rad/sec for $\gamma_o = -41.8$ degrees
can be demonstrated by constructing a root locus. The simplest feed-
back to consider is a "pure gain" feedback of $\hat{h}$ to collective. This is
illustrated on Figure 43, which shows the $\gamma = -41.8$-degree case.
Note that even at low gains, a root moves close to the zero at $s = 0.268$.
For example, for a feedback gain, $\theta_o/\hat{h}$, of 0.08 radian per 100-foot
height error, the system is unstable with a root at $s = 0.13$, i.e.,
doubling amplitude every 5.3 seconds. This divergence is too rapid
to be acceptable.

For level flight, the zero is still present but is reduced in
magnitude from $s = 0.268$ sec^{-1} to $s = 0.078$ sec^{-1}. For the same gain
as used in descent ($\theta_o/\hat{h} = 0.08/100$ radian per foot); the closed-loop
time constant is approximately 0.057; hence the time to double
amplitude is increased to 12 seconds.

143

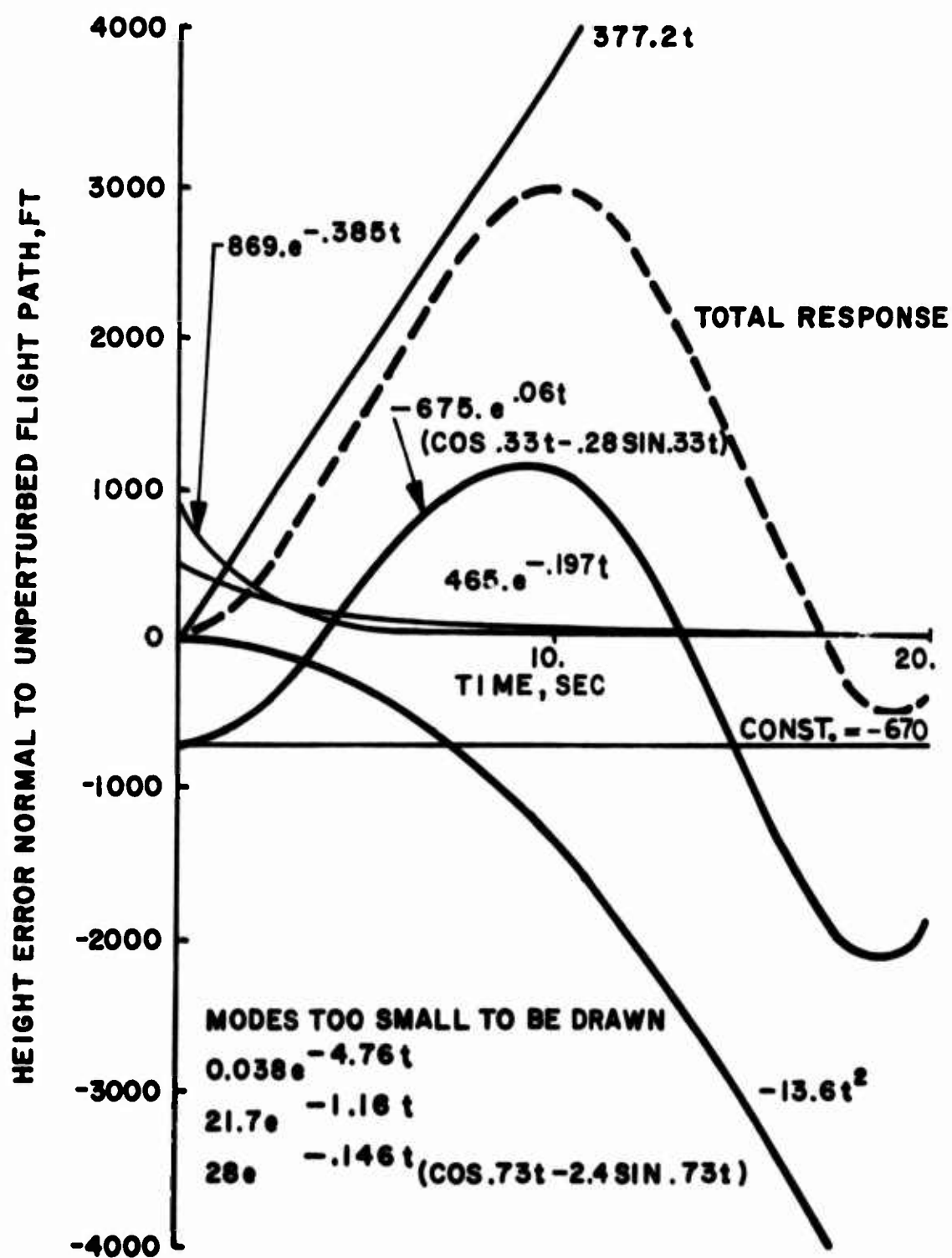Figure 41. Sikorsky S-58, Level Flight, 20 Knots, S. L.
Components of Height Error Time History per 1.0
Radian Step Increase in Collective Pitch.
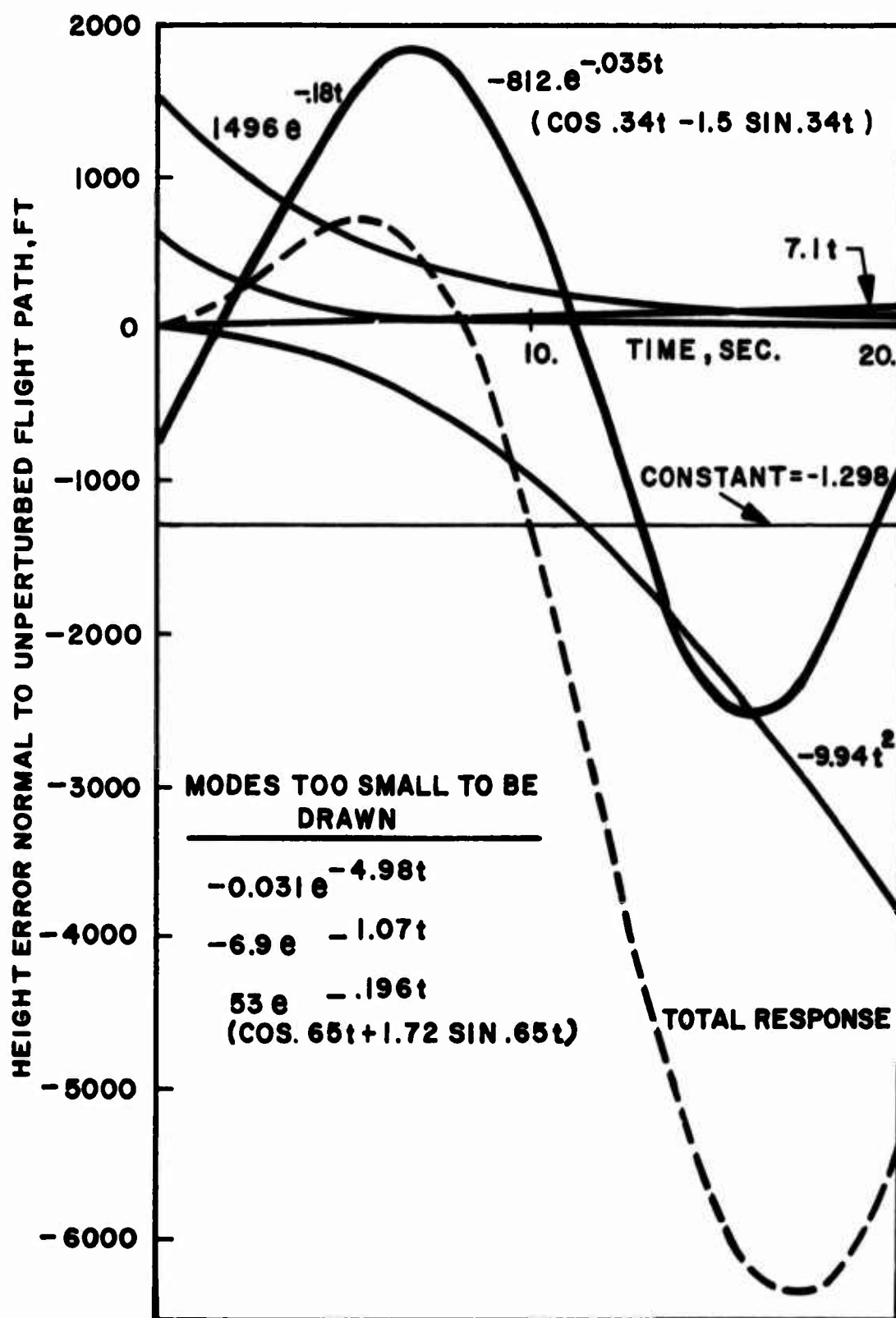
Figure 42. Sikorsky S-58: 20 Knots, S.L. Steep Descent
γ = - 41.8 Degrees Components of Height Error
Time History per 1.0 Radian Step Increase in
Collective Pitch.

145
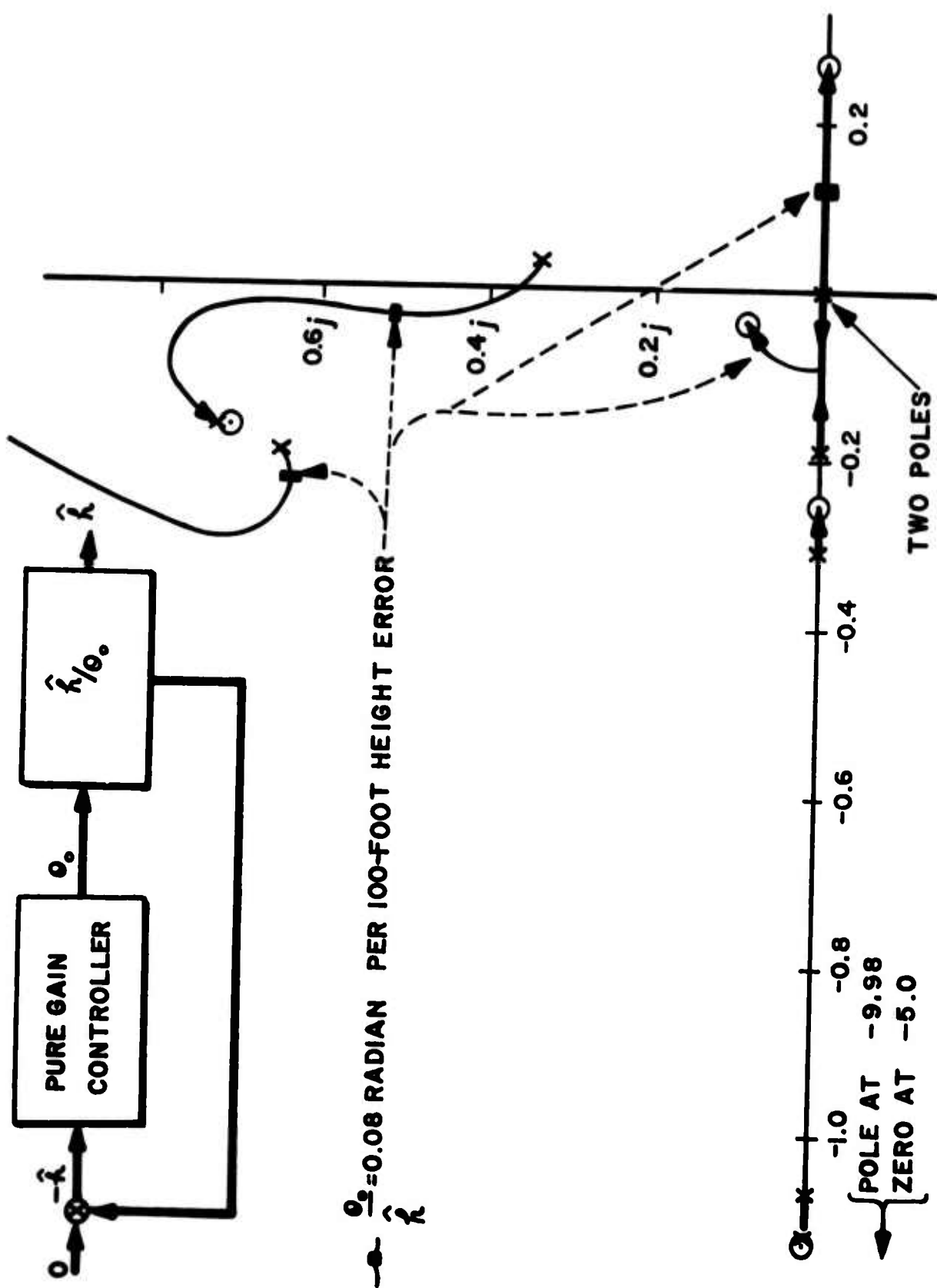
Figure 43. Sikorsky S-58: Height Error/Collective Root Locus
$U_o = 20$ Knots $\gamma = -41.8$ Deg.

Of course, the "pure gain" closure discussed above is the simplest form of control, and the instability can be cured by more complicated compensation, plus "wrong-way" gain (i.e., increasing collective to compensate for being above the desired flight path). However, little can be done to alter the position of the nonminimum phase zero, which (as shown below) is the basic cause of the unsatisfactory tracking capability.

The reason why the zero is so tenacious is that, at low speeds, collective pitch is the only effective way of controlling height error. This can be seen by going to the limit, i.e., hover, when cyclic pitch produces essentially no Z-force. Thus there is no real possibility for multiloop control of height error. (In passing, note that this possibility does exist on the AH-56A discussed in the next chapter because the propeller pitch can effectively control the flight path.) Whatever feedbacks are employed, the overall transfer function relating height error to collective retains the nonminimum phase zero.

Summarizing the above discussions: the $\hat{h}/\theta_o$ right-half plane zero is objectionable because:

(1)   It causes the initial step response to be in the opposite direction to the final response.

(2)   It makes it difficult to obtain a stable closure of the $\hat{h} \rightarrow \theta_o$ loop.

(3)   It cannot be moved appreciably by closing other loops (e.g., $\hat{h} \rightarrow B_{1s}$) unless excessively high gains are used.

Granted all the above points, some further explanation is still required. This is because right-half plane zeros are quite common in aircraft transfer functions but do not normally cause a major deterioration in handling qualities. For example, the height-to-elevator transfer function of a conventional aircraft flying above its minimum drag speed contains a "far-out" right-half plane zero. However, neither "far-out" or "very close-in" zeros cause a significant deterioration in the step response. What, then, is so bad about the S-58 $\hat{h}/\theta_o$

transfer function at 20 knots, $\gamma = 41.8$ degrees, and the associated step response shown on Figure 40?

The answer can be found rigorously by considering the effects of the relative magnitude of the nonminimum phase zero and the gust break frequency on the performance of an optimal regulator. This is done in Reference 39, but the essential point can be grasped by the following reasoning.

Consider the task of a pilot flying a helicopter in a gusty environment, approximated by a series of randomly spaced square wave w-gusts of random amplitude. Let the average time between successive gusts be τ_g seconds. Suppose, the helicopter has a stable step response to collective which is "up" for τ_h sec and "down" thereafter (i.e., a nonminimum phase characteristic). If τ_g is very much less than τ_h, the optimal control requires negative feedback, i.e., reduced collective pitch, to counter an up-gust. On the other hand, if the gusts are very widely spread, the integrated absolute value of the perturbation from the desired flight path is minimized by positive feedback. Between these two cases a condition exists where the optimal policy is zero feedback. At this condition, there is nothing that the pilot (or S.A.S.) can do to improve the accuracy with which the helicopter is following the desired flight path. In such circumstances the pilot will regard the helicopter's handling qualities as unsatisfactory.

It can be shown (Reference 39) that with a single nonminimum phase zero located at $s_2 = n$ rad/sec, and standard gust power spectrum of the form $\Phi_{ww} = K/(s^2 + \omega_b^2)$, the above condition occurs when $n = \omega_b$, i.e., when the zero is of equal magnitude to the input break frequency. For hover and low-speed flight, ω_b is normally assumed to be $\doteq 0.3$ rad/sec (see Appendix VIII). Hence, the zero located at $s = + 0.268$, as predicted for the $\gamma_o = - 41.8$-degree case, will adversely affect handling qualities.

Strictly, the above discussion applies only to single-loop control. However, at low speeds, control of $\hat{h}$ is virtually limited to collective pitch, so this restriction is realistic. A zero cannot be moved provided only one control is used. Hence, no cure is possible through stability augmentation in the collective loop.

Effect of Stability Augmentation

For simplicity, the foregoing analysis has considered only the unaugmented helicopter. The effect of stability augmentation on the nonminimum phase zero is not large, as explained above; however, some benefit is obtained, since there is a limited effect of cyclic pitch on $\hat{h}$. This is illustrated by Table XXI, which shows the effect of a typical S.A.S. feedback on the poles and zeros. With a feedback gain just adequate to stabilize the phugoid, the h/θ_o zero remains about the same magnitude as in the unaugmented case. The time histories (see Figure 44) show similar objectionable "wrong-way" characteristics to the unaugmented case (Figure 40); the stability augmentation merely damps the phugoid.

TABLE XXI. EIGENVALUES AND HEIGHT ERROR NUMERATORS FOR THE S-58 WITH $q \to B_{1s}$ STABILITY AUGMENTATION GIVING TOTAL Mq EQUAL TO FOUR TIMES THAT OF THE UNAUGMENTED AIRCRAFT.

Case	Rate of Descent	γ Deg.	Root Locus Gain	Dutch Roll	Roll Subsidence, Spiral, and Short-Period Modes				Phugoid
20 KNOTS. EIGENVALUES									
6	0.	0		-.132 ± .724j	-4.31	-.211	-.354	-3.57	-.0001 ± .198j
20	-22.5	-41.8		-.193 ± .64j	-4.77	-.234 + .093j		-3.4	-.0026 ± .193j
w/θ₀ NUMERATORS									
6	0	0	-227.5	-.1207 ± .702j	-4.08	.0048		-3.6	-.064 ± .143j
20	-22.5	-41.8	-154.4	-.209 ± .647j	-4.73	.236		-3.36	-.14 ± .138j
(q/s)/θ₀ NUMERATORS									
6	0	0	1.06	-.16 ± 1.35j	-3.5	.1721	-.411		-.114 ± .178j
20	-22.5	-41.8	.742	-.155 ± 1.14j	-3.96	.1715	-.381		-.108 ± .159j
ĥ/θ₀ HEIGHT ERROR NUMERATORS									
6	0	0	227.5	-.101 ± .735j	-4.25	.094	-.123	-3.58	-.069 ± .168j
20	-22.5	-41.8	154.5	-.191 ± .667j	-4.82	.225	-.0319	-3.42	-.137 ± .131j
40 KNOTS, EIGENVALUES									
7	0	0		-.246 ± 1.003j	-4.84	-.141	-.508	-3.49	.0087 ± .228j
1	-22.5	-19.4		-.314 ± .962j	-5.49	-.106	-.582	-3.72	-.0088 ± .116j
w/θ₀ NUMERATORS									
7	0	0	-250.	-.266 ± .924j	-4.94	-.112		-2.65	.01 ± .234j
1	-22.5	-19.4	-224.	-.336 ± .935j	-5.65	-.1005		-2.79	.1021 -.156
(q/s)θ₀ NUMERATORS									
7	0	0	1.85	-.164 ± 1.34j	-5.16	.1288	-.473		-.089 ± .133j
1	-22.5	-19.4	2.22	-.228 ± 1.08j	-6.03	.0193	-.605		-.049 ± .204j
ĥ/θ₀ HEIGHT ERROR NUMERATORS									
7	0	0	250.	-.196 ± .984j	-4.88	.0564	-.18	-3.22	-.053 + .207j
1	-22.5	-19.4	224	-.293 ± .945j	-5.53	.0321	-.224	-3.5	-.016 + .031j
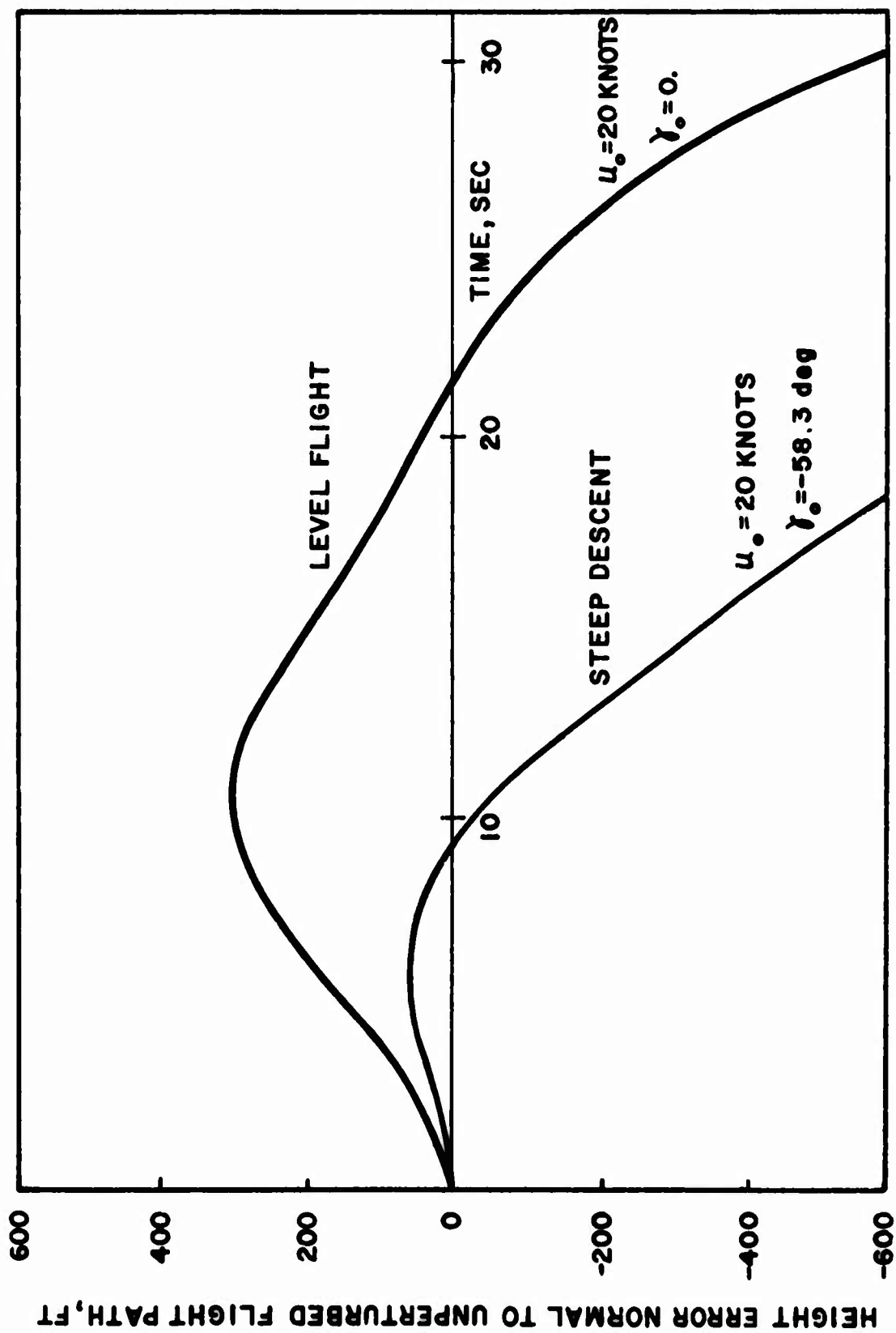
Figure 44. Sikorsky S-58: 20 Knots Airspeed, S.L. Stability Augmented by Pitch Rate Feedback to B_{1s}, Giving Total Pitch Damping Equal to Four Times That of the Unaugmented Airframe. Response to 0.1 Rad Step Increase in Collective Pitch.

At higher speeds, e.g., 40 knots, cyclic pitch has more effect on the flight path, so $q \to B_{1s}$ feedback is effective in reducing the wrong-way characteristic.

Summary

For single-rotor helicopters, as typified by the S-58, the effects of longitudinal-lateral cross-coupling on the eigenvalues are relatively small. However the cross-coupling is large, as shown by the eigenvectors and such transfer functions as p/B_{1s} and q/A_{1s}. Except at very low speeds, the variation of the eigenvalues with rate of descent is small. The cross-coupling also changes little between level flight and the upper boundary of the vortex-ring state.

The major reason why control is degraded in steep descents is shown by the transfer function relating collective pitch to the distance of the helicopter from the unperturbed flight path. This transfer function contains a right-half plane zero which cannot easily be removed by multiloop feedbacks. The effect of the zero is to cause the step response to collective pitch to be largely in the wrong direction when performing steep descents at low speeds.

Because of the large number of derivatives involved in the coupled longitudinal-plus-lateral equations of motion, it has not yet been possible to identify the significant derivatives causing the nonminimum phase zero. The question arises as to whether this is some special peculiarity of the S-58 or whether it is indeed representative of single-rotor helicopters in general. Conclusive proof will require a more general analysis; however, in the next chapter it is shown that the same nonminimum phase effect occurs on the AH-56A. It is therefore probable that the effect is typical of single-rotor helicopters.

CHAPTER VIII. COMPOUND HELICOPTER DYNAMICS

VIII.1 INTRODUCTION

This section discusses the open-loop and closed-loop dynamics of a typical compound helicopter. The principal features which differentiate such vehicles from "single-rotor" helicopters are the wing and the auxiliary thrusting device, which may be a jet engine or a propeller. Both these features are intended to unload the rotor at high speeds. One might expect, therefore, that at low speeds, there would be few significant differences between the dynamics of the "single-rotor" and "compound" configurations. This proves to be the case; the eigenvalues and eigenvectors display similar variations with forward speed and descent angle for both types of helicopters. For this reason frequent reference will be made to the preceding discussion of single-rotor helicopter dynamics, and Chapter VII should be read before this chapter.

The example vehicle chosen to represent compound helicopters is the Lockheed AH-56A. As originally flown, this helicopter incorporated an all-mechanical stability augmenter system (the "gyro"). Difficulties were experienced in flight as a result of coupling between the gyro and blade modes other than the first flapping mode. At the time of writing, alternative S.A.S. schemes are under consideration, and for our purposes, it appears logical to consider the basic AH-56A with gyro removed. The resulting configuration should be more representative of the dynamics of compound helicopters in general than the AH-56A with gyro, and the data presented here are thus suitable for preliminary design of S.A.S. systems and for prediction of handling qualities.

The detailed AH-56A data presented in Volume IV is similar to that previously discussed for the S-58. That is, it includes derivatives and transfer functions relating u, v, w, p, q, r to A_{1s}, B_{1s}, θ_o, θ_{oTR}, θ_{op} (collective pitch of the pusher propeller). Residues and eigenvectors were also calculated and are quoted in this chapter where appropriate, but they are not listed in Appendix VII.

The above information is presented for the AH-56A at sea level, with true airspeeds of 0, 20, 40, 60, and 100 knots. For each speed, descent rates of 0, 9.6, 19.2, 28.8 fps are considered. At low speeds, the highest descent rate is almost at the boundary of the vortex-ring state.

Two cases were re-run with the cyclically varying tip loss factor set to zero. This caused noticeable shifts in the eigenvalues but no radical change in the general nature of the vehicle response. That is, modes which were stable with tip losses included remained stable with B=1, and the residues were of the same order of magnitude with and without tip losses. For example, at 40 knots and 28.8 fps descent rate (γ = -25.1 deg), the eigenvalues changed as indicated below.

AH-56A 40 Knots, Steep Descent, γ = -25.1 Deg

TIP LOSS	EIGENVALUES, rad/sec					
INCLUDED	-.233 + .758j,	-9.9,	-.063,	-.526,	-1.89,	-.041 + .26j,
OMITTED	-.234 + .76j,	-8.36,	-.064,	-.603,	-1.51,	-.036 ± .257

The above changes are rather less than might be expected by considering the effect of tip losses on the derivatives. The explanation is that the magnitudes of some derivatives (e.g., Z_w) are decreased by the tip loss, whereas others (e.g., M_q, L_p) are increased in magnitude because tip loss gives increased flapping. In all the cases discussed below, tip losses were included.

VIII.2 EIGENVALUES

Table XXII summarizes the AH-56A eigenvalues. In level flight, the eigenvalues are generally similar to those calculated for the S-58, at the corresponding speeds. The major differences are

(1) The AH-56A roll subsidence root is about twice as large as that of the S-58, due to the increase in "effective hinge offset" of the hingeless rotor.

(2) The AH-56A develops longitudinal static stability at lower speeds than the S-58. This is due to the negative M_w contributions of the tail and the pusher propeller. The result is that the phugoid is stable at speeds above 50 knots, approximately. In addition, the short-period degenerate modes combine to form an oscillatory mode at 100 knots.

In descent, the eigenvalues generally do not change significantly from their values in level flight at the same airspeed. The exceptions to this statement are noted below.

At the higher speeds, descent increases the phugoid damping and causes some reduction in frequency. This would be expected from the increase in $|X_u|$. At 100 knots and the most rapid descent rate (which corresponds to γ = - 9.8 deg) this trend progresses so far that the phugoid degenerates into a pair of aperiodic roots. One

153

TABLE XXII. LOCKHEED AH-56A EIGENVALUES.

Case	V_{DAS} ft/sec	γ Deg.	Dutch Roll Mode	Roll-Spiral-Speed-Pitch				Phugoid	Remarks
5	0	0	-.018 ± .594j	-10.	-.205		-2.01	.055 ± .415j	
6	33.8	0	-.115 ± .584j	-9.94	-.111		-2.02	.009 ± .562j	
7	67.8	0	-.24 ± .816j	-9.82	-.072	-6.12	-2.07	.052 ± .38j	Level
8	101.5	0	-.281 ± 1.06j	-10.51	-.052	-.934	-1.88	-.056 ± .258j	Flight
9	169.0	0	-.401 ± 1.51j	-10.6	-.057	(-1.58 ± .556j)		-.041 ± .188j	
10	9.6	-90.0	-.057 ± .581j	-9.94	(.206 ± .062j)		-1.98j	.016 ± .424j	9.6 f.p.s.
11	33.8	-16.5	-.134 ± .567j	-9.84	-.105	-.28	-1.95	-.024 ± .526j	Rate of
12	67.8	-8.05	-.222 ± .796j	-10.25	-.064	-.70	-1.902	-.057 ± .265j	Descent
13	101.5	-5.41	-.292 ± 1.06j	-10.26	-.05	-.948	-1.82	-.056 ± .226j	
14	169.0	-3.25	-.414 ± 1.51j	-10.25	-.052	(-1.55 ± .582j)		-.059 ± .141j	
15	19.2	-90.0	-.059 ± .572j	-9.88	(-.19 ± .082j)		-1.94	-.01 ± .451j	19.2 f.p.s.
16	33.8	-35.5	-.149 ± .556j	-9.78	-.148	-.253	-1.92	-.024 ± .35j	Rate of
17	67.8	-16.5	-.266 ± .782j	-10.06	-.05	-.38	-1.98	-.052 ± .169j	Descent
18	101.5	-10.9	-.305 ± 1.05j	-9.98	-.044	-.962	-1.76	-.053 ± .185j	
19	169.	-6.52	-.426 ± 1.50j	-9.78	.0079	(-1.52 ± .586j)		-.05 ± .258j	
2	28.8	-90.0	-.08 ± .562j	-9.82	(-.181 ± .091j)		-1.91	-.039 ± .459j	28.8 f.p.s.
4	28.8	-90.0	-.09 ± .586j	-7.73	(-.20 ± .085j)		-1.45	-.025 ± .471j	No Tip Loss
20	33.8	-58.3	-.155 ± .478j	-9.78	(-.17 ± .10j)		-1.9	-.033 ± .368j	Rate of
1	67.8	-25.1	-.253 ± .758j	-9.9	-.063	-.526	-1.89	-.041 ± .262j	Descent
3	67.8	-25.1	-.254 ± .76j	-8.36	-.064	-.605	-1.51	-.056 ± .257j	
21	101.5	-16.6	-.507 ± 1.027j	-9.7	-.057	+.25	-2.16	-.27 ± .198j	
22	169.	-9.81	-.451 ± 1.49j	-9.56	-.025	(-1.5 ± .98j)		-.129 .0755	No Tip Loss

of these roots is slightly unstable at $s = 0.073$. This "tuck" mode instability is caused by the change in M_u that occurs between 60 and 100 knots at 28.8 fps descent rate. (At 60 knots, $M_u = +0.336 \times 10^{-4}$ rad/sec^2; at 100 knots, $M_u = -17.6 \times 10^{-4}$ rad/sec^2.)

Apart from this phugoid change, the only other significant effect of descent on the eigenvalues occurs at vertical and near-vertical descents. For such conditions, two modes, which at hover are aperiodic, coalesce to form a well-damped low-frequency oscillation. The eigenvectors (discussed later) indicate that this behavior is due to N_w. This derivative, referred to body axes, increases by a factor of approximately 30 going from hover to the maximum vertical descent rate at the boundary of the vortex-ring state. This marked change occurs because the tail rotor thrust becomes more sensitive to perturbations in vertical velocity as the rate of descent is increased. A similar effect was noted on the S-58.

VIII.3 CROSS-COUPLING EFFECTS

As with the single-rotor helicopter, lateral-longitudinal cross-coupling is severe. This is illustrated by Table XXIII which presents AH-56A eigenvectors at hover. Note that u, v, w, p, q, r, are referred to stability axes which, in hover, are arbitrarily defined such that the x-axis is horizontal and the y-axis is normal to the plane of the symmetry of the fuselage, which is almost but not exactly vertical. (The print-out gives the stability axis Euler angles in radians for each flight condition.) In Table XXIII the choice of the unit eigenvector varies arbitrarily from mode to mode. As in Table XVII, only the upper-half plane root of each complex pair is shown.

Examination of Table XXIII reveals the dominant degrees of freedom of each mode, and the names of each mode are chosen accordingly. However, with the exception of the roll subsidence, each mode displays strong lateral-longitudinal coupling, so the names should not be taken too literally. The resemblance of each mode to the corresponding uncoupled mode is not necessarily close.

155

TABLE XXIII. AH-56A EIGENVECTORS AT HOVER.							
(u, v, w, p, q, r, in stability axes)							
s	u	v	w	100p	100q	100r	Mode Name
-.235	.39	.014	1.0	.00067	-.039	.569	" Plunge"
-.205	.107	.829	1.0	.0058	-.102	1.85	" Yaw "
.035 +.415j	1.0	-.106 +.322j	-.00001 +.024j	.015 -.175j	.518 -.117j	.231 +.417j	"Phugoid"
-.018 +.394j	-.713 -.077j	1.0	.0135 +.043j	-.48 +.009j	-.394 -.0967j	.681 -1.27j	" Dutch Roll"
-10.0	.022	.6327	-.0185	100.0	6.3	-1.93	"Roll Subsi -dence"
-2.01	1.0	-.245	.053	-2.02	-10.56	-24.2	"Speed -Pitch"

TABLE XXIV. AH-56A EIGENVECTORS IN 28.8 fps VERTICAL DESCENT.							
Body Axis Rates / s	u	v	w	100p	100q	100r	Mode Name
-.181 +.091j	.391 -.348j	-.099 +.147j	1.0	.0213 +.0472j	.00135 +.0076j	1.32 -4.38j	"Coupled Plunge- -Yaw"
-.039 +.439j	-1.0	.057 -.187j	-.0225 -.0248j	-.0081 +.107j	-.57 -.119j	.237 +.166j	"Phugoid"
-.08 +.362j	-.449 .229j	1.0	-.06 -.092j	-.446 +.0197j	-.204 -.089j	-.717 +1.48j	"Dutch Roll"
-9.8	-.079	1.0	.012	-4.4	-2.85	-.824	"Roll Subsi- dence"
-1.91	-1.0	.171	.0045	4.5	-21.8	+.77	"Speed- Pitch"
Stability Axis Rates	-w	v	u	100r	100q	-100p	

The cross-coupling hardly changes with descent rate, provided that u, v, w, p, q, r are referred to body axes rather than stability axes. This point is important for very steep descents. For example, in vertical descent the body x-axis and the stability x-axis differ by 90 degrees. This must be considered when comparing Table XXIII with Table XXIV, its counterpart for 28.8 fps vertical descent.

At the foot of Table XXIV are listed the stability axis quantities corresponding to the body axis quantities at the head of the table. Thus, for example, to trace the effect of vertical descent on the "dutch roll" mode, note that, at hover, the ratio of $|u|:|v|:|w|$ is approximately $0.72:1.0:0.045$. For vertical descent the corresponding ratio in body axes is $0.5:1.0:0.10$. By comparing the eigenvectors in this fashion, it is seen that there is not much difference between the hover and descent modes with the exception of the plunge and yaw modes which couple together in vertical descent. This is caused by the increased sensitivity of the tail rotor to perturbations in vertical descent velocity. The tail rotor is not immersed in the main rotor wash at hover and in vertical descent. At hover, by symmetry, the tail rotor thrust is equally sensitive to "up" and "down" w perturbations; hence, its contribution to the cross-coupling derivative N_w is negligible. However, as the descent rate increases, the unperturbed flow conditions at the tail rotor become asymmetric, and the derivative N_w increases markedly, causing the "yaw" and the "plunge" modes to couple.

Cross-coupling is pronounced at forward speed. For example, the short-period oscillatory mode, $s = -1.58 \pm 0.556j$, which emerges at 100 knots involves about one-third as much roll as pitch. This is illustrated by Table XXV, which presents some typical residues for pitch and roll response to B_{1s}. Table XXV shows that the cross-coupling does not change much with shallow angles of descent.

The pitch rate/B_{1s} transfer function also changes rather little from level flight to steep descent, as shown by Figure 45. Numerous near-cancellations occur, leaving essentially a second-order numerator and a third-order denominator.

TABLE XXV. EFFECT OF DESCENT ON CROSS-COUPLING; LOCKHEED AH-56A AT 100 KNOTS, SEA LEVEL, NO S.A.S.					
Roots		-q Residues to B_{1s}		-p Residues to B_{1s}	
$\gamma = 0$	$\gamma = -9.8°$	$\gamma = 0$	$\gamma = -9.8°$	$\gamma = 0$	$\gamma = -9.8°$
-.401 +1.51j	-.431 +1.49j	.035 < -152.8°	.034 < -128.9°	.429 < -137.5°	.36 < -173.0°
-10.6	-9.56	1.90	1.526	36.4	32.95
-.037	-.025	.104	-.0079	.0777	.00317
-1.58 +.556j	-1.50 +.58j	13.7 < -130.6°	11.7 < -135.8°	5.52 < -105.0°	3.61 < -110.8°
-.041 +.188j	-.129	.56 < -89.6°	-.517	.537 < +98.6°	.265
	.0733		-.287		-.322

As noted previously, the AH-56A has a large roll subsidence root, (typically about 10 rad/sec), due to the hingeless rotor. This is well separated from the other roots, which should lead to little coupling with other modes in the p/A_{1s} transfer function. This is confirmed by Figure 46, which shows the transfer functions for p/A_{1s} at 100 knots in level flight and 22.8 fps descent. Note that only the roll subsidence pole is not cancelled by a nearby zero.

The above trends are typical. For ease of reference, Table XXVI has been extracted from the data of Appendix VII to show the effect of descent angle on the ϕ/A_{1s} and θ/B_{1s} numerators at various forward speeds. From this table and Table XXV, it is evident that the effect of descent angle on pitch and roll control is small. Similar comments apply to yaw control by tail rotor collective (see Table XXVII). Table XXVII shows that the yaw/θ_{oTR} numerators change little with descent angle, provided that the yaw is referred to body axes (i.e., overall vehicle axes) rather than stability axes.
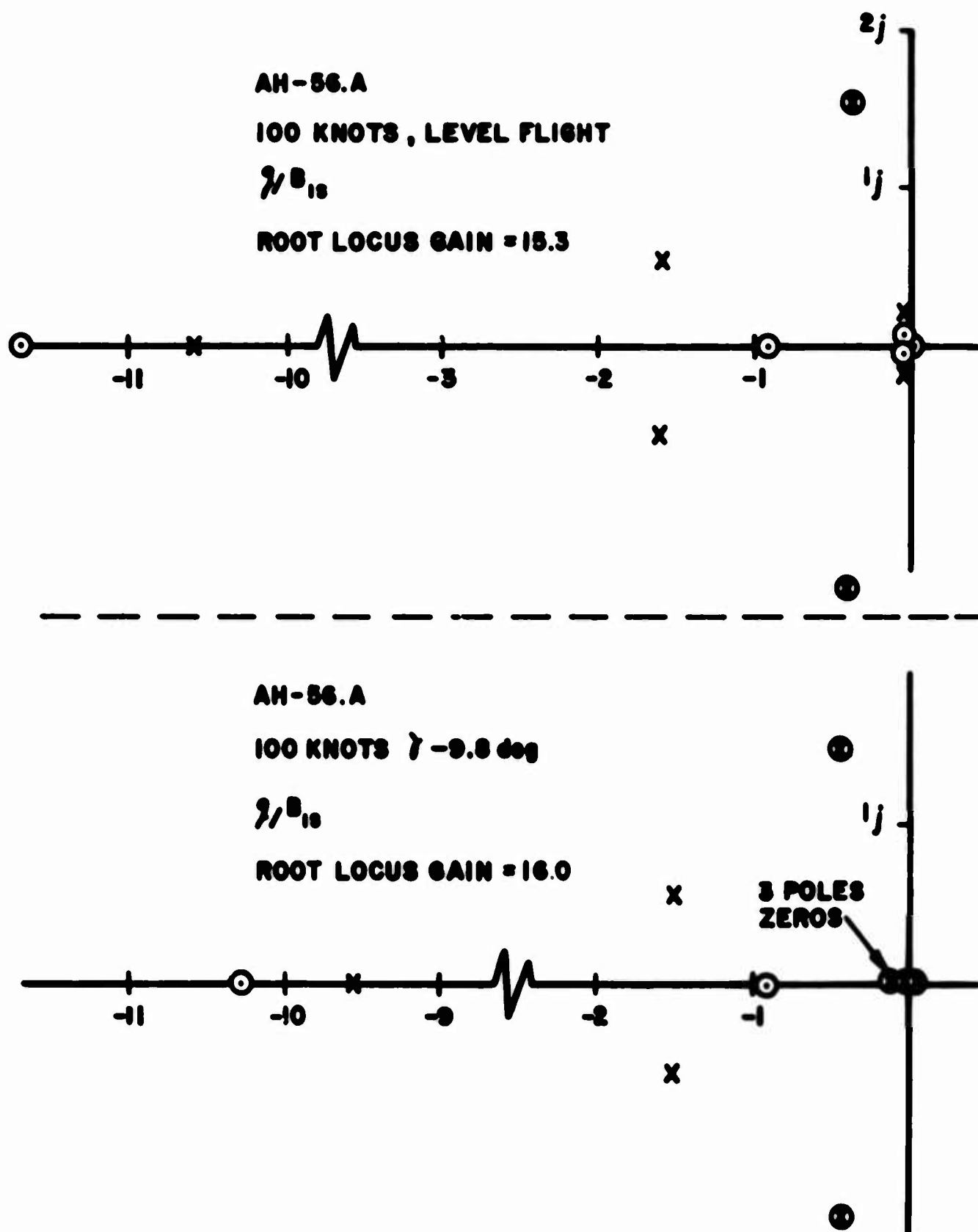
Figure 45. Compound Helicopter Pitch Rate/Longidutinal Cyclic Transfer Function for Level Flight and for a 9.8-Degree Descent Angle at Sea Level.
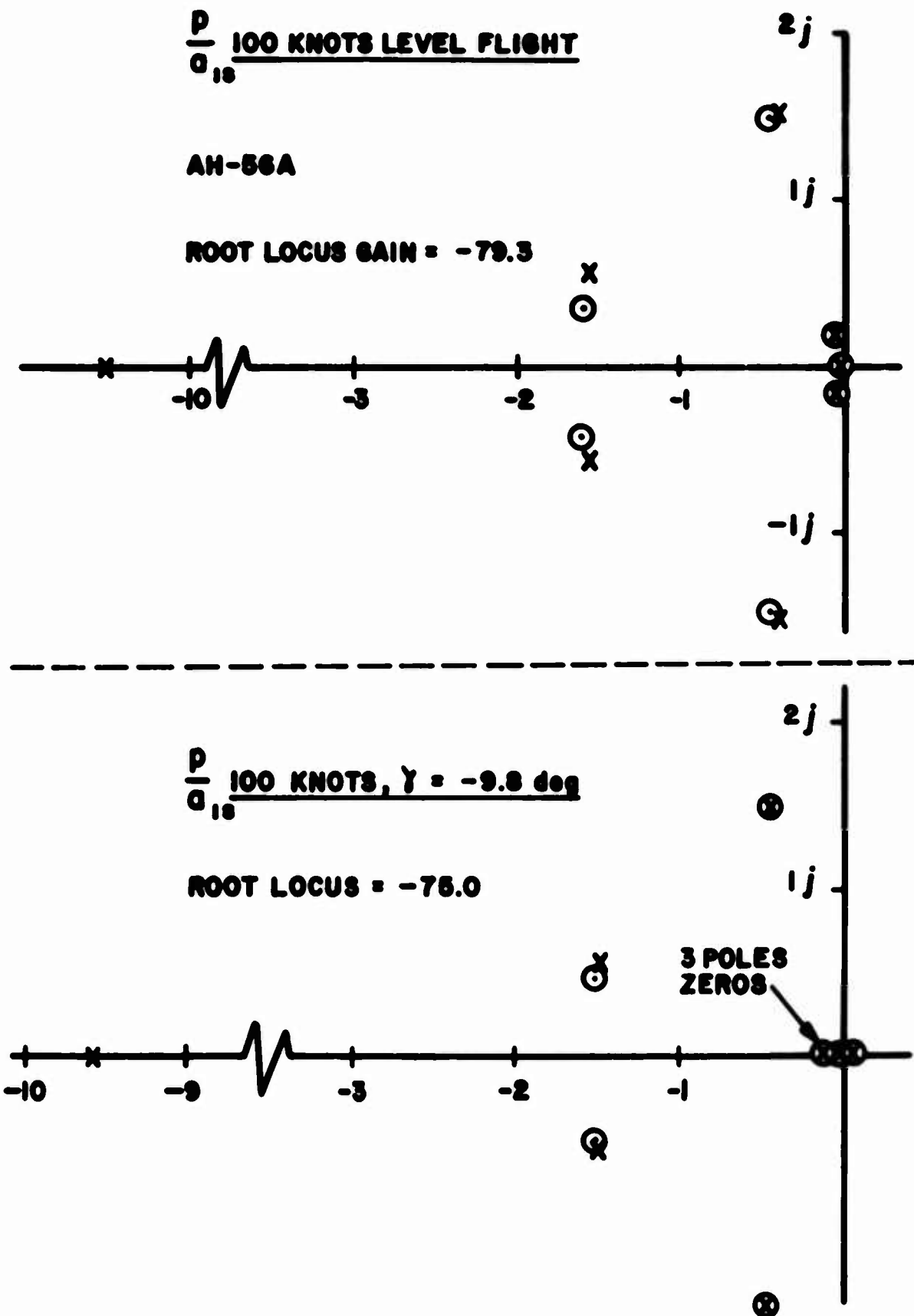
Figure 46. Compound Helicopter Roll Rate/Lateral Cyclic
Transfer Functions for Level Flight and 9.8-Degree
Descent at Sea Level.

TABLE XXVI. LOCKHEED AH-56A, No S.A.S.; TRANSFER FUNCTION
NUMERATOR COEFFICIENTS FOR φ/A₁ₛ AND θ/B₁ₛ

Case	V TAS Ft/Sec	γ Deg	Root Locus Gain	Numerator Root Locations			

φ/A₁ₛ Numerators, Rate of Descent = 0.0

Case	V TAS Ft/Sec	γ Deg	Root Locus Gain				
5	0	0	-79.76	- .231 ± .007j	- .032	-2.07	-.038 ± .409j
6	33.8	0	-79.61	- .208 ± .451j	- .397	-2.09	-.043 ± .367j
7	67.8	0	-79.46	- .269 ± .727j	- .58	-2.14	-.051 ± .398j
8	101.5	0	-79.46	- .334 ± 1.00j	- .845	-2.01	-.03 ± .28j
9	169.	0	-79.26	- .454 ± 1.48j	(-1.603 ± .363j)		-.038 ± .207j

Rate of Descent = 28.8 Ft/Sec

Case	V TAS Ft/Sec	γ Deg	Root Locus Gain				
2	28.8	-90.	1.854	2.43 - .916	- .141	(-2.64 ± .336j)	-.038 ± .435j
20	33.8	-58.3	-38.78	.165 ± .756j	- .191	-1.99	-.037 ± .376j
1	67.8	-25.1	-69.82	.111 ± .728j	- .212	-1.94	-.046 ± .276j
21	101.5	-16.6	-73.27	.262 ± 1.00j	(- .258 ± .203j)	-2.21	.245 -.092
22	169.	- 9.81	-75.01	.428 ± 1.47j	.025	(-1.52 ± .473j)	.059 -.12

θ/B₁ₛ Numerators, Rate of Descent = 0.0

Case	V TAS Ft/Sec	γ Deg	Root Locus Gain				
5	0	0	13.68	- .034 ± .408j	(- .237 ± .025j)	-11.4	.03 ± .095j
6	33.8	0	13.68	- .115 ± .58j	.072	-11.3	-.119 ± .082j
7	67.8	0	13.7	- .206 ± .808j	.048	-11.2	-.052 ± .009j
8	101.5	0	14.4	- .283 ± 1.06j	.012	-11.8	-.068 ± .026j
9	169.	0	16.0	- .404 ± 1.51j	.013	-11.6	-.064 ± .024j

Rate of Descent = 28.8 Ft/Sec

Case	V TAS Ft/Sec	γ Deg	Root Locus Gain				
2	28.8	-90.	13.27	- .096 ± .358j	(- .169 ± .107j)	-11.3	.013 ± .01j
20	33.8	-58.3	13.29	- .151 ± .475j	(- .208 ± .142j)	-11.3	.038 ± .097j
1	67.8	-25.1	13.4	- .234 ± .75j	.536	-11.2	-.022 -.077
21	101.5	-16.6	13.69	- .312 ± 1.02j	.62	-10.8	-.031 -.05
22	169.	- 9.81	15.31	- .432 ± 1.49j	.93	-10.3	-.036 -.062

161

TABLE XXVII. LOCKHEED AH-56A YAW/TAIL ROTOR COLLECTIVE NUMERATORS

Case	V_{TAS} fps	γ Deg.	Root Locus Gain	Numerator Zeros				
				r/θ_{OTR} NUMERATORS, RATE OF DESCENT = 0.0				
5	0	0	-5.12	.049 ± .41j	-9.97	-.248	-2.01	-.002 ± .405j
6	33.8	0	-4.55	.02 ± .384j	-9.91	-.413	-2.02	-.011 ± .38j
7	67.8	0	-4.23	.036 ± .388j	-9.79	-.626	-2.06	-.015 ± .365j
8	101.5	0	-5.14	-.019 ± .339j	-10.51	-.955	-1.87	-.057 ± .263j
9	169.	0	-6.95	-.038 ± .326j	-10.68	(-1.59 ± .577j)		-.041 ± .19j
				RATE OF DESCENT = 28.8 FT/SEC. BODY AXIS AT θ = 0 DEGREE				
2	28.8	-90.	-4.43	-.05 ± .436j	-9.78	-.1518	-1.903	-.065 ± .381j
20	33.8	-58.3	-4.3	-.057 ± .364j	-9.7	-.225	-1.9	0 ± .40j
1	67.8	-25.1	-3.78	-.049 ± .295j	-9.92	-.544	-1.89	-.043 ± .267j
21	101.5	-16.6	-4.96	-.274 ± .197j	-9.76	+.25	-2.15	-.053 ± .257j
22	169.	-9.81	-6.85	-1.505 ± .60j	-9.73	+.071	-.13	-.063 ± .222j

VIII.4 HEIGHT CONTROL

As with the S-58 (discussed in the previous chapter), it is
anticipated that the AH-56A will experience difficulty in flight path
control in slow, steep descents. This can be inferred from Table XXVIII,
which presents numerators for the transfer function relating height
error to collective pitch. (See Figure 39 for the definition of
"height error", h.) Table XXVIII shows that, at the lower speeds and
steeper descent angles a nonminimum phase zero appears at $0.1 < s < 0.6$
rad/sec. As shown in Chapter VII, such a zero degrades the handling
qualities. Typical effects of this zero are shown in the step responses
of Figure 47, which display awkward "wrong-way" characteristics for
the descending flight conditions.

The difficulties of removing this right-half plane zero by
feedbacks to cyclic pitch, explained in Chapter VII for the S-58, apply
equally to the AH-56A. However, the AH-56A does have the extra possibility
of flight path control through the pusher propeller, as described below.

Control Effectiveness of the Pusher Propeller

Assuming that the aircraft is trimmed so that the pusher propeller
is not operating in the vortex-ring state (a condition which is satisfied
for the flight conditions presented in this report), the principal
effects of θ_{op} relate to control of u and h. The appropriate numerators
for level flight and steep descent are summarized in Table XXIX.
Completing the transfer functions with the denominators given in Table
XXII permits some preliminary assessment of the effectiveness of the
pusher propeller as a control device.

At 100 knots in level flight, many approximate cancellations
occur between numerator and denominator, leaving the following approximate
transfer function for speed control:

$$\frac{u}{\theta_{op}} \doteq \frac{-34.0}{(s - 0.073)}$$

This indicates that the pusher propeller controls speed by
exciting the unstable "tuck" mode of the degenerate phugoid pair. This
would be unsatisfactory for $x(= \int u \, dt)$ control (e.g., stationkeeping)
since the $x \rightarrow \theta_{op}$ locus lies entirely in the right half-plane. The
situation would be improved by stability augmentation involving feed-
backs of θ to B_{1s}, which would stabilize both phugoid roots. Descent
improves the u/θ_{op} transfer function: at 100 knots and $\gamma = -9.8$ degrees,
it becomes approximately

163

TABLE XXVIII. HEIGHT ERROR/COLLECTIVE NUMERATORS FOR THE AH-56A

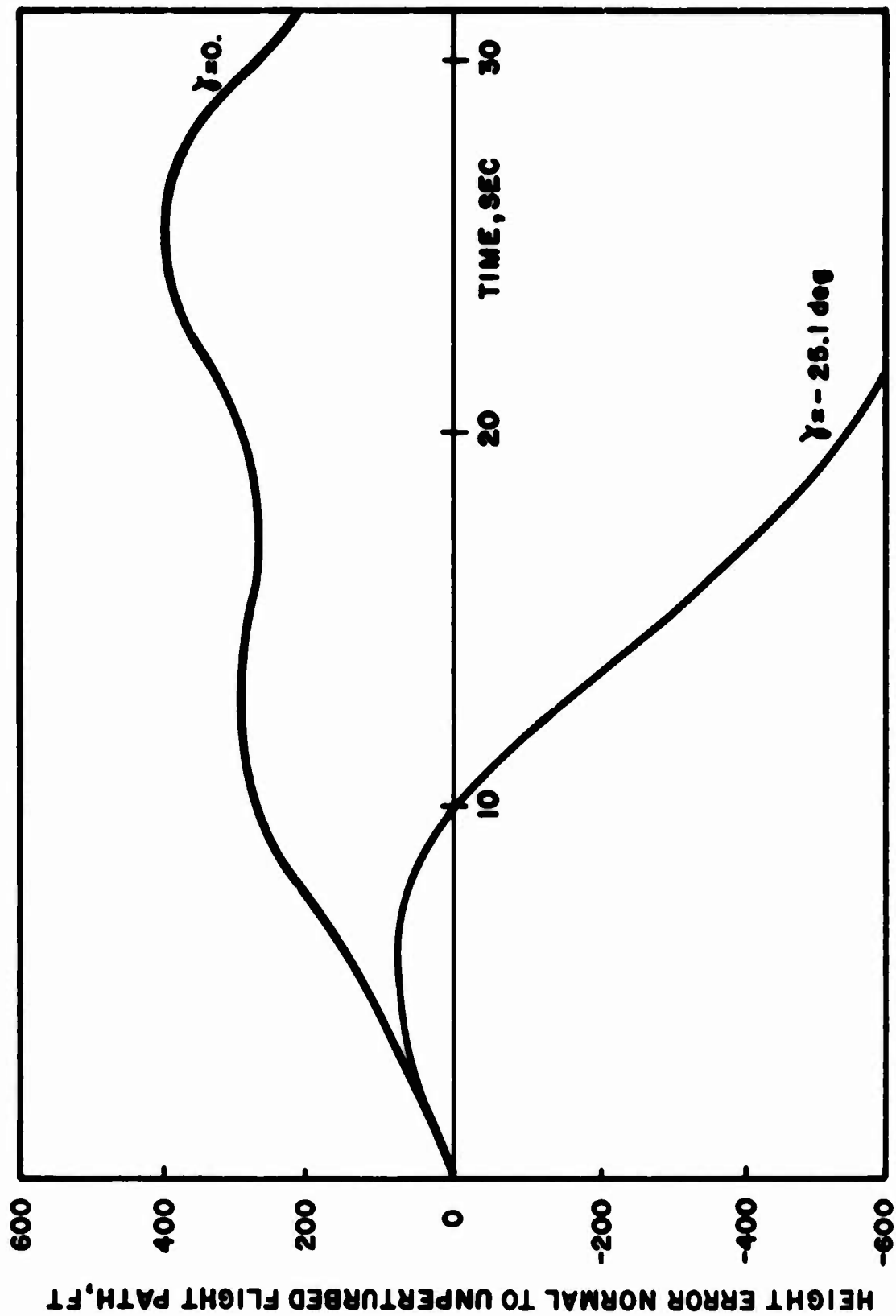| CASE	V_{TAS} FT/SEC	γ DEG	ROOT LOCUS GAIN	NUMERATOR ZEROS				
5	0	0	229.9	-.0197 ± .393j	-10.0		-.134 / -2.01	.033 ± .416j
6	33.8	0	218.4	-.122 ± .605j	-9.93	.0945	-.104 / -1.96	-.058 ± .343j
7	67.8	0	238.	-.203 ± .832j	-9.8	.0684	-.142 / -1.89	-.226 ± .238j
8	101.5	0	283.	-.286 ± 1.058j	-10.41	.0514	-.878 / -2.88	-.096 ± .048j
9	169.	0	336.	-.424 ± 1.52 j	-10.6	.0215	(-1.11 ± 2.25j)	-.074 ± .033j
10	9.6	-90	230	-.04 ± .382 j	-9.94	0	-.148 / -1.98	.017 ± .425j
11	33.8	-16.5	202.4	-.147 ± .571 j	-9.83	.132	-.058 / -1.93	-.071 ± .272j
12	67.8	-8.05	243.6	-.219 ± .81 j	-10.2	.057	-.561 / -1.49	-.107 ± .048j
13	101.5	-5.41	284.6	-.297 ± 1.07 j	-10.3	.027	(-1.09 ± .931j)	-.072 ± .038j
14	169.	-3.25	340.2	-.42 ± 1.5j	-10.18	.045	(-1.28 ± 2.1 j)	0.0 -.013
15	19.2	-90	251	-.062 ± .373j	-9.88	0	-.154 / -1.94	-.009 ± .433j
16	33.8	-33.5	170.	-.171 ± .539j	-9.77	.182	-.064 / -1.96	-.091 ± .259j
17	67.8	-16.45	257.	-.221 ± .789j	-10.	.126	-.016 / -1.68	-.091 -.342
18	101.5	-10.9	282.	-.309 ± 1.05j	-9.96	.051	(-1.05 ± .904j)	-.034 ± .016j
19	169.	-6.52	344.	-.438 ± 1.48j	-9.83	.023	(.276 ± 1.7j)	-.024 ± .021j
2	28.8	-90	253	-.084 ± .362j	-9.82	0	-.166 / -1.91	-.057 ± .44 j
20	33.8	-58.3	112.	-.195 ± .466j	-9.78	.248	-.08 / -1.97	-.105 ± .273j
1	67.8	-25.1	222.	-.231 ± .762j	-9.88	.106	-.011 / -1.71	-.082 -.56
21	101.5	-16.55	273.	-.305 ± 1.043j	-9.68	.189	-.851 / -1.12	0.0 -.057
22	169.	-9.81	345.5	-.436 ± 1.49j	-9.52	.0125	(-1.07 ± 2.17j)	-.027 ± .019j

164

Figure 47. Lockheed AH-56, 40 Knots Airspeed, S. L. Height Error Response to 0.1 Radian Step Increase in Collective Pitch.

165

$$\frac{u}{\theta_{op}} = \frac{-34.1\ (s + 0.095)}{(s + 0.04 \pm 0.188j)}$$

This provides stable $x \rightarrow \theta_{op}$ closures provided that excessive lags are avoided.

At lower speeds, fewer approximate cancellations occur. For example, at 40 knots in level flight,

$$\frac{u}{\theta_{op}} \doteq \frac{-18.2\ (s + 0.162 \pm 0.062j)}{(s - 0.072)\ (s + 2.07)\ (s + 0.032 \pm 0.38j)}$$

whereas at 40 knots in descent at $\gamma = -25.1$ degrees,

$$\frac{u}{\theta_{op}} \doteq \frac{-18.14\ (s + 0.174)\ (s - 0.057 \pm 0.312j)}{(s + 0.526)\ (s + 1.89)\ (s + 0.041 \pm 0.262j)}$$

The appearance of a nonminimum phase zero in descent is not important here because of the proximity of the phugoid mode, which will yield only a small residue and will largely cancel out the wrong-way characteristics of the step response.

Simultaneously with u-perturbations, θ_{op} also induces $\hat{h}$ perturbations; hence it is necessary to consider these also in assessing the control effectiveness of the pusher propeller. The appropriate transfer functions are given in Table XXIX; some rather gross cancellations have been made in the approximate transfer functions presented below in order to simplify the discussion.

$\gamma = 0$:

$$\frac{\hat{h}}{\theta_{op}} \doteq \frac{1.62\ (s + 0.475)\ (s - 0.349)\ (s - 43.52)}{s(s + 1.58 \pm 0.556j)\ (s + 0.041 \pm 0.188j)}$$

$\gamma = -9.8$ degrees

$$\frac{\hat{h}}{\theta_{op}} \doteq \frac{-3.15\ (s + 5.97)\ (s - 2.12)}{s(s - 0.073)\ (s + 1.5 \pm 0.58j)}$$

166

TABLE XXIX. PUSHER PROPELLER COLLECTIVE TRANSFER FUNCTION HEIGHT ERROR AND SPEED NUMERATORS FOR THE LOCKHEED AH-56A.

Case	V_{TAS} Ft/Sec	γ Deg.	Root Locus Gain	Numerator Zeros					
h/θ_{op} HEIGHT ERROR NUMERATOR									
5	0	0	-.1807	-.042 ± .493j	-10.	-.183	-2.65	-.076 ± .406j	
6	33.8	0	-.2044	-.101 ± .574j	-9.64	-.11	-16.56	-.694 ± .617j	
7	67.8	0	-.3615	-.18 ± .807j	-8.37	-.077	-15.3	.081 ± 1.145j	
8	101.5	0	.1066	-.281 ± 1.06j	-12.34	-.051	404.	.0105 ± .575j	
9	169.	0	1.62	-.408 ± 1.51j	-15.42	-.475	45.52	-.052,	.549
2	28.8	-90.	-10.5	-.084 ± .366j	-9.82	-.726	-1.32	-.115 ± .115j	
20	33.8	-58.3	-11.25	-.143 ± .474j	-9.78	-.60	-1.38	-.206 ± .05j	
1	67.8	-25.1	-8.6	-.279 ± .761j	-9.95	-.061	-2.51	-.243 ± .493j	
21	101.5	-16.6	-7.0	-.306 ± 1.02j	-9.86	.559	-3.21	-.166	-.045
22	169.	-9.81	-3.15	-.432 ± 1.48j	-11.12	-2.12	-5.97	-.119	-.056
U/θ_{op} SPEED NUMERATOR									
5	0	0	-8.95	-.23 ± .406j	-10.	-.214	-1.71	-.156	-.245j
6	33.8	0	-13.66	-.105 ± .581j	-9.94	-.446	-1.72	-.17	-.10j
7	67.8	0	-18.2	-.2005 ± .811j	-9.82	-.702	-1.72	-.162	-.062j
8	101.5	0	-25.7	-.281 ± 1.06j	-10.52	-.124	-.043	-1.35 ± .285j	
9	169.	0	-34.1	-.4005 ± 1.51j	-10.63	-.095	-.026	-1.52 ± .732j	
2	28.8	-90.	.254	-.115 ± .327j	-9.76	.616	-1.92	.0224 ± .281j	
20	33.8	-58.3	-6.38	-.141 ± .472j	-9.78	.264	-1.54	-.09	-.594
1	67.8	-25.1	-18.14	-.235 ± .744j	-9.92	-.058	-.174	-1.057 ± .312j	
21	101.5	-16.6	-24.43	-.508 ± 1.05j	-9.72	-1.78	-.513	-.265 ± .297j	
22	169.	-9.81	-34.	-.453 ± 1.53j	-9.57	-.018	-.138	-1.402 ± .856j	

The change in the sign of the root-locus gain is not significant, because of the change in the number of right-half plane zeros. The zero at $s = + 0.349$ is likely to induce a poor step response in level flight, but this should be less troublesome in descent. However, the presence of these zeros will cause difficulty in closing the $\hat{h} \rightarrow \theta_{op}$ loop, so at 100 knots the pusher propeller is not a desirable alternative to the usual $\hat{h} \rightarrow B_{1s}$ and $\hat{h} \rightarrow \theta_c$ loop closures.

At low speeds the pusher propeller shows better promise for control of height error. For example, at 40 knots and $\gamma = - 25.1$ degrees, the $\hat{h}/\theta_{op}$ transfer function is, approximately,

$$\frac{\hat{h}}{\theta_{op}} \doteq \frac{-8.6}{s(s + 0.526)}$$

This avoids the awkward nonminimum phase characteristics of the $\hat{h}$/collective transfer functions listed on Table XXVIII. Hence the pusher propeller may provide a useful method of flight path control at low speeds.

Summary

The control characteristics of compound helicopters have been studied by examining the AH-56A with the all-mechanical stability augmenter system (the "gyro") removed. From calculations of derivatives, transfer functions, and residues, the AH-56A open-loop behavior is seen to be generally that of a typical single-rotor helicopter. Strong coupling occurs between longitudinal and lateral motions, and there is not much effect of descent angle on the eigenvalues except at very low speed. In slow, steep descents, control of flight path with collective is difficult because of the appearance of nonminimum phase zeros in the appropriate transfer functions. This effect is similar to that described for the single-rotor helicopter. However the compound has a possible alternative method of flight path control, through variations of collective pitch of the pusher propeller. This circumvents the non-minimum phase effects and appears to provide a satisfactory method of controlling the flight path.

CHAPTER IX. CONCLUSIONS AND RECOMMENDATIONS

The principal results of this report are contained in the tables of derivatives and transfer functions given in the Appendixes. A large part of the value of the report lies in these detailed numerical results and in the presentation of the analytic and computational methods used to obtain them, e.g., the MOSTAB program. However, certain general conclusions have been reached, and these are presented below, together with recommendations for further work.

1. A new method for predicting the boundaries of the vortex-ring state is presented, using only simple concepts but giving good agreement with experiment.

2. The tip losses on a rotor in vertical descent can be predicted by momentum and blade-element theory, using a flow model which incorporates a sheath of vorticity surrounding the slipstream. The method gives good agreement with experiment in vertical descent; no suitable experimental data are available for inc inclined descent to check the theory for that condition, for which it predicts a cyclically varying tip loss factor.

3. In calculating helicopter derivatives, the perturbations in interference velocities induced by each element on each other element must be included. All lateral-longitudinal cross-coupling derivatives should be included on single-rotor and compound configurations.

4. Derivatives calculated for steep descents are generally appreciably different from derivatives calculated for the same airspeed and level flight. The use of level-flight derivatives for simulations of moderate and steep descents can give seriously misleading results.

4. For tandem-rotor configurations, the principal effects of descent are to cause the dutch roll to degenerate into an aperiodic pair of roots and to worsen the nonminimum phase characteristics of the roll-to-lateral-cyclic numerator. The net effect is to worsen the open-loop dynamics, increasing the need for multiloop feedbacks. Longitudinally the effects of descent angle are generally minor, except for changes in the speed/longitudinal cyclic numerator referred to cockpit axes. This could be important for stability augmenter systems using air data sensors.

169

6. For single-rotor helicopters, lateral-longitudinal cross-coupling effects are important in the transfer function numerators but have little effect on the denominators. The most significant effect of descent angle occurs at low speeds, where control of the flight path by collective pitch becomes seriously degraded due to nonminimum phase effects, causing "wrong-way" responses. This is believed to be the principal cause of the difficulties encountered by helicopters attempting to follow steep approach paths at low speeds. Remedies involving multiloop feedback or elaborate compensation of single-loop feedbacks do not appear feasible.

7. The behavior of compound helicopters is similar to single-rotor helicopters at low speeds, where the wing has little influence. The propeller provides an alternative method of flight path control which shows promise of alleviating the above-mentioned difficulties.

RECOMMENDATIONS FOR FURTHER WORK

Despite the widespread use of helicopters, and the vast production runs of certain types, research on helicopter dynamics consumes only a tiny percentage of the total aerospace budget. It is wise to recognize this situation in presenting a list of topics deserving further research. For example, from a purely technical viewpoint, a good case could be made for a method of calculating derivatives based on a "free-wake" analysis, making the minimum number of assumptions regarding slipstream geometry and interference effects. However, the computer time required to use such a program renders it less desirable than a simpler alternative using "assumed wake" representations. The technical areas listed below have been selected because of their practical importance, and the recommended approaches to solving the problems have been chosen with a realization of the probable financial constraints.

The scope of the items listed below is confined to the area of helicopter steep approaches, but some of the recommendations are sufficiently general to apply to other phases of helicopter operation or even other types of aircraft, such as tilt-rotor configurations.

170

The Vortex-Ring State

The vortex-ring state is important as a limiting condition
on low-speed descent/deceleration capabilities and as the possible
cause of accidents. A better understanding of this state is
required to define it more precisely and to indicate methods of
alleviating the unsteady flow. In addition, some unsteadiness is
known to occur even at shallow angles of descent, and a knowledge
of this self-induced turbulence is required to fully define the
helicopter turbulence environment.

Full-scale flight tests are recommended, plus more refined
theoretical investigations using more sophisticated analytic
techniques than those employed in Chapter II. The result would
be a reliable data base (available data is very incomplete), plus
a nonempirical explanation of the causes of unsteady flow in
steep descents.

Aerodynamics of Rotor in Steep Descents Outside the Vortex-Ring State

Virtually no published experimental data exist on the forces
and moments experienced by helicopter rotors in vertical and in-
clined descent. Model-scale experiments are needed on isolated
rotors, measuring steady and unsteady loads and the induced
velocities at moderate rates of descent. The flow model presented
in Chapter III contains empirical assumptions, but there
seems little point in producing a more complicated theory
without experimental data which are suitable for correlation.
Such experiments should be instrumented to measure the tip losses,
including possible cyclic variations. The number of independent
variables and the desirability of minimizing interference
effects virtually dictate that the tests be conducted at model
scale in a large wind tunnel on an isolated rotor. Tests on a
complete configuration would be disadvantageous because inter-
ference effects from other components would complicate the results.

171

Stability Derivatives

As shown in this report, marked differences exist between
stability derivatives in level flight and descent, causing
important changes in the dynamics of the helicopter. It is there-
fore misleading to use stability derivatives calculated for level
flight to analyze descent problems. Given adequate flow models
for descending rotors, derivatives can be calculated with ease by
MOSTAB or similar programs. The prime question is: how accurate
are these calculations? Since derivatives describe only the
low-frequency behavior of helicopters in small perturbations
from a fixed trim condition, accuracy of $\pm$ 20% should suffice.
However, it is not known whether even this accuracy is being
obtained. Published flight test measurements are few, and
systematic correlations of estimated and measured derivatives
in descending flight are conspicuous by their absence.

To remedy this situation, a research program involving
correlation of estimated derivatives with existing flight test
data should be undertaken. The scope should be broad, including
single-rotor, compound, and tandem configurations in level flight
and descent. The results should be used to refine the derivative
calculation process, particularly the estimation of interference
velocities, which at present is more of an art than a science.
Particular attention should be paid to low-speed descending flight
because the requirements for flight path control on the approach
are particularly stringent, requiring the most accurate derivatives
for analysis.

Transfer Functions

Transfer functions provide an accurate description of
helicopter dynamics over a limited frequency and amplitude range.
The upper frequency limit is set by considerations of blade
modes other than first flapping. Such modes are essentially
"nuisance" modes, i.e., they have no value for flight control.
Thus they can be ignored in flight control system preliminary
design, but must be included in detail design of system hardware
to avoid unwanted coupling effects. The lower frequency limit
is set by time-variations of the nominal operating condition
around which the perturbations are performed. This limit is less
restrictive for descent than for level flight, since the available
deceleration is less, because the helicopter is closer to $(D/L)_{max}$.
Thus there is a broad range of frequencies for which transfer
functions are useful. The following recommendations apply
for this frequency range.

172

Transfer functions including lateral-longitudinal cross-coupling should be used as the basis for future studies of manual and automatic control. Because of computational difficulties, cross-coupling has been ignored in many previous studies; however as shown here cross-coupling effects are quite large and significantly influence closed-loop behavior. Currently the effects of cross-coupling are countered on an ad hoc basis by offsetting the A_{1s}, B_{1s} servos. The cross-coupling phenomenon must be more clearly defined to permit a systematic study of its importance to handling qualities and to determine the best method of counteracting it. The present report used manufacturer's derivatives for the tandem-rotor helicopter, which neglect cross-coupling. Although this appears to be more justifiable for the tandem configuration than for single-rotor helicopters, cross-coupling may still be significant. Flight test data should be examined to verify this.

The significant features of certain transfer functions (i.e., the height error to collective numerator discussed in Chapter VII) should be related to the helicopter geometry. The usual way of doing this is through the use of literal approximate transfer functions (e.g., approximating dutch roll natural frequency as $\omega_d = \sqrt{N_\beta}$). Similar expressions should be developed for the critical right-half plane zero of the height error to collective transfer function and other important parameters. The task is complicated because it is necessary to include lateral-longitudinal cross-coupling; however, it is essential to be able to trace the cause of significant dynamic characteristics to design the helicopter and its stability augmenter together for good flying qualities.

Time-Varying Dynamics Representations

The need for a good method of representing the dynamic interaction of the control system with modes other than first flapping is generally recognized. No special emphasis on steep descents seems necessary here, since development of a method suitable for level flight should meet the requirements for descent. Of more special relevance to approach is the question of the validity of small-perturbation equations about a time-invariant trim condition.

For steep descents the deceleration capability is smaller than in level flight since the helicopter is operating closer to $(D/L)_{max}$. Accordingly, the effect of time variations in the trim conditions should be less important. The net recommendation is that this area is less pressing for steep descents than for level flight.

173

Flying Qualities

Most published research on helicopter flying qualities has concentrated either on hover or on level flight. Significant differences have been shown to exist between open-loop dynamics in level flight and descent, and correspondingly large differences will occur in flying qualities. This area requires investigation by simulation in conjunction with analytic studies of the man-in-the-loop. For example, flight tests indicate that handling qualities are significantly degraded in slow, steep descents (see Chapter II); the cause has been identified in Chapters VII and VIII as the "wrong way" height control characteristics. More work involving detailed loop closures, backed up by simulation, is required to verify this hypothesis.

To obtain specific results, it was necessary to consider only three helicopters, in this report. These are believed to be representative to their general types, but no information has been generated on the effects of helicopter size per se. One would like to know how descent angle affects the flying qualities of the Heavy Lift Helicopter. It is possible that for very large helicopters, body-bending modes may be of sufficiently low frequency to interact with handling qualities. Derivatives should be calculated and assessments made of handling qualities problems in steep descents for such vehicles.

LITERATURE CITED

1. Winick, A. B., V/STOL All-Weather Guidance, J. Aircraft, Vol. 5 No. 5, September-October 1968, pp. 510-511.

2. Deckert, W. H., and D. H. Hickey, Summary and Analysis of Feasibility-Study Designs of V/STOL Transport Aircraft, J. Aircraft, Vol. 7, No. 1, January-February 1970, pp. 66-71.

3. Seckel, E., J. J. Traybar, and G. E. Miller, A Note on the Effect of Helicopter Dynamics on Steep Instrument Approaches, Princeton University Aero. Eng. Rept. 600, 1962.

4. Seckel, E., J. J. Traybar, and G. E. Miller, An Exploratory Study of Instrument Approaches with Steep Gradient Aircraft, Princeton University Aero. Eng. Rept. 630, 1962.

5. Heyson, Harry H., Nomographic Solution of the Momentum Equation for VTOL/STOL Aircraft, NASA TN D-814, April 1961.

6. Mil, M. L., et al., Helicopters; Calculation and Design, Vol. I, Aerodynamics, NASA TTF-494, September 1967.

7. Washizu, Kyuichiro, Akira Azuma, Jiro Koo, and Toichi Oka, Experiments on a Model Helicopter Rotor Operating in the Vortex Ring State, Journal of Aircraft, Vol. 3, No. 3, May-June 1966, pp. 225-230.

8. Payne, P. R., Helicopter Dynamics and Aerodynamics, Sir Isacc Pitman & Sons, London, 1959.

9. Castles, Walter, and Robin B. Gray, Empirical Relation Between Induced Velocity, Thrust, and Rate of Descent of a Helicopter Rotor as Determined by Wind-Tunnel Tests on Four Model Rotors, NASA TN 2474, October 1951.

10. Shapiro, Jacob, Principles of Helicopter Engineering, McGraw-Hill, 1955.

11. Drees, J. Meijer, and W. P. Hendal, The Field of Flow Through A Helicopter Rotor Obtained From Wind Tunnel Smoke Tests, Report A.1205, Versl. Nat. Luchtvlat., Amsterdam, February 1950.

12. Drees, J. Meijer, A Theory of Airflow Through Rotors and Its Application to Some Helicopter Problems, Journal of the Helicopter Association of Great Britain, Vol. 3, No. 2, July-September 1949, pp. 79-104.

13. Drees, J. Meijer, and W. P. Hendal, <u>Airflow Patterns in the Neighborhood of Helicopter Rotors</u>, Aircraft Engineering, April 1951, pp. 107-111.

14. Drees, J. Meijer, L. R. Lucassen, and W. P. Hendal, <u>Airflow Through Helicopter Rotors in Vertical Flight</u>, N.L.L. Report V.1535/Amsterdam, December 1949.

15. Lock, C. N. H., H. Bateman, and H. C. H. Townsend, <u>An Extension of the Vortex Theory of Airscrews with Applications to Airscrews of Small Pitch</u>, Including Experimental Results, British A.R.C. R & M 1014, September 1925.

16. Azuma, Akira, and Akira Obata, <u>Induced Flow Variation of the Helicopter Rotor Operating in the Vortex Ring State</u>, Journal of Aircraft, Vol. 5, No. 4, July-August 1968, pp. 381-386.

17. Washizu, Kyuichiro, Akira Azuma, Jiro Koo, and Toichi Oka, <u>Experimental Study of the Unsteady Aerodynamics of a Tandem Rotor Operating in the Vortex Ring State</u>, Proc. 22nd Annual National Forum, American Helicopter Society, Washington, D.C., May 1966, pp. 215-220.

18. Yaggy, Paul F., and Kenneth W. Mort, <u>Wind-Tunnel Tests of Two VTOL Propellers in Descent</u>, NASA TN D-1766, March 1963.

19. Brotherhood, P., <u>Flight Measurements of the Stability and Control of a Westland Whirlwind Helicopter in Vertical Descent</u>, R.A.E. Technical Report 68021, January 1968.

20. Brotherhood, P., <u>Flow Through a Helicopter Rotor in Vertical Descent</u>, British A.R.C. R & M No. 2735, July 1949.

21. Stewart, W., <u>Flight Testing of Helicopters</u>, J.R.Ae.S., Vol. 52, May 1948, pp. 261-304.

22. Stewart, W., <u>Helicopter Behavior in the Vortex-Ring Conditions</u>, British A.R.C., C.P. No. 99, 1952.

23. Fanucci, J. B., et al., <u>Rotor Downwash in Ground Effect in the Presence of a Step</u>, AIAA Paper 69-225, February 1969.

24. Seckel, Edward, <u>Stability and Control of Airplanes and Helicopters</u>, Academic Press, 1964.

25. Seckel, Edward, and Curtiss, H. C., <u>Aerodynamic Characteristics of Helicopter Rotors</u>, Princeton University, Department of Aerospace and Mechanical Sciences Report No. 659, 1963.

26. Leverton, John W., _Helicopter Noise - Blade Slap_, NASA CR-1221, October 1968.

27. Gessow, Alfred, and Myers, Garry C., _Aerodynamics of the Helicopter_, Macmillan, 1952.

28. Yaggy, Paul F., and Rogallo, Vernon L., _A Wind-Tunnel Investigation of Three Propellers Through an Angle-of-Attack Range From 0° to 85°_, NASA TND-318, May 1960.

29. Anon, _Aircraft Stability Derivatives_, NASA Electronics Research Center RFP Number ERC/R&D GCC-0015, October 31, 1968, pp. II-19 to II-38.

30. Kelly, James K., and Matthew M. Winston, _Stability Characteristics of a Tandem-Rotor Transport Helicopter as Determined by Flight Test_, NASA Technical Note TN D-2847, June 1965.

31. Abzug, M. J., _Steady Sideslip Solutions of the Equations of Aircraft Motion_, TRW Systems Group, Redondo Beach, California, Memo No. 99900-6886-R0-00, 1969.

32. Hayden, J. S., and R. G. Ferry, _H-34A Phase IV Stability Test_, AFFTC TR 56-15, ASTIA AD 96919, 1956.

33. Griffin, J. M., _Digital Computer Solution of Aircraft Longitudinal and Lateral-Directional Dynamic Characteristics_, Air Force Systems Command, Systems Engineering Group, SEG-TR-66-52, 1966.

34. Wolkovitch, J., and R. P. Walton, _VTOL and Helicopter Approximate Transfer Functions and Closed-Loop Handling Qualities_, STI TR 128-1, ASTIA 470137, 1965.

35. Wolkovitch, J., _An Introduction to Hover Dynamics_, Society of Automotive Engineers, Paper 660476, Trans. S.A.E., 1967.

36. Craig, S. J., and A. Campbell, _Analysis of VTOL Handling Qualities Requirements - Part I. Longitudinal Hover and Transition_, AFFDL-TR-67-179.

37. Dillow, J. D., _The "Paper Pilot" - A Digital Computer Program to Predict Ratings for the Hover Task_, AFFDL-FDCC-TM-69-3, 1969.

38. Wolkovitch, J., R. A. Peters, and D. E. Johnston, _Lateral Control of Hovering Vehicles With and Without Sling Loads_, STI TR 145-1, AD 483743, 1966.

39. Wolkovitch, J., _Analytic Study of Limitations on V/STOL Terminal Guidance Caused by Aircraft Response Characteristics_, Mechanics Research, Inc. Report 385-1, forthcoming NASA Contractor Report.